Micromechanical modelling of the thermo-mechanical behaviour of semicrystalline polymers

Document Version:

Publisher's PDF, also known as Version of Record (includes final page, issue and volume numbers)

Please check the document version of this publication:

• A submitted manuscript is the version of the article upon submission and before peer-review. There can be important differences between the submitted version and the official published version of record. People interested in the research are advised to contact the author for the final version of the publication, or visit the DOI to the publisher's website.
• The final author version and the galley proof are versions of the publication after peer review.
• The final published version features the final layout of the paper including the volume, issue and page numbers.

[Link to publication](#)

Micromechanical Modelling
of the Thermo-Mechanical Behaviour
# of Semicrystalline Polymers

Micromechanical Modelling
of the Thermo-Mechanical Behaviour
# of Semicrystalline Polymers

Mikhail Poluektov

geboren te Leningrad, USSR

Dit proefschrift is goedgekeurd door de promotoren en de samenstelling van de promotiecommissie is als volgt:

voorzitter:	prof.dr. L.P.H. de Goey
promotor:	prof.dr.ir. M.G.D. Geers
copromotoren:	dr.ir. J.A.W. van Dommelen
	dr.ir. L.E. Govaert
leden:	prof.dr. C.P. Buckley (University of Oxford)
	prof.dr. S. Ahzi (Université de Strasbourg)
	prof.dr.ir. A.H. van den Boogaard (Universiteit Twente)
	prof.dr.ir. J.M.J. den Toonder

"Physics is mathematical not because we know so much about the physical world, but because we know so little: it is only its mathematical properties that we can discover."
— Bertrand Russell
An Outline of Philosophy (1927)

Contents

Summary

In flexible electronics, polymeric materials should replace conventional substrate materials as silicon, providing flexibility, and potentially enabling roll-to-roll manufacturing. Polymeric films that are used as a substrate for flexible electronics usually have a strongly oriented semicrystalline microstructure, which has to satisfy a number of requirements, among which good dimensional stability, also at elevated temperatures. This dimensional stability is highly dependent on the internal macromolecular orientation.

This thesis aims at understanding and predicting the effects of the microstructure, as well as loading conditions (stress, temperature and time-dependence) on the mechanical response of thin semicrystalline polymer films. For this purpose, a micromechanical thermo-elasto-viscoplastic constitutive model is developed to predict the dimensional stability of films when exposed to various loads. The considered material consists of an aggregate of differently oriented two-phase layered domains, where different constitutive laws are used for each of the phases. The crystalline phase is modelled with crystal viscoplasticity and the amorphous phase is described as an elasto-viscoplastic glassy polymer, taking into account material ageing.

In the second chapter, the interactions between the constituent phases of isotropic semicrystalline polyethylene terephthalate (PET) are analysed. The validity of a hybrid interaction law in a mean-field micromechanical model based on the mechanical behaviour of layered two-phase domains is assessed. For this purpose, an additional two-scale finite-element model of the spherulitic microstructure of a semicrystalline polymer is constructed, taking into account various crystal geometries, including the case when the crystalline regions do not form an interconnected network. It is shown that the predictions of the microscopic deformation measures and macroscopic properties obtained with both models are qualitatively and quantitatively matching.

In the third chapter, the micromechanical model is used to describe the mechanical behaviour of isotropic semicrystalline PET under uniaxial compression up to large strains at different temperatures. Model parameters for the selected constitutive laws of the phases are identified from experimental data. The tensile creep behaviour of isotropic PET is simulated and compared to measurements to demonstrate the applicability of the model to describe the long-term response.

In the fourth chapter, the long-term and short-term anisotropic mechanical behaviour of a biaxially stretched PET film is measured and simulated using the micromechanical model. The representative film microstructure is obtained through the experimental characterisation of the orientation of the crystalline domains. The model is extended to include pre-orientation of the non-crystalline phase. Based on results of the simulations, the deformation mechanisms at the microscopic scale are analysed. The ability to simulate the large-strain anisotropic behaviour of oriented film in the

strain rate controlled regime and the long-term creep regime is demonstrated.

In the fifth chapter, mechanisms of anisotropic reversible and irreversible thermal deformation of a polymer film produced by biaxial stretching are investigated experimentally and numerically with the proposed micromechanical model. The investigated thermo-mechanical effects can be classified as shape memory effects, since the material is partially returning to the initial state before biaxial drawing. The internal stress state is described by two deformation processes with their respective internal stress states and thermal activation energies.

In chapter six, the developed micromechanical model is used to predict the behaviour of the film subjected to conditions representative of the flexible OLED manufacturing conditions. Effects of creep and thermal shrinkage, which are simultaneously observed experimentally, are modelled.

1   Introduction

Abstract: A general introduction to the microstructure and the deformation mechanisms of polymers that are used in the manufacturing of flexible electronics is presented, as well as a brief summary of modelling techniques for the mechanical behaviour of polymers.

1.1   Polymer films in flexible electronics

Nowadays, devices containing electronic circuits manufactured on flexible substrates become increasingly popular [1]. Probably the most well-known of such gadgets are e-readers, which usually include so-called "electronic paper"—displays that reflect light like ordinary paper rather than emit it. Apart from standard e-readers, such as Amazon's Kindle, there are also fully flexible and thus more portable examples like the Readius ebook from Polymer Vision, which further exploit the advantages of this technology. It should be mentioned that at the moment flexible displays are aimed at a slightly different market than their rigid counterparts because of being monochromatic and having slow refresh rates (in fractions of a second rather than milliseconds). Such screens are unable to give the fast, colourful video capabilities that are being expected in, for example, laptops, however there are number of advantages of flexible displays when they are used in portable devices. The application of flexible electronics is not only limited to portables gadgets, but extends to other applications, such as bus-stop signs (Fujitsu), signaling OLEDs on racing cars (Holst Centre), flexible solar panels (PowerFilm), etc. [2].

The increasing sophistication of flexible electronic devices, as seen in figure 1.1, and the growing e-readers' market create a high demand for polymer substrate materials, such as polyimide, polyether ether ketone (PEEK), polyethylene terephthalate (PET) or polyethylene naphthalate (PEN), with properties that can withstand the treatment during the manufacturing process. However, the lithographic patterning of high-quality transistors on polymer substrates, as found on the backplane of a flexible display device, is a major challenge in the manufacturing of flexible electronics [3–5]. In particular, the required overlay and registration accuracy, for which sufficient dimensional stability of the substrate is required, is challenged by the flexible and time-dependent nature of the polymer substrates.

A plastic film, to be used as a substrate for flexible electronics, needs to satisfy the following requirements: high clarity, dimensional stability, thermal stability, impenetrability, solvent resistance, and low coefficient of thermal expansion, coupled with a smooth surface [4]. Because of
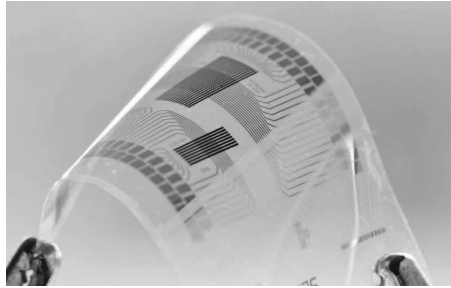
Figure 1.1: Semiconductor memory manufactured on a polymer substrate (Holst Centre).

the continuous miniaturisation of electronic devices, there is a need to understand and to predict the micro-scale deformation of these materials due to mechanical loading as well as due to thermal and hygroscopic (in particular interactions with water and acetone) stresses in order to control the patterning process at micron scale accuracy. So far, two types of polymer film, which have a similar microstructure and deformation mechanisms, are widely used for this type of applications: PET and PEN, with the latter having superior properties. These films are semicrystalline, biaxially oriented and thermally stabilised, with a typical thickness of 25–125 μm. The following will focus mostly on PET since this is used as a model material in this thesis.

Electronic circuits can be manufactured on flexible substrates either by using lithography or by printing, with latter requiring less accurate prediction of mechanical behaviour ($\sim 1\ \mu$m compared to 20–40 nm respectively). At Holst Centre, the roll-to-roll process is used to print electronics on polymer substrates, in which the film is led through several rolls with controlled tension. Following this, the film is heated to a certain temperature (usually above glass transition temperature of the polymer) that is maintained for a relatively long time (~ 1 h) and one layer of electronics is printed with subsequent cooling down. The same procedure is repeated for several layers. During the first temperature treatment, shrinkage effects are observed. Such film deformation after the printing of the first layer must be taken into account during the subsequent process, in order to precisely link the conducting elements. The same holds for another part of the manufacturing process, which is the lamination, when two layers with printed electronics are attached together. Although the printing process is constantly enhanced, for example by the introduction of a tool that uses a photonic process, which heats only the target material rather than the whole substrate, and therefore decreases characteristic times from hours to minutes, it is still important to understand and predict the deformation mechanisms of the substrate material.

At Holst Centre, flexible polymer substrates are also used for lithography, where higher accuracy of prediction of thermo-mechanical behaviour of the substrate material is required. During lithography, to print one layer of electronic circuits, layers of conducting material and resist are deposited on the substrate, with subsequent annealing in an oven where light falls on the assembly through the pattern. After that, parts of the resist are washed away with the solvent, regions where conducting material is open are etched and the rest of the resist is removed. The width of lines of the conducting material in the layer is about 1 μm. Therefore, irreversible deformation of the polymer substrate should be accurately taken into account during further processing stages.
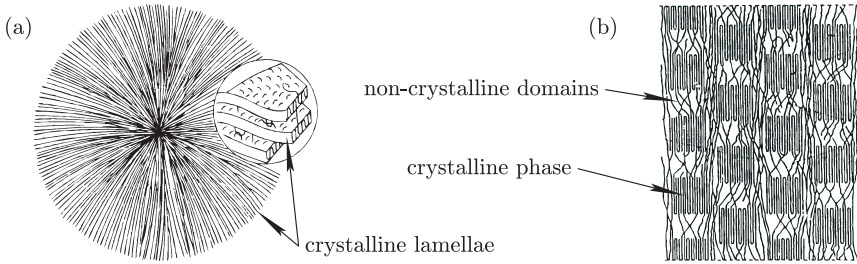
Figure 1.2: The spherulitic structure of melt-crystallised polymer, reproduced from [19] with permission from Springer (a) and the fibrillar structure of oriented polymer fibre reproduced from [17] with permission from John Wiley and Sons (b).

1.2   Semicrystalline microstructure

Thermoplastics, like PET, consist of long molecules, branched or linear, and are able to form different morphologies. Upon heating, the structure transforms into a tangled mass of molecules. During cooling the polymer may crystallise and this process is carried out partially so that some parts remain non-crystalline or amorphous [6]. In case the temperature drops below the value called glass transition temperature, T_g, a glass state (a sort of "frozen liquid") may be formed for the amorphous phase. The crystalline phase forms lamellae, which consist of a parallel stacking of long molecules. These molecular chains can traverse the interface between the crystalline and the amorphous phase and in most cases stay tangled in the non-crystalline phase [7]. However, they can re-enter the crystal if its lateral dimensions are sufficiently large. It should be noted that the size and orientation of the crystalline domains highly depend on the production process: factors like crystallisation temperature or stretching [8]. For most polymers, including high-density polyethylene (HDPE) and PET, molecular chains are oriented at a certain angle to the lamellar surface [9, 10].

As observed in different studies, the morphology of melt-crystallised bulk semicrystalline polymers is often spherulitic [11]. These spherulites are a set of radial crystalline lamellae separated by amorphous layers. Lamellae themselves are often twisted along the radial direction of a spherulite [12–14]. In partially crystallised samples, spherulites are located distantly and have a round shape, but when boundaries come in contact, separate spherulites acquire a polyhedral shape. In the case of partial crystallisation the inter-spherulitic space is filled with amorphous material.

Some semicrystalline polymers, including PET and PEN, can be obtained in various states [15]. For example, fully amorphous material can be obtained by instantly quenching the polymer from the melt state to below T_g. If an amorphous polymer is heated above T_g, the crystallisation process starts and a spherulitic morphology may be formed. For drawn polymer films, the lamellar orientation changes and single crystals incorporated in a matrix of non-crystalline material are observed [16], i.e. a spherulitic microstructure does not exist anymore [17, 18], for comparison see figure 1.2. In the case of drawn polymer fibres, even more pronounced molecular orientation can be found with a fibrillar microstructure [15]. In general, in drawn polymers, molecular chains are usually oriented along the stretch direction. In the case of amorphous polymers, by annealing above T_g, the oriented microstructure is transformed into the isotropic form.

Sometimes another phase, the "rigid amorphous phase" or "intermediate phase", is mentioned

for semicrystalline polymers [20–22]. The orientations of the molecular chains in the non-crystalline domains of a semicrystalline material were found to be oriented preferentially. This shows that the non-crystalline material in semicrystalline polymers may be composed of an unoriented amorphous phase and an intermediate phase where preferable chain orientation exists without a proper crystalline symmetry [20]. Therefore, it appears that the intermediate phase has anisotropic properties in contrast to the amorphous phase. It is difficult to determine quantitative characteristics of the intermediate phase precisely. Some studies report that this third phase should be considered to interpret the behaviour of PET subjected to deformation [23]. Since molecular chains are constrained in the intermediate phase, the glass transition temperature is higher for the intermediate phase than for fully amorphous material [21]. The amount of this phase correlates with the drawing process.

The crystal structure of PET has been studied from the 1950s and it has been determined to be triclinic [24–26]. Many semicrystalline polymers possess different types of crystals and, for example, for PEN the existence of two diverse triclinic unit cell forms was confirmed [27]. For these materials, crystalline lamella thickness is reported to be around 10 nm [10, 26]. In oriented PET, the crystal size depends on the process conditions: samples drawn at equilibrium possess larger crystals than quenched films [28] and at higher annealing temperature, larger crystals are formed [29]. Also, the volume fraction of the crystalline phase depends on the processing conditions and molecular weight. For cold crystallised PET (heated up from the glassy state to above T_g), calorimetric measurements showed 25% crystallinity to be the maximum, with 37% of the intermediate phase. By melt-crystallisation, a crystallinity of 35% with 14% of the intermediate phase can be obtained [21]. For oriented PET films and fibres, crystallinity may reach 50%, depending on processing conditions.

Two rotational isomers of the structural unit of the PET molecule exist: *trans* and *gauche*. Crystalline phase of PET consists solely of *trans* isomers and non-crystalline predominantly of *gauche* [22, 30]. Without direct evidence, the intermediate phase has been considered to consist of the *trans* isomer [30]. During stretching of the molecules not only the alignment of the *trans* isomer takes place, but a transition from *gauche* into *trans* as well.

1.3 Deformation mechanisms and molecular orientation

Deformation in PET, like deformation in other semicrystalline polymers, can be divided into three types: elastic deformation, which results from stretching bonds and is recoverable; unrecoverable viscous flow, which originates from slippage of molecules; and uncoiling of polymer chains, originating from molecular alignment and being slowly recoverable [15, 18]. In the case of PET films, upon drawing, the molecular chains are rotated and arranged in the direction of drawing, and phenyl rings tend to arrange with their plane close to the plane of the film [8, 30, 31]. The orientation of the non-crystalline phase is directly proportional to the draw ratio [32]. During deformation strain-induced crystallisation, resulting in strain hardening, can be observed in most semicrystalline polymers [33]. The deformation kinetics of polymers also highly depend on temperature and thermomechanical history.

The mechanism of plastic deformation of the crystalline phase is crystallographic slip taking place on certain slip systems [34]. Because of the complex crystallographic structure of the polymer crystals, various slip systems may be physically distinct and hence have different properties.

Sequential drawing in two orthogonal directions (the machine and the transverse directions)

can strengthen the film by orienting the molecules in different directions and creating taut regions, which are hard to deform further, resulting in increase in dimensional stability and elastic properties of the film [8]. Films that are stretched simultaneously have similar properties in both directions, the sequentially stretched ones have a noticeable anisotropy. The orientation of the molecules, in its turn, depends on the strain rate, extension ratio, molecular weight, and orientation temperature [15, 18].

For pre-stretched PET and PEN films, irreversible thermal shrinkage has been observed, which is believed to be related to thermal chain relaxation of oriented amorphous regions above T_g [35]. This phenomenon is reduced by the crystallinity due to cross-linking effects of the crystallites. For biaxially oriented films, the magnitude of expansion or shrinkage depends on annealing temperature and the molecular orientation [36].

1.4 Existing micromechanical modelling methods

Various constitutive models might be used to simulate the macroscopic behaviour of polymer materials, such as the model by Buckley et al. [37,38], by Boyce et al. [39,40] and by Govaert et al. [41,42]. These models provide an accurate representation of the mechanical behaviour of amorphous glassy polymers. By performing material characterisation once, they can describe complicated deformation cases, for example, flat-tip micro-indentation and notched impact tests [43], the large-strain behaviour of particle-reinforced composites with a polymer matrix [44] or strain localisation and necking of tensile bars [45]. In the latter work, anisotropic flow was taken into account for modelling. In general, in such models it is possible to take into account thermorheologically complex behaviour and thus they can also capture the response of semicrystalline polymers [46]. Even though it is even possible to use orientation distribution functions as internal state variables to simulate the behaviour of oriented semicrystalline polymers while tracking the evolution of morphology [47], detailed conclusions about microstructural changes and local deformation mechanisms can only be obtained by using micromechanical or multi-scale simulations that have separate constitutive descriptions of the underlying phases.

The main task of micromechanics is known as homogenisation and consists of predicting the material properties on the basis of the geometries and properties of the individual phases. The second task is the estimation of the stress and strain distributions in the individual phases for prescribed loading conditions, enabling to describe morphological changes and predict material damage. Micromechanical approaches can be separated into continuum methods and discrete methods, such as molecular dynamics, which is a very powerful method, however requiring lots of computational resources.

One of the approaches to simulate the mechanical behaviour of a polymer with known microstructure, i.e. isotropic (spherulitic) or oriented, is finite-element modelling. For example, in [48], the elastic response of semicrystalline polyethylene was modelled as the response of a multilayered spherical structure with alternating amorphous and crystalline layers using a finite-element approach, and in [49], the elastic properties of semicrystalline nylon, with a wavy-shaped monoclinic lamellar morphology, were obtained using finite-element simulation. By using appropriate constitutive laws for the underlying phases, simulation of the large-strain material behaviour can be performed. An example of such an approach, applied to the viscoplastic deformation of spherulitic polyethylene, can be found in [50]. The time-consuming requirement to create different geometries for various crystallinities and orientation distributions of the phases as well as high computational

costs are certainly drawbacks of such finite-element approach.

To construct computationally efficient models, other forms of homogenisation can be used. Only a limited number of problems in continuum mechanics where the material consists of several domains, which have different properties (such as a ellipsoidal inclusion in an infinite homogeneous matrix [51]), can be solved exactly. Thus the interaction between domains can be replaced with an average or effective interaction simplifying the problem. After that, mean-field homogenisation principles can be applied to such domains. Among the most commonly used homogenisation approaches are rules of mixtures, the self-consistent scheme and the Mori-Tanaka method.

Rules of mixtures can be applied to separate phases, for example crystalline and amorphous domains of the semicrystalline polymer, as well as individual domains that can in turn be multi-phase objects. The Voigt model in elasticity (or the Taylor model in polycrystal plasticity) assumes the average strain within each phase to be equal to the macroscopic strain, satisfying local compatibility between the phases, but not the local traction equilibrium. Similarly, in the Reuss model in elasticity (or the Sachs model in plasticity) the average stress of each phase is equal to the macroscopic stress. These models can be an equivalent to a parallel or series connection of mechanical elements, respectively.

The validity of these models when applied to semicrystalline polymers is doubtful. In [52] and [53], a fully viscoplastic micromechanical model applied to HDPE and an elastic micromechanical model applied to PET, respectively were used. Numerical and experimental results demonstrated that the Voigt model is not suitable for polymers, highly overestimating their properties because of the relatively weak interaction between domains in polymer materials, in contrast to grains in metals, where the Voigt model might be applied. Experimental data [11] confirms that freely rotating lamellar stacks can be observed during deformation.

Other homogenisation methods use an analytical solution for the elastic field of an ellipsoidal inclusion placed in an infinite homogeneous medium [51]. In case of an ellipsoidal shape of the inclusion, the strain field inside the inclusion is uniform and linked with the strain field of the inclusion without surrounding matrix through the Eshelby tensor. In the self-consistent approach [54], the material is considered as a set of domains. The assumption of the method consists of replacing the interaction between the domain and the surrounding material by the interaction of the domain (or inclusion), which has an ellipsoidal shape, and an effective medium (material that has effective properties). Initially, this method was used for polycrystalline material, for example see [55]. An example of the application of the self-consistent approach to the elastic behaviour of semicrystalline polymers can be found in [52, 56, 57], where this method was applied to domains that contain multiple phases.

In the Mori-Tanaka method [58,59], inclusions of one phase are incorporated into the matrix of the second phase. Again based on Eshelby's solution, concentration tensors and the effective composite properties can be obtained. This mean-field method gives a good estimation of properties of the semicrystalline polymers, especially for the cases of low crystallinity. In [60], semicrystalline materials (polyethylene and syndiotactic polystyrene) were treated as fibre reinforced composites, where the matrix represented the amorphous phase and the crystalline phase was modelled as randomly distributed ellipsoidal inclusions with two independent aspect ratios. Examples of the application of the Mori-Tanaka method to semicrystalline polymers can be also found in [56, 57].

It is also possible to apply these methods in viscoplastic cases, for example, using an incremental approach [61], integral transformations [62] and more recently non-incremental formulations [63]. Alternatives to self-consistent methods are approaches based on variational principles, for example [64]. In addition, there are many varieties of methods of homogenisation of elasto-viscoplastic

materials, comparisons of which can be found in [63, 65, 66].

In [53] the Mori-Tanaka and the self-consistent schemes were applied to PET and several extensions of two-phase inclusions were analysed: an extension of the double-inclusion model of [67], which consist of three nested domains (the inner domain corresponds to the single-crystal, embedded in an intermediate phase, which in turn is surrounded by the amorphous phase), and inclusion model that consisted of three adjacent layers (a crystalline lamella, a rigid amorphous phase and a mobile amorphous phase). The elastic moduli estimated by different homogenisation schemes were found to be close at low crystallinity and started to deviate at higher crystallinity values, making such inclusion models suitable for PET since the crystallinity of PET is relatively low. A similar comparison for PET was made in [68].

There are some other homogenisation techniques, for example, using Halpin-Tsai equations [69]. In [70] the spherulitic microstructure was modelled as amorphous matrix reinforced with crystalline fibres. Later, in [71], the material was modelled as a layered structure, and within each layer, the lamellae were randomly oriented in a 2D plane. Modified Halpin-Tsai equations were used in [72] to estimate the average elastic response of polyethylene.

An alternative modelling approach, which is based on hybrid interaction schemes between Voigt and Reuss, is the composite inclusion model as proposed by pioneering work of Lee et al. [73, 74] and Ahzi et al. [75, 76]. It was developed to predict the elasto-plastic deformation and texture evolution of semicrystalline polymers. The crystalline and the amorphous phase of the material are described by dedicated constitutive relations, using crystal plasticity for the crystalline phase. The two phases are assembled into a layered structure, the composite inclusion, which is the basic structural element of the model. The micromechanical approach is based on a hybrid interaction between these inclusions. The assembly could be either random, for instance, when isotropic material is modelled, or preferentially oriented.

Recently, in [77] an extended inclusion model was suggested introducing a third phase, the rigid-amorphous layer. The influence of incorporating this third phase versus a two-pase model for material properties with the same degree of crystallinity was investigated. It was found that the third phase can be left out for spherulitic material, but may be important for oriented material. More detailed modelling of the spherulitic morphology has validated the applicability of the composite inclusion model [78], where the spherulitic microstructure was approximated using two-dimensional finite-element models. Regular and random spherulite stacking models were considered. The simulations showed that the stacking does not influence micromechanical deformations significantly. In [79], the tensile behaviour of oriented polyethylene was investigated. A tensile bar was modelled using the finite-element method and the behaviour of a material point was obtained from the composite inclusion model. Experimentally observed effects were qualitatively captured by simulations. In [80], the double yield phenomenon was modelled with the composite inclusion model for polyethylene, and in [81] this model was used to simulate the creep behaviour and predict the time-to-failure of polyethylene.

1.5   Scope and the outline of the thesis

The work presented in this thesis aims at understanding and predicting the effects of time, stress and temperature on the mechanical response of thin semicrystalline polymer films under conditions relevant for lithographic processing. A high accuracy of registration during this process is essential to ensure correct circuit fabrication; however this precision can be affected by dimensional instability.

Through a rigorous understanding of the molecular viscoplasticity of the films over the range of process conditions, the findings of this work lead to further understanding of the time-dependent micro-deformation and the interaction of the constituent phases of PEN and PET films during processing by lithography and film handling. These predictions enable a further optimisation of the patterning processes on flexible substrates and the development of compensation algorithms for maskless imaging on flexible substrates.

In the thesis a precise comparison of the selected micromechanical approach with full-field simulations of an isotropic material microstructure for the elastic case is made in order to validate the model prediction of the micromechanical deformation mechanisms. Furthermore short-term large-strain and long-term small-strain deformation of isotropic and oriented semicrystalline material is predicted for a range of temperatures and crystallinities including temperatures below and above T_g using a selected micromechanical approach. The final part of the thesis deals with the simulation of the shape-memory effect, or dimensional instability at high temperatures, arising from the presence of internal stresses in the biaxially oriented film, which is the result of the manufacturing process.

2 Elastic behaviour of isotropic semicrystalline PET[*]

Abstract: The aim of this study is to assess the interactions between the constituent phases of polyethylene terephthalate and thereby analyse the validity of a hybrid interaction model in a mean field micromechanical model based on layered two-phase inclusions. Two different modelling approaches are used to simulate the behaviour of semicrystalline polymers. The first approach is the micromechanical model based on interactions of the crystalline lamellae and the adjacent amorphous layers. The second approach is a two-scale finite-element model of the spherulitic microstructure. Isotropic polyethylene terephthalate is selected as the model material. The deformation mechanisms at the microscopic scale are examined. Various crystal geometries are used in the finite-element model to analyse the case when the crystalline regions do not form an interconnected network. It is shown that the predictions of the microscopic deformation measures obtained with the micromechanical and the finite-element models are similar. Experimental evaluation of the elastic moduli has been performed to further estimate the applicability of the micromechanical model to PET.

2.1 Introduction

Semicrystalline polymers are widely used in various high-tech applications such as electronic paper or flexible electronics, which have numerous advantages over conventional rigid-substrate semiconductor products [1]. In particular *polyethylene terephthalate* and *polyethylene naphthalate* films (or PET and PEN) may serve as a substrate material in lithography or printing [4]. The dimensional stability of these films during the manufacturing process should be precisely controlled to achieve accuracy in the transistor patterning process. However, various challenges arise when the oriented film behaviour is analysed, since effects such as thermal behaviour or moisture absorption, play a role in addition to viscoelastic deformation [18].

The morphology of melt-crystallised semicrystalline polymers, as observed with polarising microscopy, is generally spherulitic [12]. The crystallisation starts from certain points, spherulite centres, and then the lamellae grow along the radial direction. While growing, the crystalline layers are

---

[*] This chapter is partly reproduced from [82].

being twisted along the radial direction of the spherulite. In the beginning, spherulites are located distantly and have a round shape, however, when the boundaries come in contact, spherulites acquire a polyhedron shape. In case of partial crystallisation, the inter-spherulite space is filled with amorphous material. A crystalline phase, a constrained amorphous phase within the spherulites and an unconstrained amorphous phase between the spherulites can then be distinguished. Oriented semicrystalline films reveal a different microstructure: separate crystals with preferred orientations, embedded into amorphous material, are likely to be found in drawn films [16].

In general, PET possesses a three-phase microstructure [23], where besides the crystalline and the amorphous phase, an "intermediate" phase exists. Within this phase, molecular chains have a preferential orientation, but they are not arranged in a perfect crystal. There are two different conformational isomers (rotational isomers) of the PET molecular unit: *trans* and *gauche*. The PET crystals consist of the trans isomer and the amorphous material of gauche [30]. Presumably, the intermediate phase consists of the trans conformer and has a specific orientation which was obtained during drawing. For HDPE it was shown that the intermediate phase does not necessarily need to be taken into account for modelling isotropic semicrystalline material [77]. Therefore, in this study, the intermediate phase is, to a first approximation, neglected.

There are several types of modelling approaches for multi-phase materials, ranging from macroscopic models to micromechanically-based methods, as well as methods using molecular dynamics. In continuum micromechanics, the macroscopic material properties are predicted, based on the geometries and the properties of the individual phases, thereby also estimating the stress and strain distributions over the phases for the prescribed loading conditions. In mean-field micromechanical approaches, the real interaction between the phases is replaced with an average or effective interaction model, and the effective material response is obtained through homogenisation. Among the most commonly used homogenisation techniques are rules of mixtures (such as Voigt and Reuss averages), the self-consistent method [54], the Mori-Tanaka method [58, 59] and semi-empirical Halpin-Tsai equations [69]. Thus, different models of semicrystalline polymers, that use different homogenisation techniques, exist. In [52] and [53] a fully viscoplastic micromechanical model applied to high density polyethylene (HDPE) and an elastic micromechanical model applied to PET were analysed. The numerical and experimental results demonstrate that the Voigt interaction model is not suitable for such polymers, since it highly overestimates their properties. The self-consistent method was initially used for polycrystalline materials (for example [55]) and in general would not necessarily be suitable for composites with a matrix and inclusions of another phase incorporated in it. However, there are cases for which it does give good result, an example of application of the self-consistent approach to semicrystalline polymers can be found in [56, 57], where the grain is a composite inclusion, that consists of two phases: crystalline and amorphous (in the form of two layers), with an ellipsoidal shape, incorporated into the medium that has the effective properties of the semicrystalline material.

The model, considered in this study, is the mean-field model called the composite inclusion model [73, 83]. It was originally developed for the large-strain deformation of HDPE, and uses a layered object, the composite inclusion, which consists of crystalline, amorphous and possibly other phases, as a basic structural element. The material behaviour is obtained from the averaging over all inclusions, assuming a certain interaction law between them. This approach was used to model the spherulitic morphology of semicrystalline polymers [78] and the behaviour of a tensile bar under uniaxial stress [79]. In [80], the composite inclusion model was applied to polyethylene and the double yield phenomenon was observed.

The elastic behaviour of PET was studied in [53], where normalised self-consistent and gener-

alised Mori-Tanaka models were applied to three-phase inclusions with different internal geometries. An application of a composite inclusion-based model in an elastic formulation to PET can be found in [68]. In both cases, the predicted elastic properties at the macroscopic scale matched experimental results well. The aim of this study is to assess whether the interaction laws used in the composite inclusion model, are suitable for modelling micromechanical aspects of deformation for PET, for which the range of crystallinities is different than for HDPE. For this purpose, a new, more detailed, two-scale finite-element model of the spherulitic microstructure is developed and the results of the full-field simulations are compared with the mean-field approach for the elastic material. Thereby, the two-scale finite-element model is used to elucidate the micromechanical deformation mechanisms within the constituent phases of a spherulitic structure. A detailed comparison of the elastic composite inclusion model with full-field finite-element simulations reveals the ability of the composite inclusion model to predict these mechanisms. The finite-element model gives information about the interactions between the phases and the ability of the mean-field model to represent these interactions. In addition to a comparison of the fields at the microscopic scale, taking into account various microstructural geometries, in this study also a macroscopic validation of the composite inclusion model is made. Furthermore, a series of experiments were carried out to validate this model and assess whether a two-phase model is indeed sufficient in case of PET.

2.2   Experimental methods

PET cast film with initial crystallinity less than 1% was supplied by DuPont Teijin Films (experimental grade). The samples were cut from sheets of the film according to ISO 527-2, type 1BA, and were annealed at $100\,^{\circ}\text{C}$ for times ranging from 1 to 14 hours in order to obtain samples with a wide range of crystallinities. To flatten the samples, they were placed between aluminium plates. Also, to prevent surface pitting, polyamide film was placed between samples and outer aluminium plates.

Crystallinity of the samples was measured by differential scanning calorimetry (DSC) and X-ray diffraction. The determination of the degree of crystallisation by calorimetric means was undertaken on a Mettler-Toledo 823DSC, using a mass of $10\,\text{mg}$ and a heating rate of $10\,^{\circ}\text{C/min}$ from $25\,^{\circ}\text{C}$ to $280\,^{\circ}\text{C}$. Each cold crystallisation exotherm curve was subtracted from the "fully" crystallised curve in order to calculate the degree of crystallisation.

Tensile testing of the samples was carried out on a Zwick Z010 tensometer at $25\,^{\circ}\text{C}$. The strain rate used for all tests was $10^{-3}\,\text{s}^{-1}$ and the maximum strain was 8%, encompassing the yield behaviour. In each case, the test was carried out three times to ensure reproducibility.

2.3   Model formulation

Two elastic models for semicrystalline material are compared at the macroscopic and microscopic scale: a mean-field composite inclusion model and a detailed finite-element model of the spherulitic microstructure. For the latter, also the influence of the crystal geometry on the elastic behaviour is investigated. In this section, a short summary of the composite inclusion model is given (more details can be found in [77, 83]) and the two-scale finite-element model is introduced.
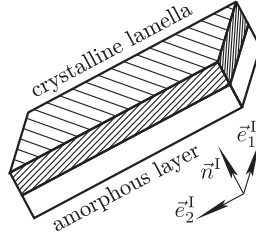
Figure 2.1: The two-layer composite inclusion after [73, 83].

2.3.1 Composite inclusion model

Since only small elastic deformations are considered, the small strain tensor $\boldsymbol{\varepsilon} = (\vec{\nabla}\vec{u} + (\vec{\nabla}\vec{u})^{\mathrm{T}})/2$ and the Cauchy stress tensor $\boldsymbol{\sigma}$ are used as the strain and stress measures. The composite inclusion model is a material point model, in the general case, relating the stress to the deformation. Two scales are considered, and the effective (averaged) characteristics $\bar{\boldsymbol{\sigma}}, \bar{\boldsymbol{\varepsilon}}$ are defined at the macroscopic scale. At the microscopic scale, a multi-phase structure, consisting of crystalline and amorphous domains, is introduced. Assuming the constitutive behaviours of the phases are known ($\boldsymbol{\sigma}^{\mathrm{c}} = \boldsymbol{\sigma}^{\mathrm{c}}(\boldsymbol{\varepsilon}^{\mathrm{c}})$ and $\boldsymbol{\sigma}^{\mathrm{a}} = \boldsymbol{\sigma}^{\mathrm{a}}(\boldsymbol{\varepsilon}^{\mathrm{a}})$) and when specific interaction laws between the phases and structures are assumed, the macroscopic behaviour can be modelled. In this study, only the linear elastic regime is considered, thus, Hooke's law is used as the constitutive law for both phases, where the crystalline phase is modelled as being anisotropic.

The structural element of the micromechanical model is the composite inclusion, which is an assembly of a single crystalline lamella and the neighbouring amorphous layer (see figure 2.1). The stress and strain fields are considered to be piecewise-homogeneous within the inclusion, i.e. constant within the single phase. The shape of the inclusion is not specified, only the volume fractions of the crystalline (f^{c}) and the amorphous ($f^{\mathrm{a}} = 1 - f^{\mathrm{c}}$) phases are defined. Restrictions are applied to the strain and stress fields of the individual phases, because the two phases are connected at the interface (compatibility and traction continuity). Thus, the variables defined by:

$$\vec{\sigma}_n = \boldsymbol{\sigma} \cdot \vec{n}^{\mathrm{I}}, \tag{2.1}$$

$$\varepsilon_{ks} = \vec{e}_k^{\mathrm{I}} \cdot \boldsymbol{\varepsilon} \cdot \vec{e}_s^{\mathrm{I}}, \quad \forall \vec{e}_k^{\mathrm{I}}, \vec{e}_s^{\mathrm{I}} \in \mathscr{X}^{\mathrm{I}} \,|\, \vec{e}_k^{\mathrm{I}} \times \vec{e}_s^{\mathrm{I}} = \vec{n}^{\mathrm{I}} \tag{2.2}$$

are assumed to be continuous across the interface, where $\mathscr{X}^{\mathrm{I}}$ is the interface plane and $\vec{n}^{\mathrm{I}}$ is the interface normal. Components of tensors $\boldsymbol{\varepsilon}$ and $\boldsymbol{\sigma}$ that are not constrained by these relations can be discontinuous. The inclusion-averaged stress and strain tensors are calculated as the volume weighted averages:

$$\boldsymbol{\sigma}^{\mathrm{I}} = f^{\mathrm{c}}\boldsymbol{\sigma}^{\mathrm{c}} + f^{\mathrm{a}}\boldsymbol{\sigma}^{\mathrm{a}}, \tag{2.3}$$

$$\boldsymbol{\varepsilon}^{\mathrm{I}} = f^{\mathrm{c}}\boldsymbol{\varepsilon}^{\mathrm{c}} + f^{\mathrm{a}}\boldsymbol{\varepsilon}^{\mathrm{a}}. \tag{2.4}$$

The material behaviour is modelled as the average behaviour of N differently oriented inclusions (here for quantities of the particular inclusion i superscript I_i is used; in other equations index i is omitted), i.e.:

$$\bar{\boldsymbol{\sigma}} = \frac{1}{N} \sum_{i=1}^{N} \boldsymbol{\sigma}^{\mathrm{I}_i}, \tag{2.5}$$

$$\bar{\varepsilon} = \frac{1}{N} \sum_{i=1}^{N} \varepsilon^{\mathrm{I}_i}. \tag{2.6}$$

Voigt, Reuss or other hybrid interaction models are used to describe the interactions between the individual composite inclusions. In the Voigt model, the average inclusion strain $(\varepsilon^{\mathrm{I}})$ is equal to the macroscopic strain $(\bar{\varepsilon})$, satisfying inter-inclusion compatibility but not inter-inclusion traction equilibrium. In the Reuss model, the average inclusion stress (σ^{I}) is matching the macroscopic stress $(\bar{\sigma})$, fulfilling inter-inclusion traction equilibrium unlike inter-inclusion compatibility. These models can be imagined as a parallel or series connection of inclusions, respectively, providing the stiffest and the most compliant way of coupling the inclusions.

The conditions (2.1) and (2.2) are constraining three of six independent components of the strain and stress tensors within the phases of the composite inclusion. A hybrid averaging scheme can be obtained by either using a Voigt-type interaction model only for the unconstrained components of ε^{I} or a Reuss-type interaction model only for the unconstrained components of σ^{I}. Thus, the first hybrid law requires the unconstrained inclusion stress components $(\sigma_{11}^{\mathrm{I}}, \sigma_{22}^{\mathrm{I}}$ and $\sigma_{12}^{\mathrm{I}})$ in the interface coordinate system with $\vec{e}_3^{\mathrm{I}} = \vec{n}^{\mathrm{I}}$, to be equal to the macroscopic stress components $(\bar{\sigma}_{11}, \bar{\sigma}_{22}$ and $\bar{\sigma}_{12}$, respectively) in the same coordinate system. In this case, an auxiliary tensor $\hat{\varepsilon}$ is introduced with the $\hat{\varepsilon}_{33}, \hat{\varepsilon}_{23}$ and $\hat{\varepsilon}_{31}$ components in the interface coordinate system equal to the $\varepsilon_{33}^{\mathrm{I}}, \varepsilon_{23}^{\mathrm{I}}$ and $\varepsilon_{31}^{\mathrm{I}}$ strains of each inclusion, respectively.

Formally, these interaction laws can be written using two fourth-order projection tensors:

$${}^{4}\boldsymbol{\mathcal{P}}_{n}^{\mathrm{I}} = \vec{e}_{1}^{\mathrm{I}}\vec{n}^{\mathrm{I}}\vec{n}^{\mathrm{I}}\vec{e}_{1}^{\mathrm{I}} + \vec{e}_{2}^{\mathrm{I}}\vec{n}^{\mathrm{I}}\vec{n}^{\mathrm{I}}\vec{e}_{2}^{\mathrm{I}} + \vec{n}^{\mathrm{I}}\vec{e}_{1}^{\mathrm{I}}\vec{e}_{1}^{\mathrm{I}}\vec{n}^{\mathrm{I}} + \vec{n}^{\mathrm{I}}\vec{e}_{2}^{\mathrm{I}}\vec{e}_{2}^{\mathrm{I}}\vec{n}^{\mathrm{I}} + \vec{n}^{\mathrm{I}}\vec{n}^{\mathrm{I}}\vec{n}^{\mathrm{I}}\vec{n}^{\mathrm{I}}, \tag{2.7}$$

$${}^{4}\boldsymbol{\mathcal{P}}_{\mathscr{X}}^{\mathrm{I}} = {}^{4}\boldsymbol{\mathcal{I}} - {}^{4}\boldsymbol{\mathcal{P}}_{n}^{\mathrm{I}}. \tag{2.8}$$

The first projection tensor acting on the stress tensor $({}^{4}\boldsymbol{\mathcal{P}}_{n}^{\mathrm{I}} : \sigma^{\mathrm{I}})$ leaves only the components corresponding to intra-inclusion traction conditions, i.e. the out-of-plane components with respect to the interface. Similarly, the second projection tensor provides the components for intra-inclusion compatibility, i.e. the in-plane components with respect to the interface. Thus, equations (2.1) and (2.2) using equations (2.7) and (2.8) can be rewritten as the following equations which are fulfilled for all inclusions:

$${}^{4}\boldsymbol{\mathcal{P}}_{n}^{\mathrm{I}} : \sigma^{\mathrm{I}} = {}^{4}\boldsymbol{\mathcal{P}}_{n}^{\mathrm{I}} : \sigma^{\mathrm{c}} = {}^{4}\boldsymbol{\mathcal{P}}_{n}^{\mathrm{I}} : \sigma^{\mathrm{a}}, \tag{2.9}$$

$${}^{4}\boldsymbol{\mathcal{P}}_{\mathscr{X}}^{\mathrm{I}} : \varepsilon^{\mathrm{I}} = {}^{4}\boldsymbol{\mathcal{P}}_{\mathscr{X}}^{\mathrm{I}} : \varepsilon^{\mathrm{c}} = {}^{4}\boldsymbol{\mathcal{P}}_{\mathscr{X}}^{\mathrm{I}} : \varepsilon^{\mathrm{a}}. \tag{2.10}$$

For the so called $\hat{\varepsilon}$-inclusion model, where the strain-like auxiliary tensor $\hat{\varepsilon}$ is introduced, the inter-inclusion conditions can then be written as:

$${}^{4}\boldsymbol{\mathcal{P}}_{\mathscr{X}}^{\mathrm{I}} : \sigma^{\mathrm{I}} = {}^{4}\boldsymbol{\mathcal{P}}_{\mathscr{X}}^{\mathrm{I}} : \bar{\sigma}, \tag{2.11}$$

$${}^{4}\boldsymbol{\mathcal{P}}_{n}^{\mathrm{I}} : \varepsilon^{\mathrm{I}} = {}^{4}\boldsymbol{\mathcal{P}}_{n}^{\mathrm{I}} : \hat{\varepsilon}. \tag{2.12}$$

Together with the expressions for the volume-averaged stress and strain $(\bar{\sigma}$ and $\bar{\varepsilon})$, i.e. equations (2.5) and (2.6), the constitutive relations for the phases $(\sigma^{\mathrm{c}} = {}^{4}\boldsymbol{\mathcal{C}}^{\mathrm{c}} : \varepsilon^{\mathrm{c}}$ and $\sigma^{\mathrm{a}} = {}^{4}\boldsymbol{\mathcal{C}}^{\mathrm{a}} : \varepsilon^{\mathrm{a}})$, six boundary conditions and equations (2.3), (2.4), (2.9), (2.10), (2.11), (2.12), a full set of equations, which allows to find all quantities at the material point, is obtained. Since linear elastic behaviour is considered, the macroscopic stiffness tensor ${}^{4}\bar{\boldsymbol{\mathcal{C}}}$, relating $\bar{\sigma}$ and $\bar{\varepsilon}$, can be obtained directly [77].
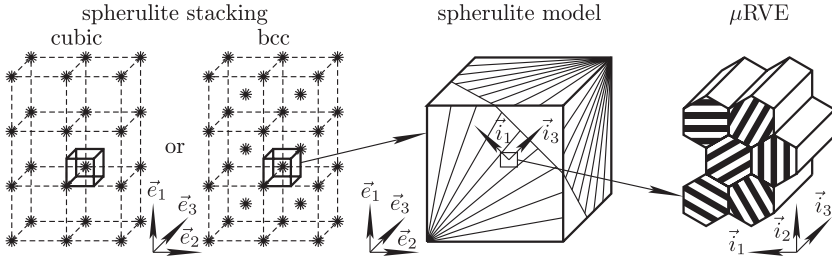
Figure 2.2: The two-level finite-element modelling scheme.

2.3.2 Finite-element model

In this work, isotropic PET is the subject of study. Therefore, a spherulitic microstructure is modelled using a two-scale finite-element scheme. Considering images of crystallised PET [84], the assumption is made that spherulites fill up the whole space and that there is no unconstrained amorphous material, at least at relatively high crystallinity.

Three length scales are considered: macroscopic, mesoscopic and microscopic. At the macroscopic length scale (application scale), PET film is homogeneous. At the mesoscopic length scale, spherulites can be distinguished and at the microscopic scale, individual crystalline and amorphous regions are modelled.

The modelling concept is similar to [78], where the mesoscopic scale (the spherulitic level) was represented by a finite-element model and the behaviour of a material point in the spherulitic model was represented by the composite inclusion model. In this study, the constitutive behaviour of a material point at the spherulitic level is modelled by another finite-element model which is representative for a bundle of parallel but twisted crystalline lamellae and corresponding amorphous regions. Homogenised properties of the mesoscopic scale model can subsequently be used to solve the macroscopic scale problem.

Mesoscopic scale

At the mesoscopic scale, individual spherulites can be distinguished. At this level, a three-dimensional spherulite model with symmetry boundary conditions, derived from the stacking of spherulites, is used (figure 2.2). Various spherulite layouts in space may exist e.g. regular or irregular. However, it has previously been found that the irregularity of spherulite stacking is not important [78]. Therefore, in this study, only ordered arrangements of spherulite centres are used: a cubic stacking (when the spherulite centres are located at the corners of a cubic unit cell) and a body-centred cubic (bcc) arrangement. Using symmetry of the geometry, $\frac{1}{8}$th of the periodic cubic volume is modelled. In figure 2.2, the spherulite model representing the bcc stacking is highlighted, with lines showing the crystalline lamella growth direction.

The spherulite model is defined in a global coordinate system given by the unit vectors $\vec{e}_1$, $\vec{e}_2$, $\vec{e}_3$. The properties of a material point in the spherulite model are defined by the orientation of the crystalline lamellae at this point, which depends on the positions of the spherulite centres. In each point, the growth direction of the lamellae is taken as the direction from the nearest spherulite centre to the point. The spherulite model derived from the cubic stacking has a spherulite centre at
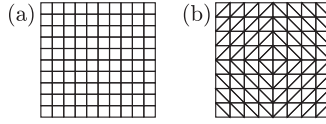
Figure 2.3: Meshes for cubic (a) and bcc (b) spherulitic models.

position $(0; 0; 0)$, and for simplicity is referred to as the cubic model. The model corresponding to the bcc stacking has two spherulite centres at $(0; 0; 0)$ and $(l; l; l)$, with l the dimension of the unit cell. Symmetry boundary conditions are imposed:

$$u_1(0; x_2; x_3) = 0, \ u_2(x_1; 0; x_3) = 0, \ u_3(x_1; x_2; 0) = 0,$$
$$u_1(l; x_2; x_3) = U_1, \ u_2(x_1; l; x_3) = U_2, \ u_3(x_1; x_2; l) = U_3,$$

with u_k, $k = \overline{1,3}$ the nodal displacement.

The volume corresponding to the cubic model is meshed using 10×10×10 linear brick elements. The volume corresponding to the bcc model is meshed using linear tetrahedron elements (see figure 2.3).

Microscopic scale

The microscopic scale model (which will be referred to as the *microscale representative volume element*, or the μRVE) represents a bundle of crystalline lamellae with amorphous layers in between them and having various angles of rotation around the radial direction of the spherulite because of the lamellar twisting. This is modelled by creating several domains, each with a different orientation of the crystalline layers and then arranging the domains randomly in a three-dimensional periodic structure. Each of the domains has an hexagonal shape, see figure 2.4. In figure 2.4, the model for one particular crystallinity is illustrated. For the calculations, models with different crystallinities are used, where the thickness of the crystalline layers is changed. The crystallinity is thereby varied from 14% to 42%. To obtain a representative structure with a limited number of domains, some restrictions are introduced, creating a quasi-random structure: the number of domains having the same orientation is uniform; the domain can not border with another domain with the same orientation; the average position of the domains with the same orientations should be close to the centre of the μRVE. With these restrictions, a convergence study has shown that a stacking 6×6 domains is sufficient to obtain a macroscopically transversely isotropic μRVE.

The finite-element mesh for a crystallinity of $f^c = 0.26$ is illustrated in figure 2.4 (only the front view of the 3D model). Linear brick and pentahedral elements (which are used near the edges of the hexagonal domains) are used in the model. Crystalline layers are illustrated in grey colour and are oriented according to the growth direction (out of plane) and the normal to the interface between the phases. The restriction that bordering domains can not have the same orientation of the crystalline layers is fulfilled, but not observed in the left figure, since for the same interface normal $\vec{n}$, two orientations of the crystalline phase are possible, which is shown in the right-bottom figure where, the orientations of the crystalline lamellae in the bordering domains are indicated. For details about crystal orientations, see section 2.3.3.

The μRVE is defined in a local coordinate system with the unit vectors $\vec{i}_1, \vec{i}_2, \vec{i}_3$. The geometry of the periodic μRVE is defined by the corner points c_k, $k = \overline{1,4}$ and the corresponding bound-
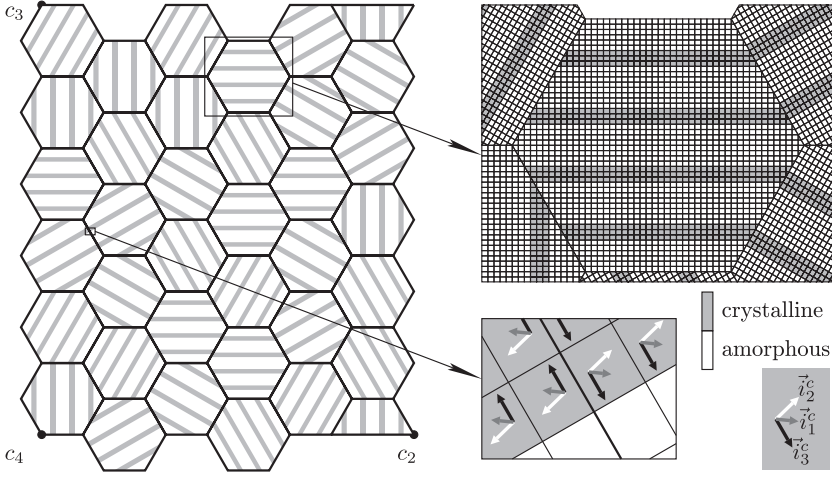
Figure 2.4: The 3D finite-element mesh for the microscale model with crystallinity of $f^c = 0.26$, front view.
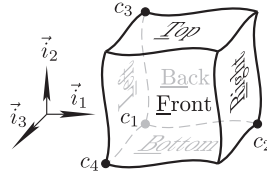
Figure 2.5: Labels used to describe the periodic volume and the periodic boundary conditions.

aries as labelled in figure 2.5. On the boundaries, the following periodic conditions for the μRVE are imposed:

$$\vec{u}^{\mathrm{R}} - \vec{u}^{\mathrm{L}} = \vec{u}^{c_2} - \vec{u}^{c_1}; \tag{2.13}$$

$$\vec{u}^{\mathrm{T}} - \vec{u}^{\mathrm{Bo}} = \vec{u}^{c_3} - \vec{u}^{c_1}; \tag{2.14}$$

$$\vec{u}^{\mathrm{F}} - \vec{u}^{\mathrm{Ba}} = \vec{u}^{c_4} - \vec{u}^{c_1}, \tag{2.15}$$

with $\vec{u}^{c_k}$ the displacements of the corner points, and with $\vec{u}^{c_1} = \vec{0}$.

Following [85], the average deformation gradient $\bar{\boldsymbol{F}}^{\prime\mu\mathrm{RVE}}$ and the average 1$^{\mathrm{st}}$ Piola-Kirchhoff stress tensor $\bar{\boldsymbol{P}}^{\prime\mu\mathrm{RVE}}$, are defined by volume averaging over the domain of the μRVE:

$$\bar{\boldsymbol{F}}^{\prime\mu\mathrm{RVE}} = \frac{1}{V_0^{\mu\mathrm{RVE}}} \int\limits_{v \in V_0^{\mu\mathrm{RVE}}} \boldsymbol{F}(v) \, \mathrm{d}v; \tag{2.16}$$

$$\bar{\boldsymbol{P}}^{\prime\mu\mathrm{RVE}} = \frac{1}{V_0^{\mu\mathrm{RVE}}} \int\limits_{v \in V_0^{\mu\mathrm{RVE}}} \boldsymbol{P}(v) \, \mathrm{d}v. \tag{2.17}$$
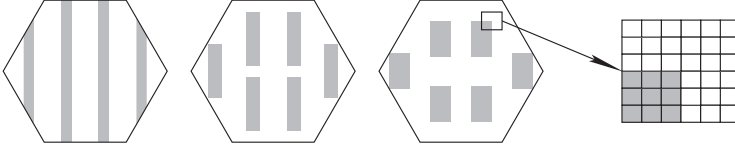
Figure 2.6: Different meshes of the single domain of the μRVE used in the simulation where the crystal geometry is varied; $\psi \approx 12$ (left), 4 (centre), 2 (right).

The deformation gradient $\bar{\boldsymbol{F}}^{\mu\text{RVE}}$ is prescribed through the displacements of the corner points $\vec{u}^{c_k}$, $k = \overline{1,4}$ which can be obtained from:

$$\vec{u}^{c_k} = \left(\bar{\boldsymbol{F}}^{\mu\text{RVE}} - \boldsymbol{I} \right) \cdot \vec{x}^0\left(c_k \right), \quad k = \overline{1,4}, \tag{2.18}$$

with $\vec{x}^0\left(c_k\right)$ the initial position of the point. Based on the periodic boundary conditions, tensor $\bar{\boldsymbol{P}}^{\mu\text{RVE}}$ for the periodic μRVE can be calculated by [85]:

$$\bar{\boldsymbol{P}}^{\mu\text{RVE}} = \frac{1}{V_0} \sum_{k=\overline{1,4}} \vec{f}^k \vec{x}^0\left(c_k\right), \tag{2.19}$$

where V_0 is the initial volume of the μRVE and $\vec{f}^k$ are the resulting external forces at the corresponding corner nodes. The effective elastic properties of the μRVE are obtained from different perturbations of it. However, in large multi-scale analyses obtaining effective properties using static condensations is preferred [86].

The composite inclusion model may be expected to provide an adequate approximation of the mechanical behaviour of material consisting of layered phases, which is most likely for high or moderate crystallinities (which is, for example, the case for fully crystallised PET). In this section, such a structure was described with the two-scale finite-element model. However, at relatively low crystallinities, crystalline lamellae within the spherulite might not border with each other, thus having a different aspect ratio of the cross-section. To study the effect of the crystalline geometry, microstructural finite-element models with varying crystalline aspect ratios (length/width ratios of the cross-section: $\psi \approx 12, 4, 2$) were used, preserving the volume of the crystalline phase and the number of rows with crystalline inclusions in the domain, see figure 2.6. The finite-element mesh of the μRVE (figure 2.4) was modified, by replacing the internal geometry of the domains by the ones in figure 2.6. These models were used to make a comparison with the composite inclusion model at the microscopic scale. In addition, μRVE models with different crystallinities (variation of the volume fraction of the crystalline phase) were created for macroscopic analysis.

Link between scales

The behaviour of the material in the finite-element model is linear elastic. Thus, the effective stress ($\bar{\boldsymbol{\sigma}}$) and strain ($\bar{\boldsymbol{\varepsilon}}$) in the μRVE are related through the anisotropic effective stiffness tensor ${}^4\bar{\boldsymbol{\mathcal{C}}}^{\mu\text{RVE}}$, which is independent of the loading conditions of the μRVE. First, this effective stiffness tensor is extracted from the μRVE. Then, it is used in the spherulite model, considering the orientation of each material point. The coordinate systems of the two models are coupled such that the long axis

of the crystalline lamella in the μRVE (the out of plane direction in figure 2.4) corresponds to the radial direction of a material point in the spherulite structure of the mesoscopic level model (the directions are indicated by $\vec{i}_3$ in figure 2.2). The rotation of lamellae around the radial direction of the spherulite is random. Thus, to obtain a uniform distribution of the interface normals, an additional random rotation of the local coordinate system around the direction $\vec{i}_3 = \vec{e}_r$ is introduced. The final step is to obtain the effective stiffness from the spherulite model ${}^4\overline{\boldsymbol{\mathcal{C}}}^{\mathrm{SM}}$. The mesoscopic scale also represents the effective behaviour of a material point at the macroscopic (application) scale. Thus, in the application scale, ${}^4\overline{\boldsymbol{\mathcal{C}}}^{\mathrm{Macro}} = {}^4\overline{\boldsymbol{\mathcal{C}}}^{\mathrm{SM}}$ can be used.

To analyse microscopic deformations, the spherulite model is subjected to the following boundary conditions (uniaxial stress state):

$$\bar{\varepsilon}_{11} = 0.01; \quad \bar{\sigma}_{ij} = 0, \quad i,j = \overline{1,3}, ij \neq 11. \tag{2.20}$$

The deformation gradient obtained from the results of the spherulite model analysis is taken from $N = 35$ material points and the corresponding boundary conditions are imposed on the μRVE model. After that, the average stresses and strains over the individual phases of the domains having the same orientation (i.e. the normal to the interface between the phases is the same) are obtained.

2.3.3 Behaviour of constituent phases

The elastic behaviour of each of the phases is represented by Hooke's law, $\boldsymbol{\sigma} = {}^4\boldsymbol{\mathcal{C}} : \boldsymbol{\varepsilon}$. Using the Voigt notation, the stress and strain tensors are stored in the columns:

$$\underset{\sim}{\sigma} = [\sigma_{11}, \sigma_{22}, \sigma_{33}, \sigma_{23}, \sigma_{31}, \sigma_{12}]^{\mathrm{T}},$$

$$\underset{\sim}{\varepsilon} = [\varepsilon_{11}, \varepsilon_{22}, \varepsilon_{33}, 2\varepsilon_{23}, 2\varepsilon_{31}, 2\varepsilon_{12}]^{\mathrm{T}},$$

respectively, which are linked by the matrix $\underset{\sim}{C}$.

The crystal structure of PET is triclinic and is shown in figure 2.7. The experimentally determined parameters from [24] are used here: $a = 0.456$ nm, $b = 0.594$ nm, $c = 1.075$ nm, $\alpha = 98.5°$, $\beta = 118°$, $\gamma = 112°$. A local coordinate system is defined for the crystal unit cell, such that $\vec{i}_3^c$ corresponds to the chain direction (the [001] crystallographic direction) and $\vec{i}_2^c$ is orthogonal to $\vec{i}_3^c$ and lies in the (100) crystallographic plane; $\vec{i}_1^c$ is then obtained from the following vector product: $\vec{i}_1^c = \vec{i}_2^c \times \vec{i}_3^c$.

For the crystalline phase, the following stiffness matrix, obtained by molecular modelling [25] (at ambient temperature 300 K), is used:

$$\underset{\sim}{C}^{\mathrm{c}} = \begin{pmatrix} 14.4 & 6.4 & 3.4 & -2.2 & -0.3 & -1.8 \\ 6.4 & 17.3 & 9.5 & 3.3 & -0.5 & 0.5 \\ 3.4 & 9.5 & 178.0 & 3.8 & -0.7 & -1.8 \\ -2.2 & 3.3 & 3.8 & 6.6 & 0.2 & -0.4 \\ -0.3 & -0.5 & -0.7 & 0.2 & 1.4 & 0 \\ -1.8 & 0.5 & -1.8 & -0.4 & 0 & 1.2 \end{pmatrix} \text{ GPa.} \tag{2.21}$$

This is in contrast to [53, 68], where the stiffness matrix is taken from an experimental study [87] with the C_{33}^{c} component obtained from [88].
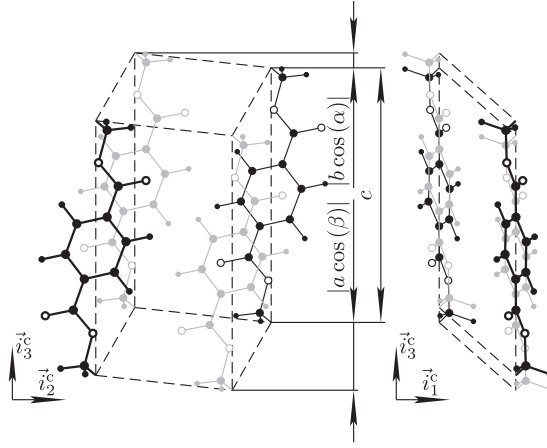
Figure 2.7: Arrangement of chains in a PET crystal, front view (left) and left view (right); carbon atoms are shown with large dots, hydrogen with small dots, and oxygen atoms with open circles, atomic positions are taken from [26].

Table 2.1: Experimentally measured Young's moduli for amorphous PET.

Source	[68]	[91]	[92]	[93]	[94]
Temperature [°C]	20–26	20	80	46–77	21
Young's modulus [GPa]	2.6	1.22	1.65	2	2.2

The orientation of the crystallographic unit cell is specified relative to the crystalline-amorphous interface, i.e. the lamellar surface. The [101] crystallographic direction is considered to be the normal to the lamellar surface [10, 26, 89]. For the above mentioned lattice parameters, the angle between the molecular chain axis and the lamellar normal is $\varphi \approx 25°$. Single crystals of PET are lath-shaped with long dimension of the lamella parallel to the (010) crystallographic plane [10]. The preferred crystal growth plane is the (100) crystallographic plane [84]. Thus, for the finite-element model, the spherulite growth direction is selected to be normal to the [101] direction and lying in (010) plane, as shown in figure 2.8. Therefore, the growth direction is close to the crystallographic a-axis. Also, in polytrimethylene terephthalate, which belongs to the same terephthalic polyester family as PET, the spherulite growth direction is the crystallographic a-axis [90].

The amorphous phase is assumed to be isotropic [20]. However, different studies have shown a large variation of the Young's modulus for amorphous PET [68, 91–94], which can be found in table 2.1. For comparing the two models, a Young's modulus of $E^{\mathrm{a}} = 2\,\mathrm{GPa}$ is used. Following [68], the Poisson's ratio is taken as $\nu^{\mathrm{a}} = 0.4$.
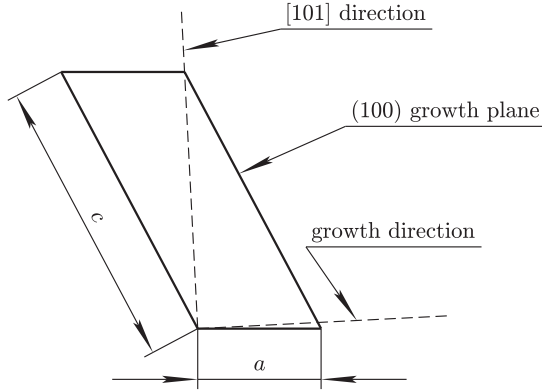
Figure 2.8: Schematic illustration of the (010) plane of the PET crystal unit cell (lattice parameters from [24]).

2.4 Results

2.4.1 Macroscopic comparison

To obtain the effective Young's modulus of the material from the composite inclusion model, the number of inclusions was set to 2000, with a random orientation distribution. The effective stiffness tensors, corresponding to different interaction laws between the inclusions, were obtained using relations given in [77]. For the finite-element model, 5 crystallinities were selected and for each crystallinity, 6 calculations were done for both the bcc model and the cubic model, each time with different random orientations of the domains.

    The dependence of the macroscopic Young's modulus on the crystallinity is illustrated in figure 2.9 for the various models. Here, the highest aspect ratio of the crystalline phase within the domain is used, i.e. the μRVE is a packed layered structure. As observed from the image, there is almost no difference between results obtained with the finite-element models having a cubic or a bcc stacking of spherulites. Also, the composite inclusion model with a hybrid interaction law predicts almost the same stiffness as the finite-element models. The Young's moduli, obtained with the composite inclusion model with various interaction laws, extrapolate to $E^{\mathrm{a}} = 2\,\mathrm{GPa}$ for a crystallinity of $f^{\mathrm{c}} = 0$.

2.4.2 Microscopic comparison

The composite inclusion model also predicts the stresses and strains in the individual phases of single inclusions, which are next compared with the results of the finite-element simulations at the microscopic scale. Intralamellar deformation ($\varepsilon^{\mathrm{c}} = \sqrt{\frac{2}{3}\boldsymbol{\varepsilon}^{\mathrm{c}} : \boldsymbol{\varepsilon}^{\mathrm{c}}}$), interlamellar separation ($\varepsilon_n^{\mathrm{a}} = \boldsymbol{\varepsilon}^{\mathrm{a}} : \vec{n}^{\mathrm{I}}\vec{n}^{\mathrm{I}}$) and interlamellar shear ($\gamma_n^{\mathrm{a}} = \left|\boldsymbol{\varepsilon}^{\mathrm{a}} \cdot \vec{n}^{\mathrm{I}} - \varepsilon_n^{\mathrm{a}}\vec{n}^{\mathrm{I}}\right|$) normalised by $\bar{\varepsilon}_{11}$ are used as the measures of the deformation. The orientations of the lamellar interface normals and the corresponding strain measures (in greyscale) are illustrated in equal area projection pole figures in figure 2.10 for the composite inclusion model with the hybrid interaction law and for the finite-element model
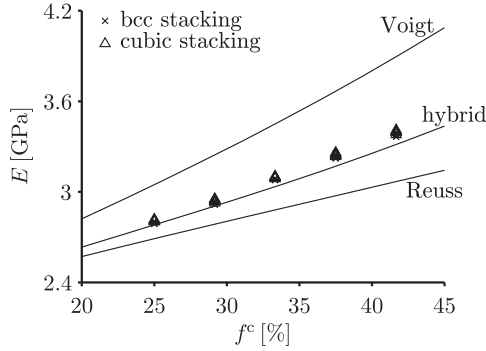
Figure 2.9: The dependence of the macroscopic Young's modulus on the crystallinity for isotropic PET calculated with the composite inclusion model using various interaction laws (lines) and with the finite-element model (symbols).

with cubic stacking of the spherulites and highest aspect ratios of crystalline layers. Crystallinity was taken as $f^c = 0.25$, which corresponds to the maximum crystallinity achieved experimentally by annealing. In the spherulite model 27 points were taken for the analysis, with coordinates $x_1, x_2, x_3 \in \{0.1; 0.5; 0.9\}$. The average strains of each amorphous and crystalline layer in the domains of the particular orientation are calculated as the volume averages. From the figures it can be observed, that the relations between the magnitude of the deformation measures, and the lamellar normal orientations, are similar in both models.

In figure 2.11 von Mises stress distributions in the spherulite model and two μRVEs corresponding to different points as well as the pole figures showing deformation measures are shown. The deformation throughout the spherulite model is heterogeneous. The deformation mechanisms, which are dominant in different areas of the model, are identified by pole figures, showing these measures, as a function of the lamellar normal orientations in the μRVE, for single points located at various positions of the spherulite model. The colours of the markers in the pole figures indicate the magnitude of the deformation measure (intralamellar deformation or interlamellar shear or separation) and the locations of the markers show the corresponding orientations of the lamellar normals. At the macroscopic scale, the deformation is applied in $\vec{e}_1$-direction, equation (2.20). Here 8 additional points in the spherulite model are further analysed; coordinates of the points are $x_1, x_2, x_3 \in \{0; 1\}$. For points in the "Left" plane of the spherulite model and neighbouring points (as defined in figure 2.5), the dominant deformation mechanism, observed at the microscopic scale, is interlamellar separation for the domains with the lamellar normals oriented along the $\vec{e}_1$-direction. For normals lying in the plane normal to $\vec{e}_1$ it is intralamellar deformation, and for other normal orientations it is interlamellar shear (see upper pole figures in figure 2.11). For points in the "Right" plane of the spherulite model and neighbouring points, which are distant from point "c_2" (see figure 2.5), where in the corresponding μRVEs domains have lamellar normals, which are oriented along the normal to the plane spanned by $\vec{e}_r$ and $\vec{e}_1$ (with $\vec{e}_r$ being the radial vector from the centre of the spherulite, point "c_1", to the current point) the dominant deformation mechanism is intralamellar deformation; for normals lying in the plane spanned by $\vec{e}_r$ and $\vec{e}_1$, it is interlamellar separation and interlamellar shear; for the rest of the normal orientations, the main mechanism of deformation is interlamellar shear (see lower pole figures in figure 2.11). For points in the neighbour-
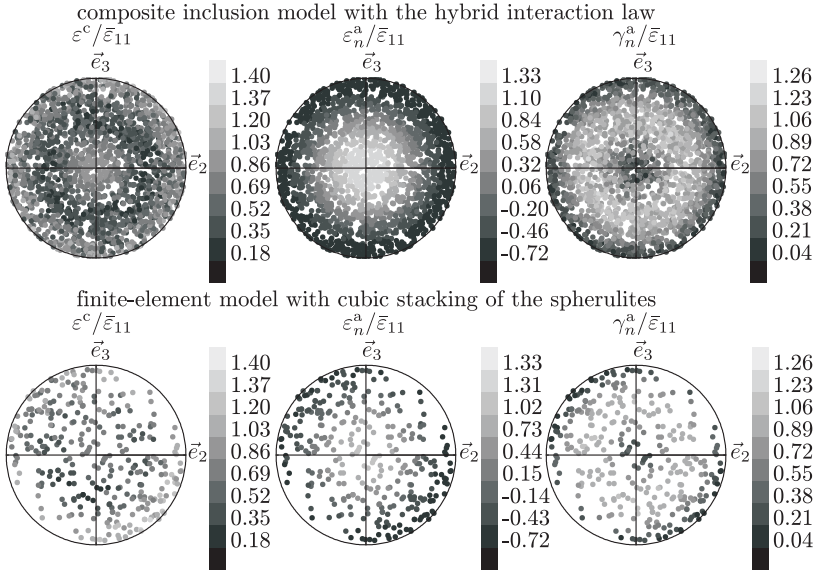
Figure 2.10: Equal area projection pole figures of lamellar normal orientations, showing local deformation measures, normalised by $\bar{\varepsilon}_{11}$.

hood of the $\vec{e}_1$-axis in the spherulite model, the dominant deformation mechanism in the domains of the corresponding μRVE is intralamellar deformation with negative interlamellar separation independent of the lamellar normal orientation. Similar inhomogeneous deformations were found in spherulitic structures of PE, where the behaviour of a bundle of twisted lamellae in a material point was modelled with the composite inclusion model [78].

2.4.3   Crystal geometry variation

As outlined in section 2.3.2, various crystalline geometries were used for relatively low crystallinities. In particular, the internal geometry of the domains in the μRVE was replaced with geometries containing crystalline layers with lower aspect ratios (see figure 2.6). For a microscopic comparison between the models with different internal geometries of the μRVE, the same crystallinity $f^c = 0.25$ was used. The number of rows with crystalline inclusions in the domain was also kept constant. For a macroscopic comparison the crystallinity was varied.

The resulting macroscopic elastic moduli, obtained from the finite-element model, are plotted in figure 2.12. The Young's modulus decreases slightly with a decrease of the aspect ratio. Thus, for all crystalline geometries, the macroscopic behaviour is relatively close to the prediction obtained with the composite inclusion model.

At the microscopic level, the stress distribution in the μRVE is changing with the aspect ratio of the crystalline layers. The same comparison as in section 2.4.2 was made, only domains in the μRVE were replaced by domains containing crystalline layers with lower aspect ratios. The type of boundary conditions influences how much the stress distributions in various μRVE models differ. If the boundary conditions are such that no significant volumetric strains are imposed on the μRVE,
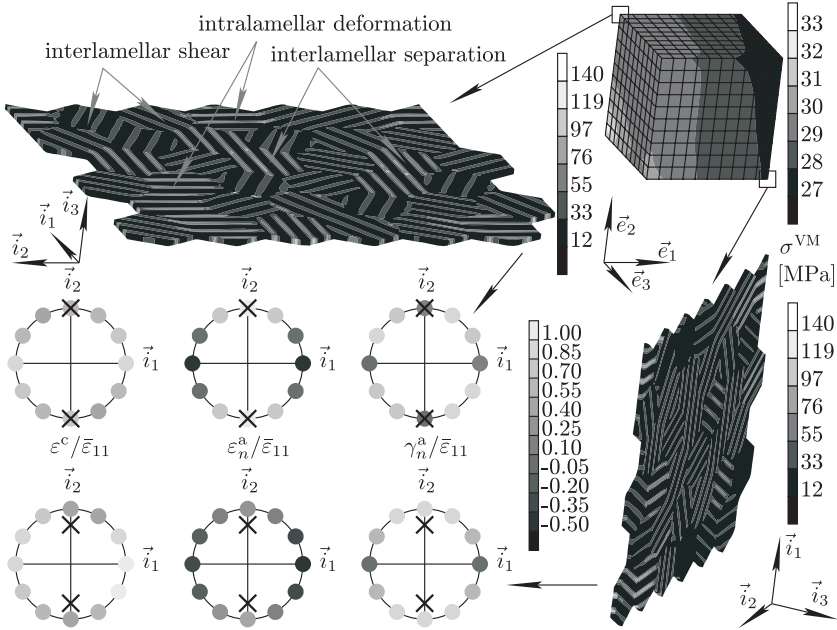
Figure 2.11: Von Mises stress distribution in the spherulite model (upper right) and two μRVEs (upper left and lower right) corresponding to two points of the spherulite model. The deformation measures in the μRVEs are shown in the pole figures: normalised intralamellar deformation (left), normalised interlamellar separation (centre), normalised interlamellar shear (right). The symbols $\bullet$ in the pole figures indicate the orientation of lamellar normals (the magnitude of the deformation measure is shown in colour); the symbols $\times$ indicate the loading direction.

then the stress distributions between phases show roughly the same pattern when various aspect ratios are used. In figure 2.13, the results of μRVEs with different aspect ratios of the crystalline layers, corresponding to point $(0.1, 0.1, 0.9)$ in the spherulite model, are shown. The boundary conditions for the spherulite model are the same as in section 2.4.2. In figures 2.14 and 2.10, it can be observed that the deformation measures (averaged within the layer) are the same for all aspect ratios (in figure 2.10, aspect ratio $\psi \approx 12$ was used in the μRVE). If the imposed boundary conditions contain sufficient volumetric strain, then for the case of the layered structure ($\psi \approx 12$), the stress is mostly accumulated in the crystalline region since it forms an interconnected network. For μRVEs where crystalline regions have a lower aspect ratio, the stress distribution is more homogeneous and the average stress in crystalline layers is lower.

In section 2.4.2, it was shown that the composite inclusion model gives a good estimation of the microscopic characteristics, compared to finite-element simulation, where the μRVE was composed of layered domains. It is therefore concluded that the composite inclusion model can be also applied in cases when separate crystalline layers do not border with each other, at least if macroscopic boundary conditions do not impose large volumetric strains.
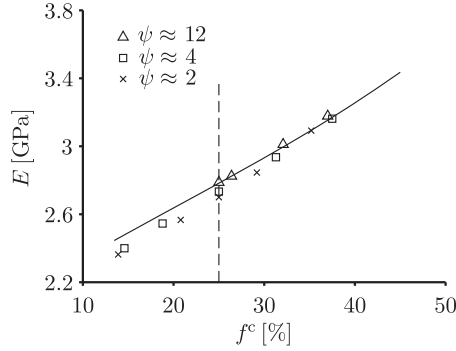
Figure 2.12: The dependence of Young's modulus on crystallinity calculated with the composite inclusion model using the hybrid interaction law (line) and with the finite-element model (symbols). In the finite-element model, in the μRVE, various geometries of the crystalline layers were used. Macroscopic Young's modulus of the models that were used in the microscopic comparison are indicated by vertical dashed line.
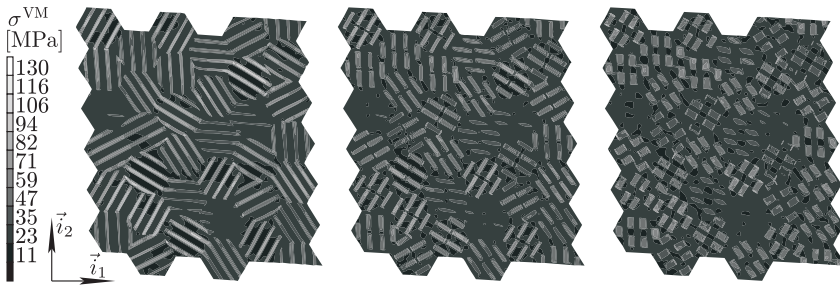
Figure 2.13: Von Mises stress distribution in three μRVEs with different aspect ratios of the crystalline layers ($\psi \approx 12, 4, 2$ from right to left). The deformed shape is shown (magnified with a factor of 9).

2.4.4 Experimental validation

As described in section 2.2, a series of tensile tests was performed on samples with varying crystallinity to validate the model results. The results are illustrated in figure 2.15. For the composite inclusion model, the Young's modulus of the non-crystalline region was taken to be either $E^{\mathrm{a}} = 1.22\,\mathrm{GPa}$ or $2.6\,\mathrm{GPa}$, the lowest and highest values found in literature, respectively (see table 2.1). If $E^{\mathrm{a}} = 1.9\,\mathrm{GPa}$, the average of the highest and lowest estimates of E^{a}, there is a good agreement between experimental and modelling results, as observed from figure 2.15. Note that although the range of crystallinities in the experimental validation is somewhat different from the range used in the finite-element validation, the ranges are overlapping in the region from 14% to 27%.
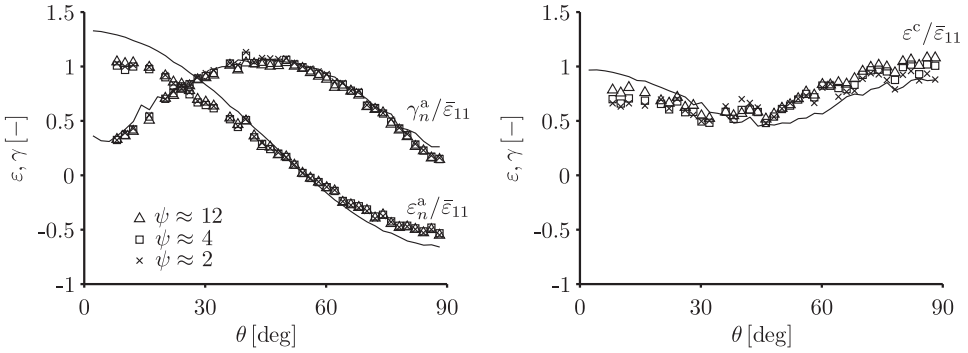
Figure 2.14: The dependence of local deformation measures, normalised by $\bar{\varepsilon}_{11}$, on angle (θ) between the loading direction and the orientation of the interface ($\vec{n}^{\mathrm{I}}$). The composite inclusion model with the hybrid interaction law (line) is compared with the finite-element model (symbols). In the finite-element model, in the μRVE, various geometries of the crystalline layers were used.
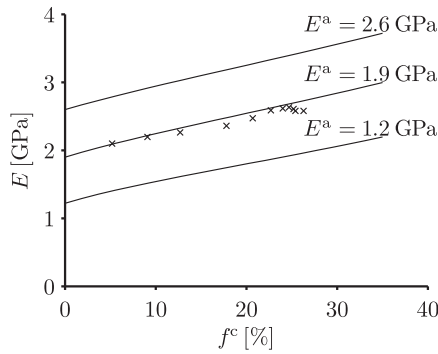
Figure 2.15: Dependence of Young's modulus on crystallinity. Predictions of the composite inclusion model with the hybrid interaction law (lines) compared to experiments (symbols).

2.5 Conclusions

In this work, the elastic behaviour of PET was modelled using different approaches. A two-scale finite-element model of a spherulitic semicrystalline microstructure was developed and compared with the existing composite inclusion model. The composite inclusion model represents a layered structure approach, whereas in the finite-element model various microstructures were used: a layered one and microstructures containing crystalline layers with smaller aspect ratios, which are more likely to be found in a semicrystalline polymer at relatively low crystallinity.

The results indicate that the composite inclusion model can be used for modelling the elastic behaviour of isotropic PET. The numerical validation, consisting of a comparison of the elastic

moduli at the macroscopic scale and the deformation measures at the microscopic scale, showed that the composite inclusion model with the hybrid interaction law gives results that are close to those obtained with a more detailed model taking into account the spherulitic geometry. At low crystallinities, different aspect ratios of the crystalline phase were used in the finite-element model, which resulted in a macroscopic elastic behaviour close to the composite inclusion model. At the microscopic scale, no significant differences were observed in the stress distribution within the microstructure when the layered structure was replaced with an amorphous matrix containing single crystals with a lower aspect ratio. From a microscopic point of view, the composite inclusion model with the hybrid interaction law remains valid when aspect ratios of the crystals are small.

Experimental validation further proved that the two-phase composite inclusion model gives an adequate approximation of the macroscopic material behaviour of PET.

The current analysis is based on linear elasticity and the conclusions therefore only hold for this regime. The same approach can be extended to the large-strain viscoplastic regime. For this regime, a viscoplastic mean-field composite inclusion model has previously been developed in which the crystalline phase deforms by crystallographic slip [81, 83]. The finite element analysis would then require the same constitutive behaviour of the constituent phases.

3 Short-term and long-term large-strain behaviour of isotropic semicrystalline PET[*]

Abstract: A micromechanically based model is used to describe the mechanical behaviour of polyethylene terephthalate under uniaxial compression up to large strains and at different temperatures. The creep behaviour of isotropic PET is simulated and compared to experimental data to demonstrate the applicability of the model to describe the long-term response. The material is modelled as an aggregate of two-phase layered domains, where different constitutive laws are used for the phases. A hybrid interaction law between the domains is adopted. The crystalline phase is modelled with crystal plasticity and the amorphous phase with the Eindhoven Glassy Polymer model, taking into account material ageing effects. Model parameters for the selected constitutive laws of the phases are identified from uniaxial compression tests for fully amorphous material and semicrystalline material. Texture evolution during the deformation predicted by the model adequately matches previously observed texture evolution.

3.1 Introduction

Understanding and predicting the dimensional stability of various polymers used in the manufacture of flexible electronics is essential for the production process [4]. Among the materials used as the substrate for electronic circuits are polyethylene terephthalate (PET) and polyethylene naphthalate (PEN), which can both exist in amorphous or semicrystalline states. Films used in the manufacturing process are semicrystalline, oriented and thermally stabilised. The goal of this work is to obtain a structure-property relationship, i.e. unravel the macroscopic behaviour of the deforming polymer in terms of its microstructural characteristics such as crystallinity, activity of different molecular relaxation processes in the amorphous phase, activity of the slip systems in the crystalline phase or phase interaction.

Semicrystalline polymers are intrinsically heterogeneous materials and rather complicated to model, therefore the variety of approaches is wide. Phenomenological models, such as the model by Buckley et al. [38] (also in application to PET [96]), the model by Boyce et al. [97] or a modification thereof [47], describe the large-strain behaviour of PET at the macroscopic scale even for

---

[*]This chapter is partly reproduced from [95].

the case of oriented polymers using orientation distribution functions as internal state variables. However they are not able to provide precise information about the texture evolution and deformation mechanisms of the phases. Another approach is multi-scale finite-element modelling of the large-strain behaviour of the polymer with known structure, i.e. isotropic (spherulitic) or oriented. One example of such an approach, applied to the viscoplastic deformation of spherulitic polyethylene, can be found in [50]. Another example is a model for the elastic deformation of a spherulitic microstructure of PET (see chapter 2). A different class of methods is based on mean-field homogenisation techniques for the amorphous and crystalline domains. In this case, the real interaction between the domains is replaced with an effective interaction model, and the average material response is obtained through homogenisation. The most well-known mean-field approaches are rules of mixtures (such as Voigt and Reuss averages), the self-consistent method [54] and the Mori-Tanaka method [58, 59]. The latter two methods were originally developed for the case of elastic deformation. Hybrid methods between the Voigt and Reuss interaction laws have been used in models capturing a viscoplastic response. One example of such a model is the so-called composite inclusion model [73, 74, 83], which was applied to the large-strain deformation of HDPE. In this model, the material behaviour is obtained by averaging the response of layered domains, consisting of crystalline and amorphous phases, and assuming a certain interaction law between the domains. This model was used in a multi-scale approach to model the spherulitic morphology of polyethylene [78] and the behaviour of a tensile bar under uniaxial stress [79]. In [80] a double yield phenomenon in the predicted response of polyethylene was observed, and in [81] this model was used to simulate the creep behaviour and predict the time-to-failure of polyethylene.

The different phases in a micromechanical model are described by dedicated constitutive laws. For the crystalline phase, crystal plasticity [98] is commonly used, where viscoplastic deformation takes place on a limited number of slip systems. The constitutive behaviour of the amorphous phase can be described with one of the existing models for the large-strain behaviour of amorphous polymers in the glassy state [37, 40, 41]. In this work, the model by Govaert et al. [41], which is referred to as the Eindhoven Glassy Polymer (EGP) model, is adopted.

The aim of this work is to model the micromechanical deformation and macroscopic response of PET during compression and creep up to moderately large strains and to obtain the parameters required for the constitutive models for the amorphous and crystalline phases. For this purpose, for the first time, a multi-process and multi-mode elastic-viscoplastic model for the mechanical response of the amorphous phase based on the EGP model is incorporated in the framework of a micromechanical model for semicrystalline polymers. Details on the numerical implementation of the model are given, as well as the procedure for identifying its parameters. The parameters of both phases of the mechanical model are systematically determined to quantitatively describe the viscoplastic response of PET based on the underlying micromechanics. Texture evolution during large-strain compressive deformation is analysed. The creep behaviour of isotropic PET with different crystallinities is simulated and compared to experimental data to demonstrate the applicability of the model to describe the long-term response.

In oriented films, a preferential orientation of the crystals exists, requiring details of the orientation distribution of the crystalline phase to properly characterise the material. Therefore, in the current work, the characterisation is performed on isotropic, melt-crystallised PET, which was further annealed in an oven to obtain a semicrystalline state. In this case, the material is isotropic and possesses a spherulitic microstructure [12]. After characterisation is performed, the model can be used to describe the behaviour of oriented films.

3.2 Experimental methods

Injection molded bars of 6 mm in diameter and 10 cm in length were prepared from a polyethylene terephthalate, which was obtained from Eastman and had a molecular weight of 52000 g/mol. The bars were wrapped in aluminium film and kept at 90 °C for 10 minutes to remove orientation. To create semicrystalline samples, the bars were annealed in an oven for 1.5 and 24 hours at 100 °C, achieving an approximate volume crystallinity of 5% and 30% respectively. Cooling down was performed by quenching. Cylinder-shape samples of amorphous and semicrystalline PET, 4 mm in diameter and 4 mm in height, were cut from these bars. Crystallinity was measured using DSC and X-ray techniques.

   True strain-controlled uniaxial compression tests were performed on a Zwick Universal Testing Machine 1475. The samples were subjected to compression at true strain rates of 10^{-2}, 10^{-3} and $10^{-4}\,\mathrm{s}^{-1}$ and temperatures of 23, 40, and 60 °C. To avoid barreling, PTFE adhesive tape (3M 5480 HD) was attached to the samples on both sides. The true stress-strain curve was recorded.

   For creep tests, PET cast film with an initial crystallinity less than 1%, supplied by DuPont Teijin Films (experimental grade) was used. The samples were cut from sheets of the film and were annealed at 100 °C for 6 and 13 hours. The geometrical shape of the samples was according to ISO 527-2, type 1BA. To flatten the samples, they were placed between aluminium plates. Also, to prevent surface pitting, polyamide film was placed between the samples and outer aluminium plates. Tensile creep tests of the samples were carried out on a Zwick Z010 tensometer at 30 °C with 5 MPa imposed stress.

3.3 Model formulation

3.3.1 Micromechanical model

A mean-field micromechanical model, referred to as the composite inclusion model, is used to simulate the mechanical behaviour of semicrystalline PET. The composite inclusion model [83] is a material point model which allows the macroscopic deformation gradient $\boldsymbol{F}^{\mathrm{M}}$ and Cauchy stress $\boldsymbol{\sigma}^{\mathrm{M}}$ to be related to the micromechanical deformation mechanisms and structure. Separation of scales is thus introduced with the macroscopic scale being the material point level and the microscopic scale corresponding to individual crystalline and amorphous domains.

   At the microscopic scale, the basic structural element is the composite inclusion, which consists of a crystalline lamella and a neighbouring amorphous layer, see figure 3.1. A collection of inclusions, each with a certain orientation, is generated. Note that the term "composite inclusion", introduced by [73, 74], refers to the use of this layered domain in an aggregate of such objects in a mean-field approach. The constitutive behaviour of the phases is described below, where each phase has a uniform deformation gradient and Cauchy stress. Compatibility and equilibrium requirements at the interface are imposed. The deformation gradient $\boldsymbol{F}^{\mathrm{I}}$ and Cauchy stress $\boldsymbol{\sigma}^{\mathrm{I}}$ of the inclusion are determined by volume averaging of the corresponding quantities of the phases. Macroscopic quantities $\boldsymbol{F}^{\mathrm{M}}$ and $\boldsymbol{\sigma}^{\mathrm{M}}$ are obtained by averaging $\boldsymbol{F}^{\mathrm{I}}$ and $\boldsymbol{\sigma}^{\mathrm{I}}$ of all inclusions.

   To link inclusion quantities to macroscopic quantities, an interaction law is used [73, 74, 83]. In current simulations, the $\hat{\boldsymbol{U}}$ interaction law is employed, in which a mixture of global-local compatibility and equilibrium conditions is implied. More details can be found in the appendix and in [83]. The spherulitic assembly of the lamellae, as exists in the studied material, is modelled a
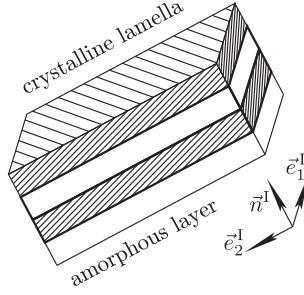
Figure 3.1: The two-layer composite inclusion after [73, 83]. The structural unit of the model is highlighted in a stack of crystalline lamellae.

mean-field approach, i.e. only orientations of crystalline lamella are taken into account, but not the spatial arrangement. The effect of latter was previously investigated in chapter 2 and in [78].

3.3.2   Crystalline phase

A multiplicative decomposition of the deformation gradient into elastic (e) and plastic (p) parts is assumed (superscript "c" indicates a quantity corresponding to the crystalline phase):

$$\boldsymbol{F}^{\mathrm{c}} = \boldsymbol{F}_{\mathrm{e}}^{\mathrm{c}} \cdot \boldsymbol{F}_{\mathrm{p}}^{\mathrm{c}}. \tag{3.1}$$

In addition to the initial configuration Ω_0 and current configuration Ω, an intermediate configuration Ω_{i}, resulting from instantaneous elastic unloading of the current configuration to a stress-free state, is introduced. The volumetric deformation is considered to be fully elastic:

$$J^{\mathrm{c}} = \det(\boldsymbol{F}^{\mathrm{c}}) = J_{\mathrm{e}}^{\mathrm{c}} = \det(\boldsymbol{F}_{\mathrm{e}}^{\mathrm{c}}). \tag{3.2}$$

The elastic behaviour is characterised by the second Piola-Kirchhoff stress tensor with respect to the intermediate configuration $\boldsymbol{S}_{\mathrm{e}}^{\mathrm{c}}$ and the elastic Green-Lagrange strain tensor $\boldsymbol{E}_{\mathrm{e}}^{\mathrm{c}}$, which are coupled in the following way:

$$\boldsymbol{S}_{\mathrm{e}}^{\mathrm{c}} = {}^{4}\boldsymbol{\mathcal{C}}^{\mathrm{c}} : \boldsymbol{E}_{\mathrm{e}}^{\mathrm{c}}, \tag{3.3}$$

where ${}^{4}\boldsymbol{\mathcal{C}}^{\mathrm{c}}$ is a fourth order tensor containing the elastic parameters of the crystalline phase, and

$$\boldsymbol{S}_{\mathrm{e}}^{\mathrm{c}} = J^{\mathrm{c}} \boldsymbol{F}_{\mathrm{e}}^{\mathrm{c}-1} \cdot \boldsymbol{\sigma}^{\mathrm{c}} \cdot \boldsymbol{F}_{\mathrm{e}}^{\mathrm{c}-\mathrm{T}} \quad \text{and} \quad \boldsymbol{E}_{\mathrm{e}}^{\mathrm{c}} = \frac{1}{2}\left(\boldsymbol{F}_{\mathrm{e}}^{\mathrm{c}\,\mathrm{T}} \cdot \boldsymbol{F}_{\mathrm{e}}^{\mathrm{c}} - \boldsymbol{I}\right). \tag{3.4}$$

Here $\boldsymbol{\sigma}^{\mathrm{c}}$ is the Cauchy stress tensor and $\boldsymbol{I}$ is the second order identity tensor. Elastic properties of the crystalline phase, i.e. components of tensor ${}^{4}\boldsymbol{\mathcal{C}}^{\mathrm{c}}$, are taken with respect to the crystallographic axes in the intermediate configuration Ω_{i}.

A crystal viscoplasticity model is used for the viscoplastic behaviour of the crystalline phase. Plastic deformation of the crystalline lamella, which constitutes a single crystal, is a superposition of plastic deformations on N^{s} distinct slip systems. Each slip system α in the crystal is described by slip direction $\vec{s}_0^{\alpha}$ and slip plane normal $\vec{n}_0^{\alpha}$, defined in the reference configuration Ω_0. Thus, the
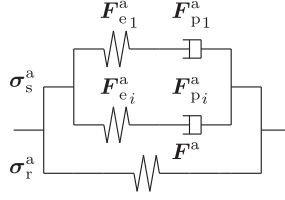
Figure 3.2: Mechanical analogue of the EGP model.

plastic velocity gradient tensor is defined as (symbol "ˆ" indicates a quantity corresponding to the intermediate configuration):

$$\hat{\boldsymbol{L}}_{\mathrm{p}}^{\mathrm{c}} = \dot{\boldsymbol{F}}_{\mathrm{p}}^{\mathrm{c}} \cdot \boldsymbol{F}_{\mathrm{p}}^{\mathrm{c}\,-1} = \sum_{\alpha=1}^{N^{\mathrm{s}}} \dot{\gamma}^{\alpha} \boldsymbol{P}_0^{\alpha}; \quad \boldsymbol{P}_0^{\alpha} = \vec{s}_0^{\alpha} \vec{n}_0^{\alpha}, \tag{3.5}$$

where $\boldsymbol{P}_0^{\alpha}$ is the nonsymmetric Schmid tensor defined in the reference configuration Ω_0 and $\dot{\gamma}^{\alpha}$ is the shear rate of slip system α. Note that the Schmid tensor will also be the same in the intermediate configuration, since $\vec{s}_0^{\alpha}$ and $\vec{n}_0^{\alpha}$ do not change from reference to intermediate configurations. The shear rate is obtained from the resolved shear stress on the slip system with an Eyring flow rule:

$$\dot{\gamma}^{\alpha} = \xi^{\alpha} \sinh \frac{\tau^{\alpha}}{\tau_0^{\alpha}}, \tag{3.6}$$

where ξ^{α} and τ_0^{α} are the reference shear rate and shear strength, respectively. The shear stress τ^{α} on slip system α is defined as [98]:

$$\tau^{\alpha} = \boldsymbol{\tau}^{\mathrm{c}} : \boldsymbol{P}^{\alpha}, \quad \text{with} \quad \boldsymbol{P}^{\alpha} = \boldsymbol{F}_{\mathrm{e}}^{\mathrm{c}} \cdot \boldsymbol{P}_0^{\alpha} \cdot \boldsymbol{F}_{\mathrm{e}}^{\mathrm{c}\,-1} \quad \text{and} \quad \boldsymbol{\tau}^{\mathrm{c}} = J^{\mathrm{c}} \boldsymbol{\sigma}^{\mathrm{c}}. \tag{3.7}$$

3.3.3 Amorphous phase

For describing the non-linear behaviour of the amorphous phase in a glassy state, the EGP model [42, 43, 99] is used. The one-dimensional mechanical analogue of the model is depicted in figure 3.2. The multi-mode multi-process formulation of this model [46] gives a more precise description of the pre-yield behaviour while being less computationally efficient than its single mode version. However, it is not necessary to use a large number of modes if the pre-yield behaviour is mostly linear, as the case for PET.

For each mode i, the deformation gradient $\boldsymbol{F}^{\mathrm{a}}$ is decomposed into elastic and plastic parts (superscript "a" indicates a quantity corresponding to the amorphous phase):

$$\boldsymbol{F}^{\mathrm{a}} = \boldsymbol{F}_{\mathrm{e}_i}^{\mathrm{a}} \cdot \boldsymbol{F}_{\mathrm{p}_i}^{\mathrm{a}}, \quad i = \overline{1, N^{\mathrm{a}}}, \tag{3.8}$$

where N^{a} is the number of modes. To ensure uniqueness of the decomposition of the deformation gradient, the plastic deformation is assumed to be spin-free [41]:

$$\boldsymbol{\Omega}_{\mathrm{p}_i}^{\mathrm{a}} = \frac{1}{2} \left(\boldsymbol{L}_{\mathrm{p}_i}^{\mathrm{a}} - \boldsymbol{L}_{\mathrm{p}_i}^{\mathrm{a}\ \mathrm{T}} \right) = \boldsymbol{0}, \quad \text{with} \quad \boldsymbol{L}_{\mathrm{p}_i}^{\mathrm{a}} = \boldsymbol{F}_{\mathrm{e}_i}^{\mathrm{a}} \cdot \dot{\boldsymbol{F}}_{\mathrm{p}_i}^{\mathrm{a}} \cdot \boldsymbol{F}_{\mathrm{p}_i}^{\mathrm{a}\ -1} \cdot \boldsymbol{F}_{\mathrm{e}_i}^{\mathrm{a}\ -1}. \tag{3.9}$$

Also for the amorphous phase, plastic deformation occurs without volume change, i.e. $J^{\mathrm{a}} = J_{\mathrm{e}\,i}^{\mathrm{a}}, i = \overline{1, N^{\mathrm{a}}}$. The Cauchy stress is split into a hardening stress $\boldsymbol{\sigma}_{\mathrm{r}}^{\mathrm{a}}$ and a driving stress $\boldsymbol{\sigma}_{\mathrm{s}}^{\mathrm{a}}$, which, in turn, is split into a hydrostatic part and a deviatoric part:

$$\boldsymbol{\sigma}^{\mathrm{a}} = \boldsymbol{\sigma}_{\mathrm{r}}^{\mathrm{a}} + \boldsymbol{\sigma}_{\mathrm{s}}^{\mathrm{a\,h}} + \boldsymbol{\sigma}_{\mathrm{s}}^{\mathrm{a\,d}}. \tag{3.10}$$

The driving stress depends on the elastic parts of the deformation gradient of each mode:

$$\boldsymbol{\sigma}_{\mathrm{s}}^{\mathrm{a\,h}} = -p^{\mathrm{a}}\boldsymbol{I}; \quad p^{\mathrm{a}} = -K^{\mathrm{a}}\left(J_{\mathrm{e}}^{\mathrm{a}} - 1\right); \quad \boldsymbol{\sigma}_{\mathrm{s}}^{\mathrm{a\,d}} = \sum_{i=1}^{N^{\mathrm{a}}} \boldsymbol{\sigma}_{\mathrm{s}\,i}^{\mathrm{a\,d}} = \sum_{i=1}^{N^{\mathrm{a}}} G_i^{\mathrm{a}} \tilde{\boldsymbol{B}}_{\mathrm{e}\,i}^{\mathrm{a\,d}}; \tag{3.11}$$

with K^{a} being the bulk modulus, G_i^{a} the shear moduli and $\tilde{\boldsymbol{B}}_{\mathrm{e}\,i}^{\mathrm{a}} = J_{\mathrm{e}\,i}^{\mathrm{a}\,-\frac{2}{3}} \boldsymbol{F}_{\mathrm{e}\,i}^{\mathrm{a}} \cdot \boldsymbol{F}_{\mathrm{e}\,i}^{\mathrm{a}\,\mathrm{T}}$ the isochoric elastic Finger tensor of mode i. The hardening stress depends on the isochoric deformation gradient:

$$\boldsymbol{\sigma}_{\mathrm{r}}^{\mathrm{a}} = G_{\mathrm{r}} \tilde{\boldsymbol{B}}^{\mathrm{a\,d}} \tag{3.12}$$

where G_{r} is a hardening modulus. Finally, the plastic deformation gradients are obtained from time-integration of the plastic part of the deformation rate, which is related to the deviatoric driving stress:

$$\boldsymbol{D}_{\mathrm{p}\,i}^{\mathrm{a}} = \frac{1}{2}\left(\boldsymbol{L}_{\mathrm{p}\,i}^{\mathrm{a}} + \boldsymbol{L}_{\mathrm{p}\,i}^{\mathrm{a}\,\mathrm{T}}\right) = \frac{\boldsymbol{\sigma}_{\mathrm{s}\,i}^{\mathrm{a\,d}}}{2\eta_i}. \tag{3.13}$$

To account for the contribution of two molecular processes, α and β, the Maxwell modes are divided into two groups corresponding to these molecular processes. The number of modes corresponding to the α process is N_α^{a} and $N_\beta^{\mathrm{a}} = N^{\mathrm{a}} - N_\alpha^{\mathrm{a}}$ is the number of modes corresponding to the β process.

The viscosities η_i in equation (3.13) are non-linear and depend on the equivalent deviatoric driving stress τ_π, temperature T, pressure p^{a}, and thermodynamic state S_π, which is related to the equivalent plastic strain γ_{p}:

$$\eta_i = \eta_{0i} \frac{\tau_\pi/\tau_{0\pi}}{\sinh\left(\tau_\pi/\tau_{0\pi}\right)} \exp\left(\frac{\mu_\pi p^{\mathrm{a}}}{\tau_{0\pi}}\right) \exp\left(S_\pi\right), \tag{3.14}$$

with $\pi = \alpha, \beta$. Here τ_0 is a characteristic stress, μ the pressure dependence parameter and η_{0i} are viscosity parameters corresponding to the rejuvenated state, which are temperature dependent in the following way:

$$\eta_{0i} = \eta_{0ir} \exp\left(\frac{\Delta U_\pi}{R}\left(\frac{1}{T} - \frac{1}{T_{\mathrm{r}}}\right)\right), \tag{3.15}$$

where R is the universal gas constant, ΔU_π the activation energy and T_{r} a reference temperature, which corresponds to the viscosity parameters η_{0ir} in the rejuvenated reference state. The equivalent deviatoric driving stress τ_π is defined as:

$$\tau_\pi = \sqrt{\frac{1}{2}\boldsymbol{\sigma}_{\mathrm{s}\pi}^{\mathrm{a\,d}} : \boldsymbol{\sigma}_{\mathrm{s}\pi}^{\mathrm{a\,d}}}, \tag{3.16}$$

where $\boldsymbol{\sigma}_{\mathrm{s}\pi}^{\mathrm{a\,d}}, \pi = \alpha, \beta$ is the overall deviatoric driving stress of process π, calculated as the summation of $\boldsymbol{\sigma}_{\mathrm{s}\,i}^{\mathrm{a\,d}}$ for all modes corresponding to the π process. The characteristic stress is a temperature-dependent parameter:

$$\tau_{0\pi} = \frac{kT}{V_\pi^*}, \tag{3.17}$$

where k is the Boltzmann constant and V_π^* the activation volume.

The deformed, "rejuvenated" state is chosen as a reference state, of which the strain rate dependence is fully described by the viscosity expressions in equations (3.13)–(3.15). Changes in thermodynamic state, as a result of ageing, are incorporated by introduction of the state parameter S_π, one for each process, which determines the age-dependent shift of the strain rate dependence of the yield stress towards lower strain rates and which is zero at the reference state. This implies that within such approach there is no difference between the thermodynamic state of the material during deformation at a different strain rates. This is supported by experimental observations [100], where it was shown that the softening process is independent of deformation rate and is influenced by an evolution of structure that is a result of plastic deformation.

A thermodynamic state variable S_π also describes softening after the yield point. It depends on a function $R_{\gamma\pi}$ that describes mechanical rejuvenation [42]:

$$S_\pi = S_{a\pi} R_{\gamma\pi}; \quad R_{\gamma\pi} = \frac{\left(1 + (r_{0\pi} \exp{(\gamma_p)})^{r_{1\pi}}\right)^{\frac{r_{2\pi}-1}{r_{1\pi}}}}{\left(1 + r_{0\pi}{}^{r_{1\pi}}\right)^{\frac{r_{2\pi}-1}{r_{1\pi}}}}, \tag{3.18}$$

Here $S_a, r_{0\pi}, r_{1\pi}$ and $r_{2\pi}$ are model parameters. The ageing parameter S_a is taken to be constant, although it can be time and temperature dependent (for details see [42]). The equivalent plastic strain is defined on the basis of the first mode and its time derivative as:

$$\dot{\gamma}_p = \frac{\tau_1}{\eta_1}; \quad \tau_1 = \sqrt{\frac{1}{2}\boldsymbol{\sigma}_{s\,1}^{a\;d} : \boldsymbol{\sigma}_{s\,1}^{a\;d}}, \tag{3.19}$$

where tensor $\boldsymbol{\sigma}_{s\,1}^{a\;d}$ is the deviatoric driving stress of the first mode.

In this work, a multi-process formulation is used with a single mode corresponding to each process. Since it was observed in the experiments that the pre-yield behaviour of PET is almost linear, using a single mode corresponding to each process for the description is sufficient.

3.3.4   Some aspects of numerical implementation of the EGP model

To enable the incorporation of the EGP model in the micromechanical modelling framework, a solution procedure is used in which the amorphous state of deformation $\boldsymbol{F}^a$ and Cauchy stress $\boldsymbol{\sigma}^a$ can be fully determined from imposed mixed boundary conditions. For a well-posed boundary value problem, by specifying some components of $\boldsymbol{F}^a$ and $\boldsymbol{\sigma}^a$, all other components of these tensors can be obtained. The elastic deformation gradient of the first mode, $\boldsymbol{F}_{e\,1}^a$, is a variable, for which a set of non-linear equations (linking $\boldsymbol{F}^a$ and $\boldsymbol{\sigma}^a$) are solved using the Newton-Raphson method. This tensor is used because it fully describes the state of the material, as shown in figure 3.3, and fits in the composite inclusion model framework, see [83]. Therefore, in the solution scheme of the EGP model, a Newton-Raphson method is used to find $\boldsymbol{F}_{e\,1}^a$ such that the components of $\boldsymbol{F}^a$ and $\boldsymbol{\sigma}^a$ satisfy the values imposed by boundary conditions. The numerical procedure for obtaining $\boldsymbol{F}^a$ and $\boldsymbol{\sigma}^a$ from a known $\boldsymbol{F}_{e\,1}^a$ is schematically shown in figure 3.3 and is described below.

Since $\tau_\pi, \pi = \alpha, \beta$ depends non-linearly on $\boldsymbol{F}_{e\,1}^a$, at first, τ_π is determined. The state of the plastic and elastic deformation and thereby the stress in each mode depend on the viscosity η_i, which, in turn, depends on τ_π. Therefore, using Banach fixed-point theorem, τ_π can be iteratively found, using the value from the previous time step as an initial estimate. Some details of obtaining the stresses are summarised below.

$F_{e_1}^a(t_n)$

$J_e^a(t_n)$ $\sigma_{s_1}^a(t_n)$ $\tau_\pi(t_n);\ \pi = \alpha, \beta$

integrate $\dot\gamma_p = g(\gamma_p)$

$\eta_i(t_n);\ i = \overline{1, N^a}$ $\gamma_p(t_n)$

solve equation $\tau_\pi = f(\tau_\pi)$

$\hat{L}_{p1}^a(t_n)$ $F_{p1}^a(t_{n-1})$

Padé approximation of $\exp\left(\hat{L}_{p1}^a\right)$

$\sigma_r^a(t_n)$ $F_{p1}^a(t_n)$

$F^a(t_n)$ $C_{pi}^a(t_{n-1});\ i = \overline{2, N^a}$

solve $C_{pi}^a(t_n) = M\left(t_n, C^a(t_n), C_{pi}^a(t_{n-1})\right)$

$\sigma^a(t_n)$ $C_{pi}^a(t_n);\ i = \overline{2, N^a}$

$B_{e_i}^a(t_n)$ $\sigma_{s_i}^a(t_n)$ $f(\tau_\pi(t_n))$
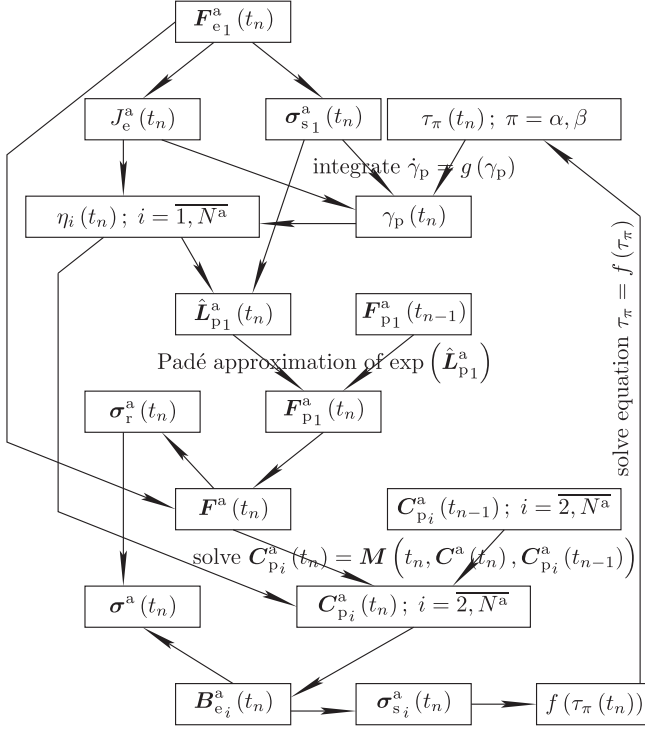
Figure 3.3: Numerical solution procedure of the EGP model.

Knowing $F_{e_1}^a$, the deviatoric driving stress of the first mode $\sigma_{s_1}^{a\ d}$ can be found. Then, integrating equation (3.19), using the implicit Euler method (and also the Newton-Raphson scheme to obtain the solution of the resulting non-linear equation), γ_p is obtained. Next, knowing the viscosity η_1, the plastic velocity gradient $\hat{L}_{p1}^a$ (in the intermediate configuration) is determined. Time integration of $\hat{L}_{p1}^a$ (using the Padé approximation of $\exp\left(\hat{L}_{p1}^a\right)$) leads to F_{p1}^a, thus to F^a. It can be shown, that for other modes ($i \neq 1$), the plastic Cauchy-Green deformation tensor C_{pi}^a takes the following form (if the implicit Euler method is used for time integration of $\dot{C}_{pi}^a$):

$$C_{pi}^a(t_n) = s\left(\frac{\Delta t G_i^a}{(J^a)^{\frac{2}{3}}\eta_i} C^a(t_n) + C_{pi}^a(t_{n-1})\right), \quad i = \overline{2, N^a}, \tag{3.20}$$

where Δt is the time step, s a normalisation constant (taken such that $\det\left(C_{pi}^a\right) = 1$) and $C_{pi}^a(t_{n-1})$ the plastic Cauchy-Green deformation tensor at the previous time step. Next, the elastic Finger tensor of the i-th mode $B_{e_i}^a$ is obtained and, after that, the deviatoric driving stress of the i-th mode $\sigma_{s_i}^{a\ d}$. From the obtained stresses, τ_π can be determined.

After obtaining τ_π, in the same iterative loop, F^a is found. Likewise, the hardening stress σ_r^a and total Cauchy stress σ^a result.

Table 3.1: Input parameters for PET.

parameter	η_{01r} [MPa·s]	G_1^a [MPa]	ΔU_α [kJ/mol]	μ_α [−]	T_r [K]	
value	10^{27}	230	700	0.024	296	
parameter	η_{02r} [MPa·s]	G_2^a [MPa]	ΔU_β [kJ/mol]	μ_β [−]	G_r [MPa]	
value	70	187	100	0.024	4.7	
parameter	V_α^* [nm³]	$S_{a\alpha}$ [−]	$r_{0\alpha}$ [−]	$r_{1\alpha}$ [−]	$r_{2\alpha}$ [−]	K^a [MPa]
value	13.0	13	0.9	5	−2	1800
parameter	V_β^* [nm³]	$S_{a\beta}$ [−]	$r_{0\beta}$ [−]	$r_{1\beta}$ [−]	$r_{2\beta}$ [−]	
value	4.3	13	0.99	50	−8	

3.4 Characterisation

3.4.1 Amorphous material

To obtain the constitutive parameters for amorphous PET, pure amorphous material is first considered. In the case of uniaxial deformation, the constitutive equations of the amorphous phase, summarised in section 3.3.3, can be simplified. Thus, a direct relation between model parameters and experimentally observed quantities, such as yield stress or stress at large stains, can be established. In appendix 3.B, the process of characterisation is summarised (more details can also be found in [46, 101]). Results are shown in table 3.1.

The true stress-strain behaviour of amorphous PET under uniaxial compression is shown in figure 3.4. The dependence of the upper yield stress, which is the maximum stress before softening, and the lower yield stress, which is the minimum stress after softening, on the strain rate is shown in figure 3.5. When large strains in PET in a glassy state are considered, two molecular processes contribute to stress, which results in a marked change of strain rate dependence during post yield. In such a multi-process approach two different contributions can be recognized, each with their own reference response, their own Eyring parameters and both being subject to physical ageing. However, in this description, the position of the reference state of the β molecular process is arbitrary, i.e. its reference viscosity and ageing parameters of both processes are chosen and are not determined uniquely. Examples of methods to determine model parameters in such cases are extensively described in [46]. As seen in figure 3.5, at 23 °C, the lower yield stress is relatively high. Since the activation of a secondary molecular process (β) is governed by temperature and strain rate [46], a deviation of lower yield stress from a linear relation at 23 °C in figure 3.5b can be considered as a contribution of the β molecular process, which allows one to fix an arbitrary choice of the reference state. Note that this choice does not influence the quality of the prediction of upper yield, since at the upper yield point the reference state viscosities are shifted due to material ageing. As other polymers, PET reveals piecewise linear yield kinetics.

At 60 °C and small strain rates, the experimentally measured yield stress is dropping. The explanation of this fact can be that the material reaches equilibrium, since this temperature is close to the glass transition temperature T_g for PET. It can be shown that when temperatures are close to T_g the yield stress dependence on annealing time reaches a plateau [102]. For a quenched sample, the yield stress increases with annealing time until, after some time, equilibrium is reached. However if well-aged material (with high yield stress at room temperature) is heated to such a temperature
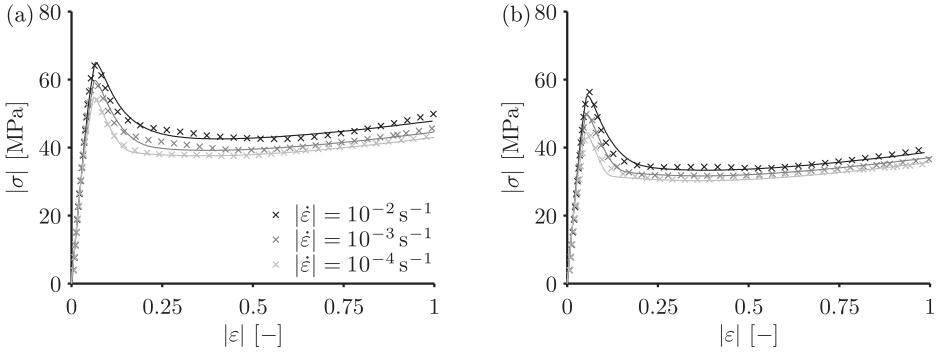
Figure 3.4: Intrinsic stress-strain response of amorphous PET under uniaxial compression, at $23\,°C$ (a) and at $40\,°C$ (b); comparison of the model (solid lines) and experimental data (symbols).
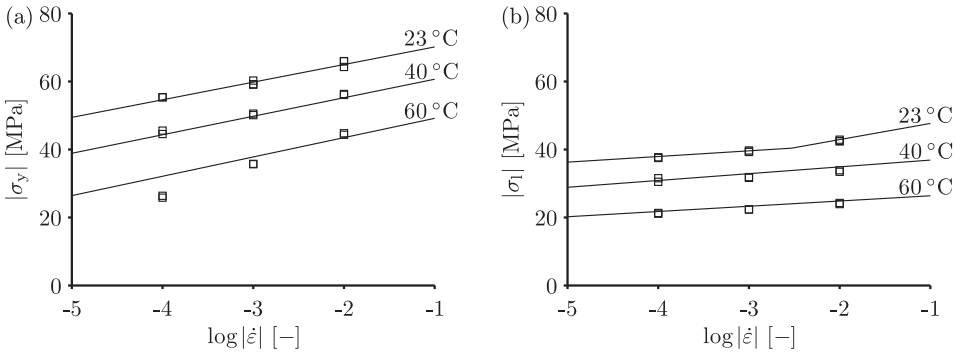
Figure 3.5: Dependence of absolute values of upper (a) and lower (b) yield stresses of PET during uniaxial compression on strain rate at $23\,°C$, $40\,°C$ and $60\,°C$; comparison of the model (solid lines) and experimental data (symbols).

the yield stress will decrease as a function of time until reaching an equilibrium state. As seen from figure 3.5a, with the increase of the test time, the deviation of the prediction from the measurements increases. This behaviour was also observed in tensile experiments on a different grade of isotropic amorphous PET, but not taken into account in the model prediction in figure 3.5.

For PET a two-process EGP model with one Maxwell mode for each process is sufficient, since the pre-yield behaviour of PET is almost linear and it is not necessary to use multiple Maxwell modes to describe the pre-yield behaviour precisely. A comparison of the model prediction with experimental data for uniaxial compression is shown in figure 3.4. As it can be observed, there is a good match between the computational and experimental results.
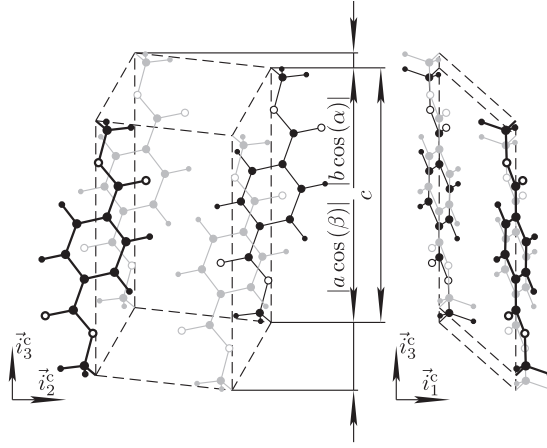
Figure 3.6: Arrangement of chains in a PET crystal, front view (left) and left view (right); carbon atoms are shown with large dots, hydrogen with small dots, and oxygen atoms with open circles, atomic positions are taken from [26].

3.4.2 Semicrystalline material

The crystal structure of PET is triclinic, see figure 3.6. Lattice parameters, determined by molecular modelling [25], are given by: $a = 0.448\,\text{nm}$, $b = 0.602\,\text{nm}$, $c = 1.086\,\text{nm}$, $\alpha = 102.5°$, $\beta = 119.8°$, $\gamma = 107.0°$ (at $T = 300\,\text{K}$). A local coordinate system is defined for the crystal unit cell, such that $\vec{i}_3^{\,c}$ corresponds to the chain direction (the (001) crystallographic direction) and $\vec{i}_2^{\,c}$ is orthogonal to $\vec{i}_3^{\,c}$ and lies in the (100) crystallographic plane; $\vec{i}_1^{\,c}$ is then obtained through the vector product: $\vec{i}_1^{\,c} = \vec{i}_2^{\,c} \times \vec{i}_3^{\,c}$. Note that if atomic positions are taken from [26], then the angle between the normal to the (100) plane and the normal to the benzene ring of the PET molecule is $21.5°$.

The stiffness matrix of the PET crystal is temperature dependent, here interpolated at a particular temperature from molecular modelling data [25]. At ambient temperature $(300\,\text{K})$ the stiffness matrix is the following:

$$\underline{C}^{\text{c}} = \begin{pmatrix} 14.4 & 6.4 & 3.4 & -2.2 & -0.3 & -1.8 \\ 6.4 & 17.3 & 9.5 & 3.3 & -0.5 & 0.5 \\ 3.4 & 9.5 & 178.0 & 3.8 & -0.7 & -1.8 \\ -2.2 & 3.3 & 3.8 & 6.6 & 0.2 & -0.4 \\ -0.3 & -0.5 & -0.7 & 0.2 & 1.4 & 0 \\ -1.8 & 0.5 & -1.8 & -0.4 & 0 & 1.2 \end{pmatrix} \text{GPa}, \qquad (3.21)$$

where the Voigt notation $(11,\ 22,\ 33,\ 23,\ 31,\ 12)$ is used.

The orientation of the lamellar surface, the crystalline-amorphous interface, is specified relative to the crystallographic unit cell. The $[101]$ crystallographic direction is considered to be normal to the lamellar surface [10, 26, 89]. For the above mentioned lattice parameters, the angle between the molecular chain axis and the lamellar normal is $\varphi \approx 25°$.

The PET crystal has three independent slip systems: $(100)[001]$ and $(010)[001]$ chain slip and $(100)[010]$ transverse slip [34]. As outlined above, in the composite inclusion model, the crystalline

phase is described as elasto-viscoplastic with an Eyring flow rule for the constitutive behaviour of the slip systems. In the case of HDPE, which has eight physically distinct slip systems, it was shown that the composite inclusion model can predict a similar macroscopic stress-strain dependence for different sets of slip systems parameters, i.e. these parameters could not be determined uniquely from an experiment with isotropic material [81]. Since the PET crystal has only three slip systems, the influence of the constitutive behaviour of each slip system on the macroscopic response is higher. However, it is still not possible to uniquely identify the behaviour of each individual slip system based on the response of isotropic material. Furthermore, two of the slip systems will be predominantly active at large deformations, where a comparison with experimental data is not possible (see figure 3.9 and discussion afterwards). Therefore, similar to [81], certain assumptions are made to reduce the number of unknown parameters.

The first assumption is that the reference shear rates for slip systems are taken such that the sequence of activation of the slip systems corresponds to the one observed experimentally in [34], i.e. $(100)[001]$ chain slip is the most easily activated slip system during compression, then $(100)[010]$ transverse slip, followed by $(010)[001]$ chain slip.

The second assumption is that the shear strength, τ_0^α (defining the slope of the slip kinetics), is the same for all slip systems. The value for τ_0^α is selected such that the characteristic stress of the Eyring flow rule of the crystalline phase and the amorphous phase are proportional, i.e. $\tau_0^\alpha = \chi\left(\tau_{0\alpha} + \tau_{0\beta}\right)$ at $T = 23\,^\circ\mathrm{C}$, where the coefficient $\chi = 0.866$ is introduced because of the different definitions of shear stress on the slip plane in the crystalline phase and equivalent stress in the amorphous phase. In [76], the behaviour of idealised 100% crystalline PET was modelled, with a power law constitutive relation between the shear rate and shear stress on the slip system. In the present work, the value for the parameter of the Eyring model, τ_0^α, is taken such that the slope τ^α versus $\log\left(\dot{\gamma}^\alpha\right)$ is close to the slope of the power law used in [76].

The constitutive behaviour of the slip systems in comparison to the constitutive behaviour of the amorphous phase is shown in figure 3.7. For the comparison, the viscosity used is taken at $S_\pi = 0$. For this purpose, the equivalent plastic deformation of separate processes in the amorphous phase needs to be defined, i.e. the equivalent plastic deformation of the α process is $\dot{\gamma}_{p\alpha} = \dot{\gamma}_p$ and the equivalent plastic deformation of β process is the following:

$$\dot{\gamma}_{p\beta} = \frac{\tau_2}{\eta_2}; \quad \tau_2 = \sqrt{\frac{1}{2}\boldsymbol{\sigma}_{\mathrm{s}\,2}^{\mathrm{a}\,\mathrm{d}} : \boldsymbol{\sigma}_{\mathrm{s}\,2}^{\mathrm{a}\,\mathrm{d}}}. \tag{3.22}$$

Equivalent shear stress τ^α of the slip systems of the crystalline phase is compared to the effective equivalent deviatoric driving stress of the amorphous phase $\tau_1 + \tau_2$ (i.e. when both molecular processes are active).

Using the composite inclusion model for simulating the behaviour of an isotropic material, random orientations of the crystalline phase have to be generated. A number of inclusions of $N^{\mathrm{I}} = 125$ was found to be sufficient to describe the macroscopic behaviour in case of isotropic material. The parameters ξ^α were identified such that the stress-strain curves demonstrate the best match with the experimentally measured results. The results of the characterisation are shown in table 3.2. The predicted effect of crystallinity on the macroscopic behaviour of rejuvenated material is illustrated in figure 3.8. In figure 3.8, it is observed that the elastic modulus is increasing with crystallinity, as well as the hardening modulus. The increase of the hardening modulus was not observed in the experiment, as shown further on.

A comparison of the experimentally measured stress-strain relations with computational results is shown in figure 3.9 for crystallinities of 5% and 30% and temperatures of $23\,^\circ\mathrm{C}$ and $60\,^\circ\mathrm{C}$. The
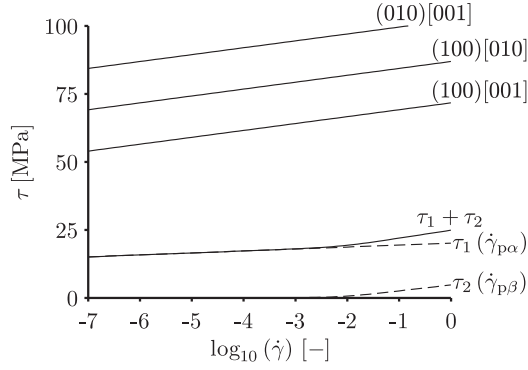
Figure 3.7: Constitutive behaviour of the slip systems of the crystalline phase in comparison to the yield kinetics of the amorphous phase (α process, β process and both processes).

Table 3.2: Parameters of the constitutive behaviour of the crystalline phase.

slip system	$(100)[001]$		$(010)[001]$		$(100)[010]$	
parameter	$\xi^1\,[\mathrm{s}^{-1}]$	$\tau_0^1\,[\mathrm{MPa}]$	$\xi^2\,[\mathrm{s}^{-1}]$	$\tau_0^2\,[\mathrm{MPa}]$	$\xi^3\,[\mathrm{s}^{-1}]$	$\tau_0^3\,[\mathrm{MPa}]$
value	10^{-28}	1.1	10^{-40}	1.1	10^{-34}	1.1
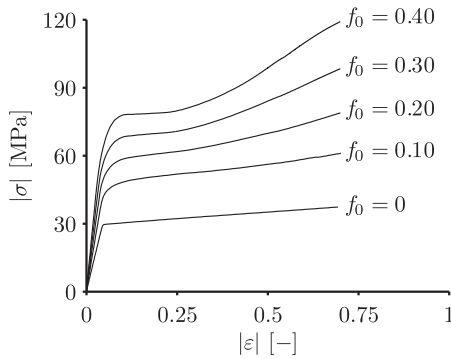
Figure 3.8: Intrinsic stress-strain dependence of rejuvenated PET prediction by the model under uniaxial compression with strain rate $|\dot{\varepsilon}| = 10^{-3}$ at $23\,°\mathrm{C}$ for different crystallinities f_0.

following conclusions can be made from a variation of the slip system parameters as given in table 3.2 (the results discussed are not shown in figures):

- Due to anisotropy of the crystal and orientation of the crystal unit cell relative to the interface between the phases, the $(100)[001]$ slip system is the dominant slip system. The average plastic deformation of this slip system is the largest of all 3 systems even when the kinetics of all slip systems are identical. Parameter ξ^1 has significant influence on the stress level at high strains.

- Parameters ξ^2 and ξ^3 have some influence on the shape of the stress-strain curve at the yield point. Increasing these parameters leads to a "sharper" yield point. However, these parameters have only a small influence on the macroscopic hardening regime due to limited slips on the $(010)[001]$ and $(100)[010]$ slip systems. Neither of the parameters has influence on the hardening slope. In an experimental study [34], activity of the $(010)[001]$ slip system was not observed, which indicates that it should have the highest resistance.

- To check if the orientation of crystals relative to the interface has an influence on the hardening modulus, the angle φ between the lamellar normal and the chain direction was varied from $0°$ (the chain direction is aligned with the lamellar normal) to $50°$ (the lamellar normal is the $[201]$ crystallographic direction) with the lamellar normal remaining of the $[u0w]$ type. Increasing φ slightly decreases the stress level in the hardening region. For values of $\varphi \geq 15°$ the hardening modulus stays almost constant, however, for values of $\varphi < 15°$ it decreases and these values also lead to a non-smooth stress-strain curve due to a sudden increase of the rate of plastic deformation for certain inclusions at certain times, also leading to higher calculation times. A smoother curve can be obtained by increasing the number of inclusions.

The reason for a significant difference between the predicted and measured elastic modulus is an inaccurate measurement technique at lower strains during compression due to the special procedure of the test. The purpose of the test lies in the large-strain response for which the experimental method is adequate. The difference at large strains between the model and experiments is attributed to other deformation mechanisms not taken into account here. In an experimental study, where semicrystalline PET was subjected to compression at $190\,°\mathrm{C}$ [34], a new long period was observed at compression ratios around 2.6, $|\varepsilon| \approx 1$, i.e. break-up of the crystalline lamellae. At lower temperatures, especially below the glass transition temperature, crystals are most likely to be destroyed at even lower strains due to a stiffer amorphous phase. The model does not take into account breakup of the crystals and therefore shows a stronger behaviour at large strains. The simulations done at $60\,°\mathrm{C}$ and small crystallinity show a larger region where the model is close to experiments, see figure 3.9.

The average absolute plastic shear rates for different slip systems of the crystalline phase of all inclusions and the average equivalent plastic strain rate of the amorphous phase are used to evaluate the plastic deformations on the slip systems and in the amorphous domains:

$$\langle \dot{\gamma}^\alpha \rangle = \frac{1}{N^{\mathrm{I}}} \sum_{k=1}^{N^{\mathrm{I}}} \left| \dot{\gamma}^{\alpha k} \right|; \quad \langle \dot{\gamma}^{\mathrm{a}} \rangle = \frac{1}{N^{\mathrm{I}}} \sum_{k=1}^{N^{\mathrm{I}}} \dot{\gamma}_{\mathrm{p}}^k. \tag{3.23}$$

Here, the superscript "k" indicates that quantities describe the phases of the kth inclusion. These quantities, normalised by the applied macroscopic strain rate, are illustrated in figure 3.10, for which
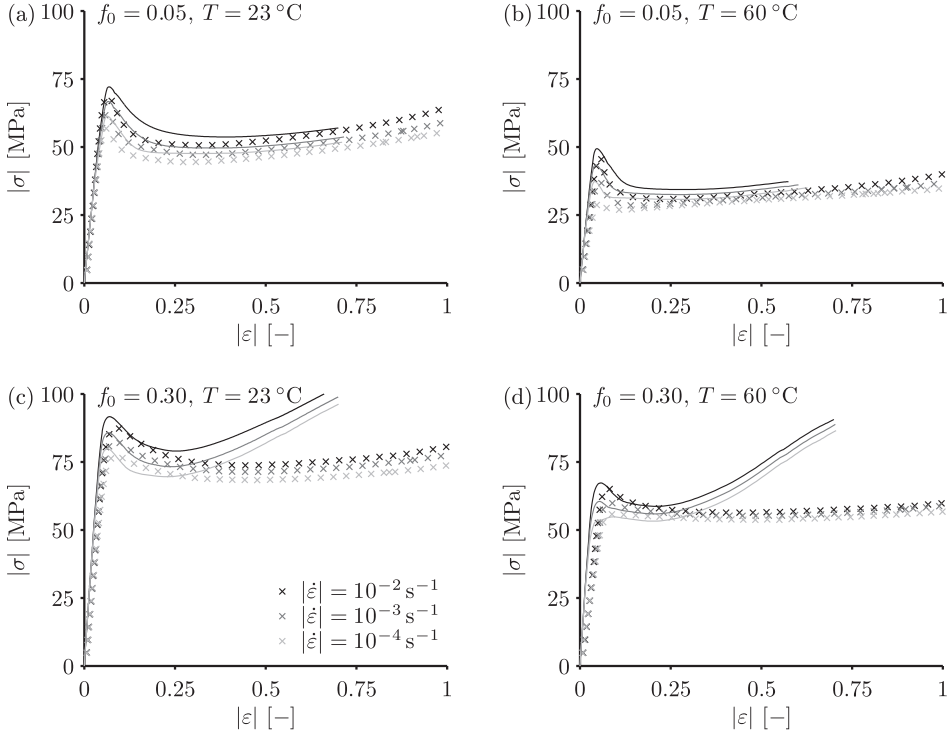
Figure 3.9: Intrinsic stress-strain response of semicrystalline PET with crystallinity $f_0 = 0.05$ (a,b) and $f_0 = 0.30$ (c,d) under uniaxial compression, at $23\,°C$ (a,c), $60\,°C$ (b,d); comparison of the model (solid lines) and experimental data (markers).

data corresponding to $|\dot{\varepsilon}| = 10^{-3}\,\mathrm{s}^{-1}$ was used. There is no significant difference between the normalised plastic deformation rates at different applied strain rates. In figure 3.10, it is observed that with increasing crystallinity, the plastic deformation rate of the amorphous phase is increasing, as well as the slip rate on system $(100)[001]$, whereas shear rates on other slip systems are decreasing. The short sudden increase of the average shear rate of the $(010)[001]$ chain slip system is due to the behaviour of one specific inclusion with a particular orientation, for which there is a temporarily large plastic deformation rate.

Texture evolution during uniaxial compression, which is illustrated in figure 3.11, corresponds to the experimentally observed texture evolution in [34]. Crystals become oriented such that (100) crystallographic planes are aligned in the plane, normal to the loading direction. The spatial distribution of inclusions (or crystalline layers) is further quantified with cumulative distribution functions $F_N\,(\theta_\zeta)$, $\zeta = \mathrm{r, c, n}$ of different angles: the angle θ_r between the global $\vec{e}_1$ direction (loading direction) and the normal to the (100) crystallographic plane, which $\theta_\mathrm{r} \leq \pi/2$; the angle θ_c between the global $\vec{e}_1$ direction and the $[001]$ crystallographic direction, which is the molecular chain direction, which $\theta_\mathrm{c} \leq \pi/2$; and the angle θ_n between the global $\vec{e}_1$ direction and the direction normal to the inclusion interface (which $\theta_\mathrm{n} \leq \pi/2$). An example of such distribution functions at different time steps is illustrated in figure 3.12, where it is seen that at $|\dot{\varepsilon}t| = 0.7$ the angles θ_r are
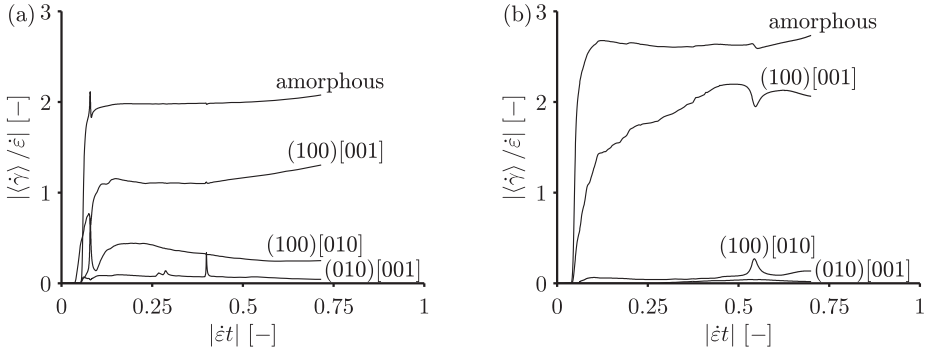
Figure 3.10: Evolution of average plastic deformation with time predicted by the model for the amorphous phase and the 3 slip systems for 5% (a) and 30% (b) crystallinity in case of uniaxial compression.
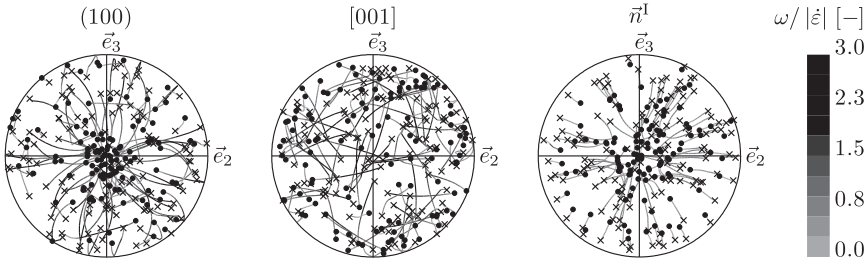

Figure 3.11: Equal area projection pole figures showing various crystallographic orientations (normal to (100) plane and $[001]$ direction) and the normal to the inclusion interface $(\vec{n}^{\mathrm{I}})$ with their trajectories during loading. Initial positions are shown with symbols $\times$, final positions $(|\dot{\varepsilon}t| = 0.7)$ with symbols $\bullet$. Colours indicate the angular velocity normalised by $|\dot{\varepsilon}|$. Here, crystallinity is $f_0 = 0.30$, strain rate $|\dot{\varepsilon}| = 10^{-3}\,\mathrm{s}^{-1}$, temperature $T = 23\,^{\circ}\mathrm{C}$ and loading direction is $\vec{e}_1$.

decreasing, i.e. normals to (100) planes are aligning towards the loading direction. The horizontal axis uses $1 - \cos{(\theta_{\mathrm{r}})}$ because it is uniformly distributed in cases where orientations correspond to isotropic material (i.e. when $t = 0\,\mathrm{s}$). A similar behaviour is observed for the angle θ_{n}, i.e. lamellar normals are also aligning with loading directions. However, the $[001]$ direction is mostly drifting around the loading direction and slightly away from it.

Evolution of the distribution functions with time is characterised with the Kolmogorov-Smirnov statistic:

$$D_N\left(\theta_{\zeta}\left(t\right)\right) = \sup_{\theta_{\zeta}} \left|F_N\left(\theta_{\zeta}\left(t\right)\right) - F_N\left(\theta_{\zeta}\left(t_0\right)\right)\right|, \quad \zeta = \mathrm{r}, \mathrm{c}, \mathrm{n}. \tag{3.24}$$

An example of D_N for θ_{n} is shown in figure 3.13a, where only a small variation of this function is observed when loading conditions are changed. The same is observed for θ_{r} and θ_{c}. A small
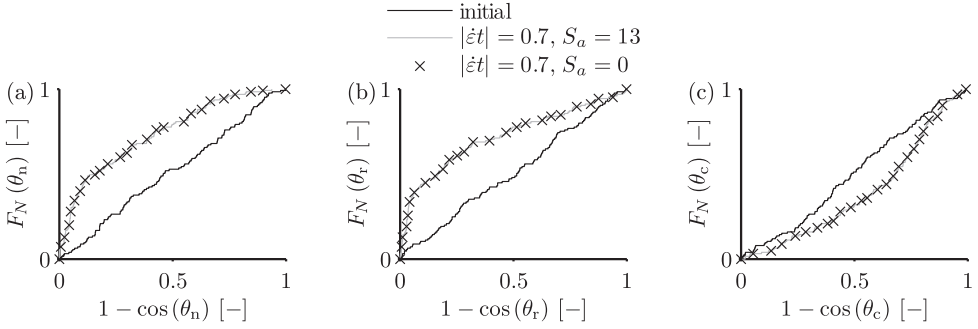
Figure 3.12: Dependence of cumulative distribution functions $F_N(\theta_n)$ on $1 - \cos(\theta_n)$, where θ_n is the angle between loading direction and the normal to the inclusion interface (a); $F_N(\theta_r)$ vs. $1 - \cos(\theta_r)$, where θ_r is the angle between loading direction and the normal to the (100) crystallographic plane (b); $F_N(\theta_c)$ vs. $1 - \cos(\theta_c)$, where θ_c is the angle between loading direction and the chain direction (c). Here crystallinity $f_0 = 0.30$, strain rate $|\dot{\varepsilon}| = 10^{-3}\,\mathrm{s}^{-1}$ and temperature $T = 23\,°\mathrm{C}$. Two different ageing parameters S_a are used, with data corresponding to rejuvenated state ($S_a = 0$) shown in symbols, part of which was omitted for clarity.

deviation of D_N is observed when crystallinity is changed. Therefore, it can be concluded that texture evolution is negligibly influenced by strain rate or temperature when these parameters are changed in the analysed regime, and are only little affected when crystallinity is changed from 5% to 30%. Statistical measures for different angles are compared in figure 3.13b, where a significant change of $D_N(\theta_r)$ (evolution of distribution function for the angle between loading direction and the (100) crystallographic plane) and $D_N(\theta_n)$ (evolution of distribution function for the angle between loading direction and the inclusion interface) with time is observed.

The influence of the ageing parameter S_a on texture evolution was also investigated. Values of $S_a = 13$ and $S_a = 0$ result in two types of curves: with a high yield stress followed by softening, such as in figure 3.9, or a stress-strain curve corresponding to mechanically rejuvenated material, such as in figure 3.8. Almost no influence of material ageing on texture evolution (i.e. the distribution functions of θ_r, θ_c and θ_n) was observed, as shown in figures 3.12 and 3.13a.

3.5 Application to creep

The micromechanical model with parameters as determined above for uniaxial compression conditions was next applied to describe the creep behaviour of PET film and model predictions were compared with experimental results. The behaviour of amorphous PET was simulated with the EGP model with the parameters listed in table 3.1, with the exception of the shear moduli (since G_k^a depend on the PET grade; moreover it cannot be measured exactly in compression), and ageing parameters (since samples prepared for compression and tension can have a different thermodynamic
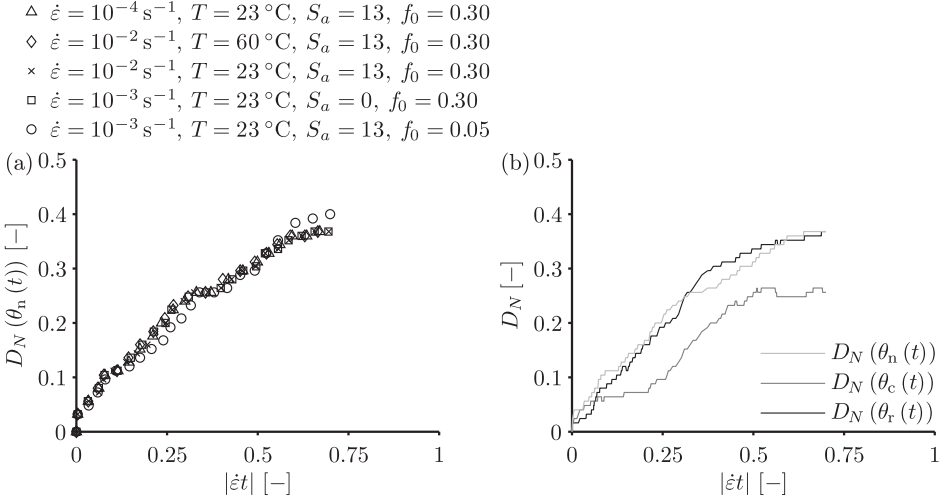
△ $\dot{\varepsilon} = 10^{-4}\,\mathrm{s}^{-1}$, $T = 23\,°\mathrm{C}$, $S_a = 13$, $f_0 = 0.30$
◇ $\dot{\varepsilon} = 10^{-2}\,\mathrm{s}^{-1}$, $T = 60\,°\mathrm{C}$, $S_a = 13$, $f_0 = 0.30$
× $\dot{\varepsilon} = 10^{-2}\,\mathrm{s}^{-1}$, $T = 23\,°\mathrm{C}$, $S_a = 13$, $f_0 = 0.30$
□ $\dot{\varepsilon} = 10^{-3}\,\mathrm{s}^{-1}$, $T = 23\,°\mathrm{C}$, $S_a = 0$, $f_0 = 0.30$
○ $\dot{\varepsilon} = 10^{-3}\,\mathrm{s}^{-1}$, $T = 23\,°\mathrm{C}$, $S_a = 13$, $f_0 = 0.05$

Figure 3.13: Dependence of Kolmogorov-Smirnov statistic (a) on time for θ_n for different loading conditions and material parameters; comparison of Kolmogorov-Smirnov statistics (b) for θ_r (angle between loading direction and the (100) crystallographic plane), θ_c (angle between loading direction and the chain direction) and θ_n (angle between loading direction and the inclusion interface) in case of strain rate $|\dot{\varepsilon}| = 10^{-3}\,\mathrm{s}^{-1}$, temperature $T = 23\,°\mathrm{C}$ and a crystallinity of $f_0 = 0.30$.

age). Here, these parameters were fitted to the experiment and are the following:

$$G_1^\mathrm{a} = 448\,\mathrm{MPa}, \quad G_2^\mathrm{a} = 365\,\mathrm{MPa}, \quad S_{a\alpha} = S_{a\beta} = 12.7. \tag{3.25}$$

To describe the behaviour of the semicrystalline PET, the composite inclusion model was used. Parameters for the constitutive behaviour of the amorphous phase in the semicrystalline material are identical to those used for the creep simulation of the fully amorphous PET. Crystallinities were estimated from X-ray measurements of the crystallinity of the annealed samples, i.e. 13% and 25%, which correspond to 6 and 13 hours of annealing, respectively. The applied stress and temperature correspond to the experimental conditions $\sigma_\mathrm{c} = 5\,\mathrm{MPa}$, $T = 30\,°\mathrm{C}$. Results are shown in figure 3.14a, where a good match of experimentally measured and simulated creep compliances for amorphous PET is observed. Also, the model predicts reasonably well the compliance modulus at high crystallinity, and its evolution with time. However, there is an offset error for 13% crystallinity.

    Since the deformations remain small, almost no texture evolution is predicted by the model in the case of creep boundary conditions. Kolmogorov-Smirnov statistics for distribution functions for the angles between loading direction and the normal to the (100) plane (θ_r), the chain direction (θ_c) and the inclusion normal (θ_n) at the final time step t_f are small:

$$D_N\left(\theta_\zeta\left(t_\mathrm{f}\right)\right) \leq 0.024; \quad \zeta = \mathrm{r}, \mathrm{c}, \mathrm{n}; \quad t_\mathrm{f} = 60000\,\mathrm{s}. \tag{3.26}$$

This implies that the distribution of the inclusion orientations is almost constant within the time frame of the simulations or experiments. However, plastic deformation is developing in both phases
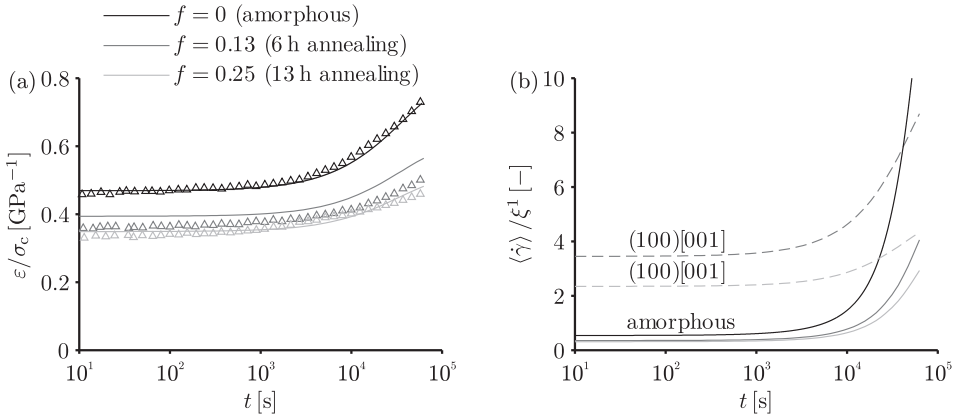
Figure 3.14: Dependence of creep compliance of PET on time for different crystallinities with 5 MPa load (a). Comparison of the model with the measurements. Evolution of plastic deformation for the amorphous PET with time and average plastic deformation of the amorphous phase and $(100)[001]$ slip system with time for the semicrystalline PET (b) in case of creep boundary conditions, model prediction.

in case of semicrystalline material. In figure 3.14b, the evolution of plastic deformation is shown, where $\dot{\gamma}$ is normalised by parameter ξ^1, which is the reference shear rate of the $(100)[001]$ slip system. It is observed that with increasing crystallinity, the average equivalent plastic strain rate of the amorphous phase and the crystalline slip rates are both decreasing. Note that only one slip system is active, since the average absolute plastic shear rates of the other slip systems are 12 and 6 orders of magnitude smaller than the parameters ξ^2 and ξ^3 of table 3.2. Focusing on the long-term response, the absolute values of plastic deformation rates are small in comparison to a short-term response.

3.6 Conclusions

In this work, the viscoplastic behaviour of semicrystalline polyethylene terephthalate was modelled using the composite inclusion model, and necessary parameters were obtained. The mechanical behaviour of amorphous PET was modelled with the multi-process EGP model, which shows an adequate agreement with the experiments at different temperatures, also predicting the complex yield kinetics. The EGP model was implemented in the framework of the composite inclusion model, where it was used for the constitutive behaviour of the amorphous phase. Some details of the numerical implementation of the EGP model were provided. For the crystalline phase, crystal viscoplasticity was used. With the composite inclusion model, the behaviour of PET under uniaxial compression was simulated, and the influence of loading conditions has been investigated. At high crystallinities and at large strains, there is a still significant mismatch between the model and the experiment, probably due to effects of crystal destruction, which are not included in the model, but were observed during X-ray measurements at much higher temperature and higher strains [34].

Below $T_{\rm g}$ break-up most probably happens at much lower strains due to the harder amorphous phase. Texture evolution obtained with the model shows a good correspondence with experiments, in spite of the omitted effect of break-up of the crystals at high strains. No influence of ageing on texture evolution is predicted by the model.

To validate the model parameters used in the description of viscoplastic behaviour, the creep compliance of PET film has been simulated. The EGP model, with shear moduli identified for the particular PET grade, showed an adequate agreement with the experiment. The composite inclusion model demonstrated a good match with the measured data at high crystallinity as well, but at lower crystallinity, it seems to underestimate the elastic modulus. This might also be due to inaccurate crystallinity measurements in the experiment.

The model can now be further applied to oriented films, to predict creep behaviour of oriented PET used in, e.g., the manufacturing of flexible electronics.

3.A   Appendix: composite inclusion model

In this section, the equations representing the composite inclusion model are summarised. In addition to notations used in the chapter, a superscript "k" is introduced to indicate that a tensor or scalar describes an inclusion with number k. The constitutive equations for each phase of the $N^{\rm I}$ inclusions specify the stress depending on the deformation gradient in the following way:

$$\boldsymbol{\sigma}^{\nu k}\left(t\right) = \boldsymbol{\sigma}^{\nu k}\left(\boldsymbol{F}^{\nu k}, t^*|0 \leq t^* \leq t\right); \quad k = \overline{1, N^{\rm I}}; \quad \nu = {\rm a, c}. \tag{A1}$$

The material is modelled as a collection of layered domains, referred to as inclusions, see figure 5.4. Inclusion averaged quantities are obtained as:

$$\boldsymbol{F}^{{\rm I}k} = \left(1 - f_0\right)\boldsymbol{F}^{{\rm a}k} + f_0\boldsymbol{F}^{{\rm c}k}, \tag{A2}$$

$$\boldsymbol{\sigma}^{{\rm I}k} = \left(1 - f^k\right)\boldsymbol{\sigma}^{{\rm a}k} + f^k\boldsymbol{\sigma}^{{\rm c}k}, \tag{A3}$$

where the volume fraction of the crystalline phase, with f_0 the initial value, is given by:

$$f^k = \frac{f_0 J^{{\rm c}k}}{\left(1 - f_0\right)J^{{\rm a}k} + f_0 J^{{\rm c}k}}, \tag{A4}$$

with $J^{\nu k} = \det\left(\boldsymbol{F}^{\nu k}\right), \nu = {\rm a, c}$. The orientation of the interface is given by two vectors $\vec{e}_1^{\,{\rm I}k}$ and $\vec{e}_2^{\,{\rm I}k}$ lying in the interface and its normal vector $\vec{e}_3^{\,{\rm I}k} = \vec{n}^{{\rm I}k}$. A subscript "0" indicates that quantities are taken in the initial configuration rather than in the current configuration.

In the inclusion, two layers are considered to be perfectly mechanically attached to each other. Therefore, equilibrium and compatibility conditions within each inclusion are enforced:

$$\boldsymbol{\sigma}^{{\rm c}k} \cdot \vec{e}_3^{\,{\rm I}k} = \boldsymbol{\sigma}^{{\rm a}k} \cdot \vec{e}_3^{\,{\rm I}k}; \quad k = \overline{1, N^{\rm I}}; \tag{A5}$$

$$\boldsymbol{F}^{{\rm c}k} \cdot \vec{e}_{n0}^{\,{\rm I}k} = \boldsymbol{F}^{{\rm a}k} \cdot \vec{e}_{n0}^{\,{\rm I}k}; \quad k = \overline{1, N^{\rm I}}; \quad n = \{1, 2\}. \tag{A6}$$

Various interaction laws between the inclusions can be defined. In this study, the $\hat{\boldsymbol{U}}$ interaction law [83] is used, for which an auxiliary deformation-like symmetric tensor $\hat{\boldsymbol{U}}$ is introduced as an unknown. A subscript "M" indicates that quantities belong to the macroscopic scale. The following

interinclusion interaction laws are imposed:

$$\vec{e}_m^{\mathrm{I}k} \cdot \boldsymbol{\sigma}^{\mathrm{I}k} \cdot \vec{e}_n^{\mathrm{I}k} = \vec{e}_m^{\mathrm{I}k} \cdot \boldsymbol{\sigma}^{\mathrm{M}} \cdot \vec{e}_n^{\mathrm{I}k}; \quad k = \overline{1, N^{\mathrm{I}}}; \quad m, n = \{1, 2\}; \tag{A7}$$

$$\boldsymbol{U}^{\mathrm{I}k} \cdot \vec{e}_{30}^{\mathrm{I}k} = \hat{\boldsymbol{U}} \cdot \vec{e}_{30}^{\mathrm{I}k}; \quad k = \overline{1, N^{\mathrm{I}}}; \tag{A8}$$

$$\boldsymbol{R}^{\mathrm{I}k} = \boldsymbol{R}^{\mathrm{M}}; \quad k = \overline{1, N^{\mathrm{I}}}, \tag{A9}$$

where the macroscopic Cauchy stress is determined by volume averaging:

$$\boldsymbol{\sigma}^{\mathrm{M}} = \sum_{k=1}^{N^{\mathrm{I}}} f^{\mathrm{I}k} \boldsymbol{\sigma}^{\mathrm{I}k}, \tag{A10}$$

and where $f^{\mathrm{I}k} = f_0^{\mathrm{I}k} J^{\mathrm{I}k} / J^{\mathrm{M}}$ is the volume fraction of the inclusion, $J^{\mathrm{M}} = \sum_{k=1}^{N^{\mathrm{I}}} f_0^{\mathrm{I}k} J^{\mathrm{I}k}$ is the macroscopic volume ratio, $f_0^{\mathrm{I}k} = 1/N^{\mathrm{I}}$ is the initial volume fraction of the inclusion and $J^{\mathrm{I}k} = \det\left(\boldsymbol{F}^{\mathrm{I}k}\right)$ is the volume change ratio of the inclusion. Volume averaging is also used to find the macroscopic right stretch tensor:

$$\left(\frac{J^{\mathrm{M}}}{J_{\Sigma}}\right)^{\frac{1}{3}} \boldsymbol{U}^{\mathrm{M}} = \sum_{k=1}^{N^{\mathrm{I}}} f_0^{\mathrm{I}k} \boldsymbol{U}^{\mathrm{I}k}; \tag{A11}$$

where $J_{\Sigma} = \det\left(\sum_{k=1}^{N^{\mathrm{I}}} f_0^{\mathrm{I}k} \boldsymbol{F}^{\mathrm{I}k}\right)$.

3.B Appendix: identification of model parameters

Using the assumptions made (at the yield point $\dot{\gamma}_{\mathrm{p}} = \sqrt{3}\,|\dot{\varepsilon}_{\mathrm{p}}| \approx \sqrt{3}\,|\dot{\varepsilon}|$, therefore $R_{\gamma\pi} \approx 1$; $J_{\mathrm{e}} \approx 1$, no volume change; $\sinh(x) \approx 0.5\exp(x)$), the stress after the yield point, when the major deformation mechanism is plastic deformation, can be calculated using the following relation (in the case that both molecular processes give a contribution to the stress):

$$|\sigma| = \frac{1}{\sqrt{3} + \mathrm{sign}\,(\dot{\varepsilon})\,(\mu_\alpha + \mu_\beta)} \left(3\tau_{0\alpha} \ln\left(\frac{2\sqrt{3}\eta_{01}\,|\dot{\varepsilon}|\,|\lambda_{\mathrm{e}1}|}{\tau_{0\alpha}} \exp\left(S_{\mathrm{a}\alpha} R_{\gamma\alpha}\right)\right) + \right.$$

$$\left. + 3p_0\,(\mu_\alpha + \mu_\beta) + 3\tau_{0\beta} \ln\left(\frac{2\sqrt{3}\eta_{02}\,|\dot{\varepsilon}|\,|\lambda_{\mathrm{e}2}|}{\tau_{0\beta}} \exp(S_{\mathrm{a}\beta} R_{\gamma\beta})\right) + \sqrt{3}\left|\lambda^2 - \frac{1}{\lambda}\right| G_{\mathrm{r}}\right), \tag{B1}$$

where λ is the stretch ratio, $\lambda_{\mathrm{e}i}, i = 1, 2$ the elastic stretch ratios of mode i according to equation (3.8), $\dot{\varepsilon}$ is the time derivative of the true strain $\varepsilon = \ln(\lambda)$, $R_{\gamma\pi}, \pi = \alpha, \beta$ are functions describing the thermodynamic state, which at the yield point ($\lambda = \lambda_{\mathrm{y}}$) are approximately 1, and p_0 is the superimposed hydrostatic pressure. The following steps are taken to identify the EGP model parameters:

1. The first step is to determine the bulk modulus, K^{a}, which for PET is taken from [103].

2. Next, the pressure dependence parameters μ_π, $\pi = \alpha, \beta$ are determined from a series of compression or tensile tests under superimposed hydrostatic pressure. In case of PET, experimental data is taken from [103]. From tensile tests with the same strain rate and varying pressure, parameters μ_α and μ_β are determined. From equation (B1), the slope of the true yield stress ($\sigma = \sigma_y$) vs. hydrostatic pressure is

$$\left| \frac{\partial \sigma_y}{\partial p_0} \right| = 3 \frac{\mu_\alpha + \mu_\beta}{\sqrt{3} + \mu_\alpha + \mu_\beta}. \tag{B2}$$

Also, here the assumption is made that both molecular processes contribute equally to the pressure dependence, i.e. $\mu_\alpha = \mu_\beta$.

3. After that, $\tau_{0\pi}$, $\pi = \alpha, \beta$ are determined from compression experiments at different strain rates (they may also be determined in tension). In figure 3.4, at the (upper) yield point, a contribution of both molecular processes is observed. At the lower yield point, which is defined as the minimum stress after softening, for small strain rates and $T = 23\,^\circ\text{C}$, or for high temperatures ($T = 40, 60\,^\circ\text{C}$) only the α process is active. For the lower yield stress, a formula similar to equation (B1) is used, without the contribution of the β process and with $R_{\gamma\alpha} = 0$. Therefore, to determine $\tau_{0\alpha} + \tau_{0\beta}$, the dependence of the upper yield stress on strain rate is considered, i.e. the slope of the true yield stress vs. the logarithm of strain rate is

$$\left| \frac{\partial \sigma_y}{\partial \log |\dot{\varepsilon}|} \right| = 3 \frac{\tau_{0\alpha} + \tau_{0\beta}}{\sqrt{3} - \mu_\alpha - \mu_\beta} \ln(10). \tag{B3}$$

To determine $\tau_{0\alpha}$, the lower yield stress vs. strain rate dependence is considered, i.e.:

$$\left| \frac{\partial \sigma_1}{\partial \log |\dot{\varepsilon}|} \right| = 3 \frac{\tau_{0\alpha}}{\sqrt{3} - \mu_\alpha} \ln(10). \tag{B4}$$

Assuming a reference temperature, the activation volumes V_π^* are determined, see equation (3.17).

4. The next step is the determination of the hardening modulus G_r from the slope of the true stress vs. strain measure $\left| \lambda^2 - \frac{1}{\lambda} \right|$ at large strains. It should be mentioned that, in general, the hardening modulus is strain rate dependent. However, this is not taken into account in the model since this effect is small. The average G_r of all strain rates is taken.

5. After that, the viscosity parameters corresponding to the rejuvenated state, η_{0i}, $i = 1, 2$, are determined. If the stress-strain response corresponding to small strain rates and one particular temperature (in this case $T = 23\,^\circ\text{C}$) is considered, at large strains only the α process is active. At very large strains, $\lambda \approx 1$, friction during compression distorts the data, and therefore parameters are obtained from the data at lower strains, $\lambda \approx 0.7$. Parameter η_{01} is calculated using equation (B1) with all terms corresponding to the β process removed and the elastic stretch ratio equal to the stretch ratio at yield, $\lambda_{e_1} \approx \lambda_y$. After that, the same is repeated for data corresponding to a large strain rate and low temperature (in this case $\dot{\varepsilon} = 10^{-2}\,\text{s}^{-1}$, $T = 23\,^\circ\text{C}$), when both molecular processes contribute to the stress level. In this case, parameter η_{02} is calculated directly using equation (B1); again the assumption $\lambda_{e_2} \approx \lambda_y$ is used. By using a reference temperature $T_r = 23\,^\circ\text{C}$, the viscosity parameters for the rejuvenated reference state $\eta_{0ir} = \eta_{0i}$, $i = 1, 2$ are obtained.

6. The ageing parameters $S_{a\pi}, \pi = \alpha, \beta$ can then be calculated from data at T_r. Since no tests were performed at temperatures lower than $T = 23\,°C$, at the yield point both processes contribute and the contribution of the α process cannot be separated. Thus, following [99], the assumption is made that $S_{a\alpha} = S_{a\beta}$. After that, the exact value is calculated using equation (B1) at yield, $\sigma = \sigma_y, \lambda = \lambda_y$.

7. Activation energies $\Delta U_\pi, \pi = \alpha, \beta$ are determined using equation (3.15). To obtain ΔU_α, the viscosity parameter corresponding to the rejuvenated state η_{01} at a temperature different from T_r, $T = 40\,°C$, is found using a similar procedure as in step 5. To obtain ΔU_β, parameter η_{02} at a temperature different from T_r is needed. It is calculated by applying equation (3.15) at the yield point at $T = 40\,°C$.

8. Next, shear moduli $G_i^a, i = 1, 2$ are determined. In the elastic regime, the stress is calculated using the following relation:

$$|\sigma| = \left| \lambda^2 - \frac{1}{\lambda} \right| (G_1^a + G_2^a + G_r), \qquad (B5)$$

from which $G_1^a + G_2^a$ is obtained. The individual values of G_k^a are identified such that the best fit of experimental data is obtained.

9. The last step is determining the softening parameters $r_{k\pi}, k = 0, 1, 2, \pi = \alpha, \beta$, which determine the shape of the stress-strain curve from the upper yield point to the lower yield point.

4 Anisotropic thermo-mechanical behaviour of oriented PET film*

Abstract: The long-term and short-term anisotropic mechanical behaviour of a biaxially stretched polyethylene terephthalate film is measured. The orientation of the crystalline phase is characterised and the representative film microstructure is discussed. Using the obtained information, a mean-field model is used to simulate the elasto-viscoplastic behaviour of the oriented polymer film, taking into account the different constitutive behaviour of the phases. The material is modelled as an aggregate of connected two-phase domains. The parameters of the constitutive behaviour of the crystalline and non-crystalline phases are determined and the ability to simulate the large-strain anisotropic behaviour of polyethylene terephthalate in the strain-rate-controlled regime and the long-term creep regime is demonstrated. The model is extended to include pre-orientation of the non-crystalline phase. In addition, deformation at the microscopic level is analysed using the model results.

4.1 Introduction

Application of polymer substrates to flexible electronics requires high stability and predictable mechanical response during processing [4]. The most commonly used materials are polyethylene terephthalate (PET) and polyethylene naphthalate (PEN), which can both exist in amorphous or semicrystalline states, but only semicrystalline, oriented and thermally stabilised PET and PEN films are used in such applications. The goal of this work is to predict the influence of the microstructure on the macroscopic material behaviour, and therefore to predict the dimensional stability of such films.

The material studied here is PET, for which a vast amount of data is available (orientation measurements [105, 106], crystal structure [24, 25], mechanical behaviour [47, 96], etc.). The film is produced by sequential biaxial stretching. Process parameters, such as drawing ratios, temperature, molecular weight and thermomechanical history, influence the resulting material structure [107], i.e. the orientation of the polymer molecules within the different phases of the material, which, in turn, influences macroscopic properties.

Various constitutive models might be used to simulate the macroscopic behaviour of isotropic

---

*This chapter is partly reproduced from [104].

polymer materials, such as the model by Buckley et al. [37,38], by Boyce et al. [39,40] and by Govaert et al. [41, 42]. By performing material characterisation once, such models can describe complicated deformation cases, for example, flat-tip micro-indentation and notched impact tests [43], or the large-strain behaviour of particle-reinforced composites with a polymer matrix [44]. Even though it is possible to use orientation distribution functions as internal state variables [47], detailed conclusions about microstructure evolution are difficult to obtain because of the absence of adequate descriptions of local microscopic deformation mechanisms. Therefore, multiscale modelling is preferred to investigate microstructure evolution and the role of the microstructure in macroscopic deformations. In such models, at the microscopic scale, various constituents are described with different constitutive laws, and the macroscopic behaviour is obtained through homogenisation: either full-field averaging or mean-field averaging, where effective coupling laws replace real interactions between domains. Extreme cases can be obtained by applying rules of mixtures (Voigt and Reuss bounds), i.e. parallel or serial connections of phases, which give the stiffest and the most compliant responses, respectively. The majority of homogenisation methods are based on Eshelby's problem, which in the elastic case and for an infinite medium has an exact solution. In case of elastic homogenisation, this solution (with some assumptions) is used in the self-consistent method [54] and the Mori-Tanaka method [59]. It is also possible to apply these methods in viscoplastic cases, for example, using an incremental approach [61], integral transformations [62] and more recently non-incremental formulations [63]. Alternatives to self-consistent methods are approaches based on variational principles, for example, [64]. In addition, there are many variations of these methods. More information and a comparison of some approaches of homogenisation of elasto-viscoplastic materials can be found in [63, 65, 66].

In [108], simple micromechanical models were used to determine the coefficient of thermal expansion (CTE) of PEN film at different locations. Voigt and Reuss models were applied to uniaxially and biaxially drawn films. Hybrid methods between the Voigt and Reuss interaction models also exist, constraining domains differently in distinct directions. For example, the composite inclusion model [73, 74, 83] has demonstrated a good match with measurements for the large-strain behaviour of HDPE. In this model, the macroscopic behaviour is an average of layered domains containing crystalline, amorphous and possibly other phases, between which a certain interaction law is imposed. The composite inclusion model has been used successfully in various applications, such as modelling the spherulitic morphology of polyethylene [78], qualitatively describing the behaviour of an oriented tensile bar under uniaxial stress [79], predicting the double yield phenomenon of HDPE [80] and simulating of the creep behaviour and predicting the time-to-failure of polyethylene [81]. In [78,79], this model was used in combination with the finite-element method, where it was used as a constitutive model of each material point, to simulate the inhomogeneous deformation of the material.

In terms of constitutive laws used within the composite inclusion model, crystal plasticity [98] is often used for the crystalline phase where viscoplastic deformation takes place on a limited number of slip systems. For the non-crystalline phase, one of the previously mentioned models can be used. In this work, the model by Govaert et al. [42] (referred to as the EGP model) is used.

Since polymer molecules may be strongly aligned in one or several directions in oriented polymers, creating highly anisotropic material, quantitative information on the molecular orientation, more specifically the orientation of crystals, is essential when mechanical behaviour is to be predicted. Moreover, polymer films are generally spatially inhomogeneous due to the specific production process, i.e. uniaxial or biaxial stretching. Therefore, variation of molecular orientation within the film should be taken into account as well. The aim of this work is to obtain a structure-property

relationship for an oriented PET film, i.e. to predict the macroscopic behaviour for different loading conditions, including short-term and long-term responses for various temperatures, based on the underlying microstructure. By characterising various deformation processes of the different constituent phases at the microscopic level and by modelling the interaction between these phases, a micromechanical model can be used to predict the macroscopic properties of this semicrystalline material.

To characterise the oriented material behaviour, several steps were made. Since in contrast to some other polymers PET can exist in the amorphous glassy state at room temperature, amorphous PET was studied first, see chapter 3. Thereafter, the isotropic semicrystalline material was characterised, also in chapter 3. In this work, it is shown that the obtained parameters for purely amorphous PET cannot be directly used to describe the non-crystalline phase in isotropic or oriented semicrystalline material, due to the presence of an intermediate phase with significant orientation of polymer molecules. In oriented material, the influence of the individual deformation processes on the macroscopic behaviour in different directions can be separated, and thus a more precise characterisation can be obtained.

In previous work, the micromechanical composite inclusion model was used for a qualitative and quantitative description of the viscoplastic behaviour of isotropic HDPE [80, 83] and PET (chapter 3) and for a qualitative description of the viscoplastic behaviour of oriented HDPE [79]. This work, for the first time, aims obtain a quantitative micromechanical description of oriented PET. For that purpose, the anisotropic yield behaviour of the non-crystalline phase was included by incorporation of an internal stress state of the phase, which is the result of film drawing.

4.2   Experimental methods

A polyethylene terephthalate film with an average thickness of 125 μm and a width of 90 cm was provided by DuPont Teijin Films. It was manufactured by sequential biaxial stretching (draw ratios λ = 3.0–3.5). The molten polymer was extruded into a film and subsequently longitudinally stretched (MD direction) on rollers with increasing speeds. Next, the film was stretched in the lateral (TD) direction to obtain a biaxial orientation. This PET film was manufactured on the same production line as the PEN film in [108]. During the manufacturing, the film was heat treated to reduce residual stresses and thus thermally stabilise the film. Small deviations of the film thickness were observed in both the length and width directions, whereas major deviations towards higher values were observed at the edges of the film. Samples for the mechanical tests were cut from the film with a shape according to ISO 527-2, type 1BA.

Constant strain rate and creep tests were performed under uniaxial tensile conditions on a Zwick Z010 universal tensile tester equipped with a video extensometer, a temperature controlled chamber and a 1 kN force cell. The engineering strain was calculated from video extensometer measurement of the distance between markers glued on the sample. As is common in testing of thin films, the measured stress-strain dependence showed a small non-linear start-up region, which was attributed to a small amount of slack in the specimen. Therefore, a strain correction was applied, in which the Young's modulus of the material was used to recalculate the initial distance between markers and thus obtain the correct engineering strain. This was especially important in case of creep compliance measurements, which due to the small strains are sensitive to a measurement error of the initial distance between markers.

The samples were cut in the machine direction (MD, also length direction), the transverse di-

rection (TD, also width direction) and other intermediate directions of the film. In the case of strain-rate-controlled tests, samples were tested up to an engineering strain of 0.4, although some samples, especially the ones which had been cut in TD, were failing at a smaller strain. After yield, the samples deformed homogeneously until failure was reached at a certain strain level.

The experimental programme was divided into four parts. The inhomogeneity within the film was first investigated. Initial measurements showed that the mechanical behaviour of the film was approximately homogeneous across the length but not across the width, due to the sequential manufacturing conditions. To quantify the inhomogeneity in the width direction, both the elastic and post-yield behaviour were considered. For the mechanical tests, an engineering strain rate of $10^{-3}\,\mathrm{s}^{-1}$ and a temperature of $22\,^{\circ}\mathrm{C}$, corresponding to the lab room temperature, were prescribed. For this particular comparison, the stretch ratio, and consequently the applied engineering strain rate, were calculated from the grip separation and not from the video extensometer. Also, to calculate the true stress and strain from engineering quantities, incompressibility was assumed. The second part consisted of quantifying the anisotropy of the film in selected positions across the width. To this end, samples were cut in different directions and tested as before. The third part was an investigation of the deformation rate dependence, for which mechanical tests, with a prescribed engineering strain rate varying from $10^{-5}\,\mathrm{s}^{-1}$ to $10^{-2}\,\mathrm{s}^{-1}$ were performed. The temperature of the tests was also varied: one set of samples was tested at room temperature ($22\,^{\circ}\mathrm{C}$) and another set at $50\,^{\circ}\mathrm{C}$. Such extensive testing, where sample orientation, strain rate and temperature were varied, was performed both at the central and right positions. For these tests and for creep tests, the engineering strain was measured using a video extensometer. The final part of the experimental programme consisted of tensile creep measurements. The same positions within the film were selected for testing as for the strain-rate-controlled tests. The creep behaviour of the film was found to be well reproducible.

4.3   Micromechanical modelling

A summary of the micromechanical model, referred to as the composite inclusion model, is given in this section. A more elaborate description can be found in section 3.A. For a detailed presentation of the model, see previous chapter or [83]. The behaviour of the material is simulated by relating the Cauchy stress $\boldsymbol{\sigma}^{\mathrm{M}}$ to the deformation gradient $\boldsymbol{F}^{\mathrm{M}}$ for a material point. A separation of scales is introduced with the material point scale in the model as the *macroscopic scale*. At the *microscopic scale*, a heterogeneous microstructure is considered. To take into account the microstructure and the existence of individual phases, the behaviour of the material point is modelled as the average behaviour of multiple differently oriented domains, each consisting of different phases, see figure 4.1.

The basic structural element of the generated microstructure is a layered entity, referred to as the composite inclusion [74]. For the material considered here, the entities consist of two layers: crystalline and amorphous (or, more precisely, non-crystalline), although the existence of three or more layers is possible [77]. Layers are mechanically connected, i.e. compatibility and equilibrium conditions are enforced at the interface:

$$\sigma_{n3}^{\mathrm{c}k} = \sigma_{n3}^{\mathrm{a}k}; \quad F_{ns}^{\mathrm{c}k} = F_{ns}^{\mathrm{a}k}; \quad k = \overline{1,N}; \quad n = \{1,2,3\}; \quad s = \{1,2\}, \qquad (4.1)$$

where components are taken with respect to the inclusion coordinate system shown in figure 4.1 (with unit vectors $\vec{e}_1^{\mathrm{I}}, \vec{e}_2^{\mathrm{I}}, \vec{n}^{\mathrm{I}}$). Superscripts "c", "a" indicate quantities belonging to the crystalline
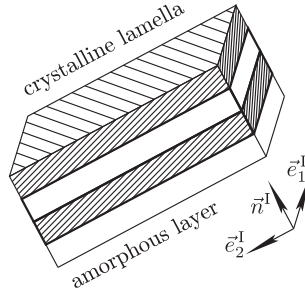
Figure 4.1: The two-layer composite inclusion after [74, 83]. The structural unit of the model is highlighted in a stack of crystalline lamellae.

and amorphous phases and N is the number of layered domains. Within the layer of a certain phase, the stress and the deformation are assumed to be homogeneous here and are related through a constitutive law. The average stress $\boldsymbol{\sigma}^{\mathrm{I}}$ and deformation gradient $\boldsymbol{F}^{\mathrm{I}}$ of the composite inclusion are obtained by volume averaging. To link multiple inclusions present in the microstructure, various interaction laws can be used. Here, based on the previous work of [74] and [83], an interaction law is selected for the components of $\boldsymbol{\sigma}^{\mathrm{I}}$ or $\boldsymbol{F}^{\mathrm{I}}$, which are not constrained by intra-inclusion equilibrium and compatibility conditions. More specifically, the components of the inclusion-averaged right stretch tensors, which are not constrained as in equation (4.1), are linked to an auxiliary deformation-like symmetric tensor $\hat{\boldsymbol{U}}$ [74, 83], while all rotation tensors $\boldsymbol{R}^{\mathrm{I}k}$ are fixed:

$$U_{n3}^{\mathrm{I}k} = \hat{U}_{n3}; \quad \boldsymbol{R}^{\mathrm{I}k} = \boldsymbol{R}^{\mathrm{M}}; \quad k = \overline{1, N}; \quad n = \{1, 2, 3\}. \tag{4.2}$$

Similarly, components of the inclusion-averaged stress tensors, which are not constrained as in equation (4.1), are linked to the macroscopic stress:

$$\sigma_{ps}^{\mathrm{I}k} = \sigma_{ps}^{\mathrm{M}}; \quad k = \overline{1, N}; \quad p, s = \{1, 2\}. \tag{4.3}$$

The macroscopic quantities $\boldsymbol{F}^{\mathrm{M}}$ and $\boldsymbol{\sigma}^{\mathrm{M}}$ are obtained by volume averaging the inclusion-averaged quantities $\boldsymbol{\sigma}^{\mathrm{I}}$ and $\boldsymbol{F}^{\mathrm{I}}$.

The non-crystalline phase is modelled with the EGP model [42, 46, 109], which is similar to a generalized Maxwell model with neo-Hookean-like elastic elements and non-linear viscosity elements. Viscoplastic deformation is modelled using the Eyring flow, i.e. the viscosity depends on the equivalent stress τ, the pressure p^{a}, the temperature T and the thermomechanical history S:

$$\eta_i = \eta_{0ir} \exp\left(\frac{\Delta U}{R}\left(\frac{1}{T} - \frac{1}{T_{\mathrm{r}}}\right)\right) \frac{\tau/\tau_0}{\sinh\left(\tau/\tau_0\right)} \exp\left(\frac{\mu p^{\mathrm{a}}}{\tau_0}\right) \exp\left(S\right); \tag{4.4}$$

$$\tau_0 = \frac{kT}{V^*}, \tag{4.5}$$

where R is the universal gas constant, ΔU is the activation energy, T_{r} is a reference temperature, k is the Boltzmann constant and V^* is the activation volume. In this model, multiple molecular relaxation processes can be taken into account. In chapter 3, the numerical implementation of this model is discussed.

To take into account the anisotropy of the non-crystalline phase, internal stresses were incorporated in a similar to that in [110]. Some model limitations resulting from this assumption are discussed later. Initial elastic isochoric pre-deformation of the molecular network is prescribed. The viscoplastic contribution has non-zero initial plastic deformation to obtain zero initial total deformation. Formally, the deformation gradient $\boldsymbol{F}_{\mathrm{r}}^{\mathrm{a}}$ corresponding to the molecular network is calculated from the total deformation gradient $\boldsymbol{F}^{\mathrm{a}}$ of the amorphous phase, i.e.

$$\boldsymbol{F}_{\mathrm{r}}^{\mathrm{a}} = \boldsymbol{F}^{\mathrm{a}} \cdot \boldsymbol{F}_{\mathrm{d}}^{\mathrm{a}}, \tag{4.6}$$

where $\boldsymbol{F}_{\mathrm{d}}^{\mathrm{a}}$ is a deformation gradient determining the initial pre-deformation of the network. Initial elastic $\boldsymbol{F}_{\mathrm{e}_i}^{\mathrm{a}}$ and plastic deformation gradients $\boldsymbol{F}_{\mathrm{p}_i}^{\mathrm{a}}$ are calculated such that the overall stress of the non-crystalline phase is zero, $\boldsymbol{\sigma}^{\mathrm{a}} = \boldsymbol{0}$, and the deformation gradient is equal to identity $\boldsymbol{F}^{\mathrm{a}} = \boldsymbol{I}$. In the original formulation of the EGP model, $\boldsymbol{F}_{\mathrm{r}}^{\mathrm{a}} = \boldsymbol{F}^{\mathrm{a}}$. It was found by numerical simulations that the pre-deformation state of the molecular network in the form of $\boldsymbol{F}_{\mathrm{d}}^{\mathrm{a}} = (1/\lambda_{\mathrm{d}})\,\vec{e}_1\vec{e}_1 + \lambda_{\mathrm{d}}\vec{e}_2\vec{e}_2 + \vec{e}_3\vec{e}_3$, with $\vec{e}_1$ corresponding to TD and $\vec{e}_2$ corresponding to MD, is closest to the experimental data. Thus pre-deformation is controlled by one parameter λ_{d}.

A crystal viscoplasticity model is used as a constitutive law for the crystalline phase [98], where the deformation is split into elastic and viscoplastic parts. The viscoplastic deformation is a superposition of slip taking place on a limited number of crystallographic slip systems. In each of the slip systems, the shear rate and shear stress are linked by an Eyring flow equation [81], i.e. the shear rate $\dot{\gamma}^{\alpha}$ of slip system α depends on the shear stress τ^{α} in the following way:

$$\dot{\gamma}^{\alpha} = \xi^{\alpha} \sinh \frac{\tau^{\alpha}}{\tau_0^{\alpha}}. \tag{4.7}$$

The parameters ξ^{α} and τ_0^{α} are the reference shear rate and characteristic stress of slip system α and cannot be measured directly. The process of identification of these parameters involves a comparison of the macroscopic behaviour of the micromechanical model with experimental data.

4.4　Microstructural characterisation

The crystal structure of PET is triclinic and its lattice parameters, determined by molecular modelling [25], are given by: $a = 0.448\,\mathrm{nm}$, $b = 0.602\,\mathrm{nm}$, $c = 1.086\,\mathrm{nm}$, $\alpha = 102.5°$, $\beta = 119.8°$, $\gamma = 107.0°$ (at $T = 300\,\mathrm{K}$). Details of the molecular chain arrangement can be found in [24–26].

To generate a microstructure, which is used in the micromechanical model, information about the orientation distribution of the crystalline phase is required. Here, the orientation distribution of crystals is described by empirical probability density functions with three parameters, which are provided (film draw ratio), measured (dominant chain direction) or fitted. In biaxially stretched PET film, crystals are oriented in such a way that the (100) crystallographic plane is almost aligned with the plane of the film [105], i.e. molecular chains are lying almost parallel to the film plane and benzene rings are almost at an angle of $21°$ to the film surface (if atomic positions are taken from [26]). The orientation of chains within the film surface is non-homogeneous and depends on the production process [107, 111]. Therefore, this orientation distribution should be quantified separately for different positions and different films.

In this work, three coordinate systems are used. The global coordinate system is linked to the polymer film with the unit vectors $\vec{e}_1$, which correspond to the transverse direction (TD), $\vec{e}_2$, corresponding to the machine direction (MD) and $\vec{e}_3$ corresponding to the surface normal direction
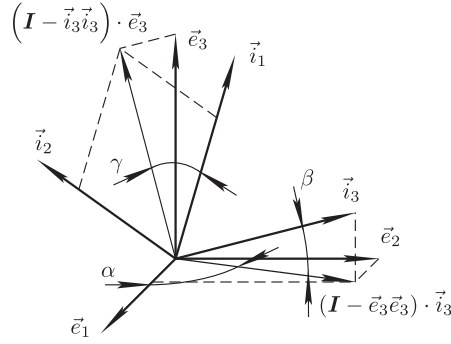
Figure 4.2: Global and local coordinate systems.

(ND). The local coordinate system is linked to the individual crystals with unit vectors $\vec{i}_1$, which is normal to the (100) crystallographic plane, $\vec{i}_2$ and $\vec{i}_3$, which corresponds to the chain direction [001]. An illustration of molecular chains in the crystal with respect to the coordinate system $\vec{i}_k$ can be found in chapter 3. The third coordinate system, with unit vectors $\vec{e}_1^{\mathrm{I}}$, $\vec{e}_2^{\mathrm{I}}$ and $\vec{n}^{\mathrm{I}}$, is linked to the interface between phases as shown in figure 4.1. To fully quantify the distribution of the crystalline phase, cumulative distribution functions are specified for 3 angles, see figure 4.2. Angle $\beta \in [0; \pi/2]$ is the angle between the polymer film surface (the surface spanned by the global $\vec{e}_1$ and $\vec{e}_2$ directions) and the molecular chain direction (local $\vec{i}_3$), which is assumed to be described by the following distribution density:

$$f_1(\beta) = \frac{C}{\left((\lambda^6 - 1) \sin^2 \beta + 1 \right)^{1.5}}, \tag{4.8}$$

where λ is the draw ratio, thus defining how close the chains are to the film surface, and C is a normalisation constant, such that $C = 1/\Pi \left(1 - \lambda^6, \sqrt{1 - \lambda^6} \right)$ with $\Pi(n, m)$ being the complete elliptic integral of the third kind. This distribution density function is similar to that used by [105]. The angle $\gamma \in [0; \pi/2]$ is the angle between lines $\left(\mathbf{I} - \vec{i}_3 \vec{i}_3 \right) \cdot \vec{e}_3$ and $\vec{i}_1$, thus defining how parallel the (100) crystallographic planes are to the film surface, where $\mathbf{I}$ is the second order identity tensor. The distribution density function $f_2(\gamma)$ for γ is taken to be the same as for β, equation (4.8). Finally, angle $\alpha \in [0; \pi]$ is the angle between $\vec{e}_1$ (TD) and the projection of the chain direction to the film surface; more precisely, the angle between lines $(\mathbf{I} - \vec{e}_3 \vec{e}_3) \cdot \vec{i}_3$ and $\vec{e}_1$, thus defining the distribution of chains within the film plane. A Tikhonov distribution density (also von Mises distribution, [112]) is selected for α:

$$f_3(\alpha) = \frac{e^{\kappa \cos(2\alpha - \mu)}}{\pi I_0(\kappa)}, \tag{4.9}$$

where $I_0(\kappa)$ is the modified Bessel function of the order 0. The parameters for the distribution functions (4.8) and (4.9) are discussed later.

If the orientation of a single crystal is considered, then the case with $\beta = 0$ corresponds to the orientation when the polymer chains, i.e. the [001] directions, are lying in the film plane. If $\beta = 0$

and $\alpha = 0$, then the crystal orientation is such that the chain direction corresponds to TD, while $\beta = 0$ and $\alpha = \pi/2$ give a chain orientation corresponding to MD. If $\beta = 0$ and $\gamma = 0$, then the (100) crystallographic plane is parallel to the surface of the film.

In addition to the orientation of the crystalline phase, the orientation of the interface between two phases, i.e. the lamellar surface normal, should be specified. Normally, the orientation of the interface is specified relative to the crystalline unit cell. In the case of isotropic PET, the [101] crystallographic direction is considered to be normal to the lamellar surface [10,26,89], which corresponds to an angle between the molecular chain axis and the lamellar normal of $\varphi \approx 25°$. However, in the case of oriented PET, other stable configurations are observed depending on the drawing conditions both in the films and fibres [106, 113]. One of the configurations is $\varphi \approx 0°$, and another $\varphi \approx 46$–$52°$. Based on [106,113], for the simulations, this angle was taken as $\varphi \approx 50°$, since film draw ratios (during manufacturing) were relatively small. Furthermore, it was assumed that in the case of oriented PET, the lamellar normal is lying in the (010) plane, similar to the case for isotropic material, thus corresponding to the [201] crystallographic direction.

As outlined in section 4.3, the multiscale model simulates the behaviour of the material as the behaviour of a collection of anisotropic two-phase layered domains. The spatial orientations of these domains (inclusions) define the microstructure of the material. The discrete set of orientations is generated using continuous probability density functions for angles between certain crystallographic directions and the axes of the global coordinate system. These orientations were generated in the following way: first, parameters for the distribution densities of angles α, β and γ were selected. Then, N sets of 3 angles were generated, fully defining the orientation of N crystals. Finally, by using information about the interface orientation with respect to the crystal, the orientations of N interfaces were calculated from the orientations of the crystals.

The parameter controlling the alignment of (100) planes with respect to the film normal was selected as $\lambda = 3$ (as mentioned in section 4.2, the film draw ratio is 3.0–3.5). A more detailed discussion on the relation between this parameter and the film draw ratio can be found in [105]. At the center of the film, polymer chains are mainly oriented in MD, and therefore the parameter μ was selected to be $\mu = \pi$. The last parameter, $\kappa = 2$, was fitted to the mechanical measurements. The latter parameter is controlling the spread around the mean value, i.e. $1/\kappa$ is analogous to the variance in the case of a normal distribution.

The adopted distribution functions and parameters were compared and found to be similar to experimentally measured distributions by WAXD, see figure 4.3. From diffraction data, two distribution densities were obtained: for the angle between ND and the normal to the (100) plane (angle $\delta = \arccos\left(\cos\left(\beta\right)\cos\left(\gamma\right)\right)$), and for the angle between TD and the normal to the ($10\bar{5}$) plane (angle χ)*. The first can be compared to a distribution density function $f_4\left(\delta\right)$, calculated from functions $f_1\left(\beta\right)$ and $f_2\left(\gamma\right)$, since in the model, the direction of the normal to the (100) plane results from two rotations (by angles β and γ). The second distribution density function can be compared to $f_5\left(\chi\right)$, which is calculated numerically from functions $f_1\left(\beta\right)$, $f_2\left(\gamma\right)$ and $f_3\left(\alpha\right)$. For the PET crystal, the angle between the ($10\bar{5}$) plane normal and the chain direction [001] is $14.6°$, i.e. α and χ are close and do not differ by more than $14.6°$. Due to experimental inaccuracy, different values are observed at $\chi = 0°$ and $\chi = 180°$.

---

*These angles are random variables with their own cumulative distribution functions $F^{(100)}\left(\delta\right)$ and $F^{(10\bar{5})}\left(\chi\right)$, which show the probability that a crystal is oriented such that the angle between ND and the normal to the (100) plane and the angle between TD and the normal to the ($10\bar{5}$) plane are less than or equal to δ and χ respectively. Intensities plotted in figure 4.3 are probability density functions, i.e. derivatives of the cumulative distribution functions. Here experimentally obtained and numerically calculated probability densities are labelled as I and f respectively.
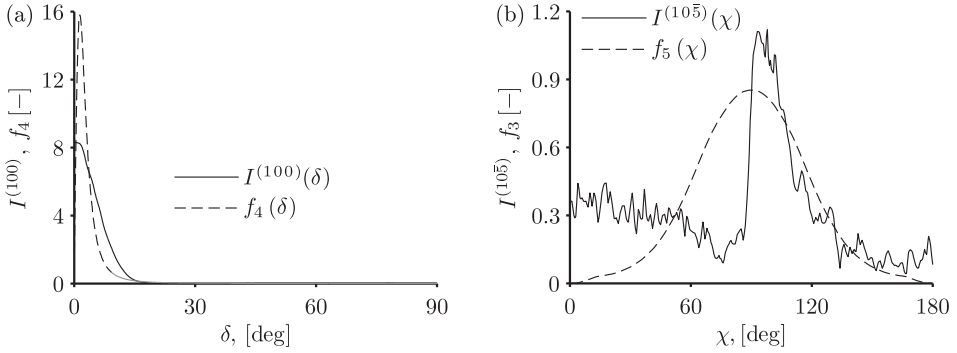
Figure 4.3: Distribution density $I^{(100)}$ of the angle between ND and the normal to the (100) plane (angle δ) and distribution density $I^{(10\bar{5})}$ of the angle between TD and the normal to the $(10\bar{5})$ plane (angle χ), obtained from diffraction intensities (WAXD) of (100) and $(10\bar{5})$ planes*, compared to distribution density functions of angles δ, χ used to generate crystal orientations for the model (see text for explanation).
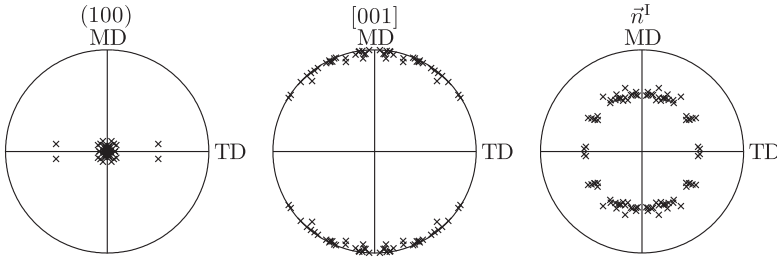

Figure 4.4: Equal area projection pole figures showing the initial crystallographic orientations (normal to the (100) plane and the $[001]$ direction) and the normal to the inclusion interface ($\vec{n}^{\mathrm{I}}$).

Based on these probability density functions and information about the crystalline-amorphous interface, a set of 100 inclusions corresponding to the centre (C) of the film was generated. This number of inclusions was found to be sufficient, based on a comparison of the mechanical behaviour of the model with different aggregate sizes, see 4.B. The set of orientations corresponding to the centre is demonstrated in equal area projection pole figures in figure 4.4. In section 4.6, the parameter κ is varied and different sets of orientations were used for that variation.

---

*The PET film, which was used for mechanical measurements, was subjected to WAXD. The pole figures showing the orientations of (100) and $(10\bar{5})$ planes were provided by Rigaku. From these pole figures distribution densities were calculated.
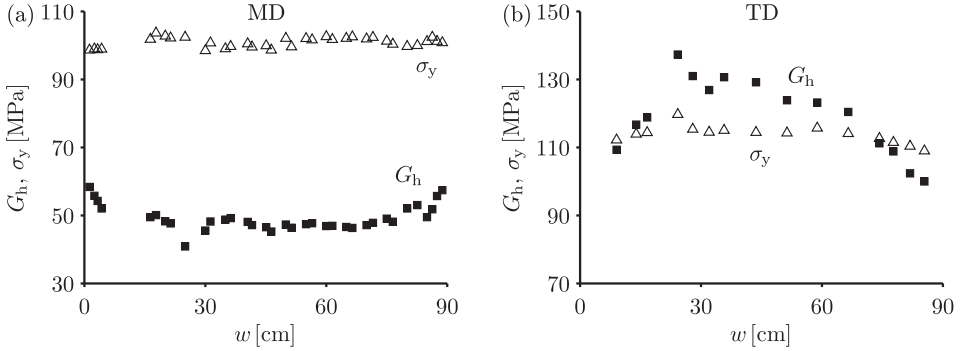
Figure 4.5: Hardening modulus and the yield stress at different positions across the width of the film, measured in MD (a) and TD (b). The centre of the film corresponds to $w = 45\,\text{cm}$.

4.5 Macroscopic characterisation

4.5.1 Inhomogeneity

The elastic modulus and yield stress were approximately constant across the width of the film for both the MD and TD cut samples, however the post-yield behaviour differed significantly for different regions of the film, see figure 4.5. This can be quantified through the hardening modulus G_h, which is the slope of the true stress σ versus the strain measure $\varepsilon_\text{r} = \lambda^2 - \lambda^{-1}$, where λ is the stretch ratio, which is based on a neo-Hookean description of the post-yield material behaviour under uniaxial loading. In figure 4.5, it is clearly seen that the central part of the film is close to homogeneous, but the sides of the film show a different post-yield behaviour. The reason for this is the difference in the underlying microstructure, i.e. the orientation of the crystalline phase and non-crystalline regions in these parts of the film. Here, the yield point was calculated as the intersection of two linear approximations of the true stress $\sigma\left(\varepsilon_\text{r}\right)$ in the elastic region and in the large strain region.

4.5.2 Anisotropy

Based on the information on film inhomogeneity, several positions across the width of the film were selected for further characterisation:

- left: $w = 5\text{–}15\,\text{cm}$ (L),
- centre: $w = 40\text{–}50\,\text{cm}$ (C),
- right: $w = 75\text{–}85\,\text{cm}$ (R).

To characterise the anisotropy of the film, samples cut in different directions were tested. In figure 4.6, the Young's moduli for different loading directions and for different parts of the film (L, C and R) are shown. The effect of orientation is clearly seen with TD being stiffer than MD. The behaviour appears to be symmetric with respect to MD at the centre of the film. The dominant
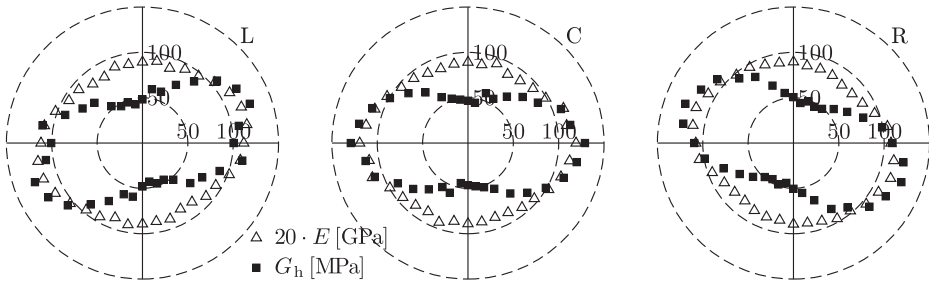
Figure 4.6: Young's moduli (scaled) and hardening moduli at different loading angles at 22 °C for the left, centre and right parts of the film.

direction, along which the molecular chains are aligned, changes along the width of the film, and therefore plots appear to be rotated at the sides by approximately 15°. It was found that the post-yield regime also shows the same trend, i.e. the hardening modulus at different loading angles is rotated by 15° at the side of the film compared to the centre (result not shown here).

Although some difference in the elastic and yield behaviour was observed at the selected positions of the film, the largest differences in the stress-strain dependencies were in the post-yield regime, see figure 4.5. This is due to two main mechanisms: (i) for different loading angles, different crystallographic slip systems in the crystalline phase are active; (ii) anisotropic crystals, having a preferential orientation, are constraining the deformation of neighbouring non-crystalline domains in some directions, allowing it to deform easily in other directions.

4.5.3 Deformation rate dependence

The deformation rate dependence of the samples cut in MD and TD is shown in figure 4.7, where the engineering stress-strain response for different temperatures is given. In the centre of the film, MD and TD demonstrate an extreme post-yield behaviour, however, at the side of the film the difference between MD and TD is smaller, since the dominant molecular orientation is different than in the centre. Later, these results are compared with the simulations.

4.5.4 Creep

The influence of the applied stress on the creep compliance is demonstrated in figure 4.8a. Obviously, the strain measurement error increases with decreasing applied stress; however, the magnitude of the applied stress is limited by the high temperature compliance. A significant increase of the creep rate is observed when the applied stress is larger than 15 MPa, which demonstrates the non-linear dependence of the material viscosity on stress. A similar behaviour has been observed for other polymers, for example PE fibres [114].

Positions C and R were tested to investigate the difference in macroscopic properties of the film across the width and to relate it to the molecular orientation, see figure 4.8b. No significant difference in the compliances of the C and R positions was observed. The differences are in the same order of the measurement accuracy. A comparison was performed of compliances of the samples from the centre of the film cut in MD and TD with the samples from the right side of the film cut
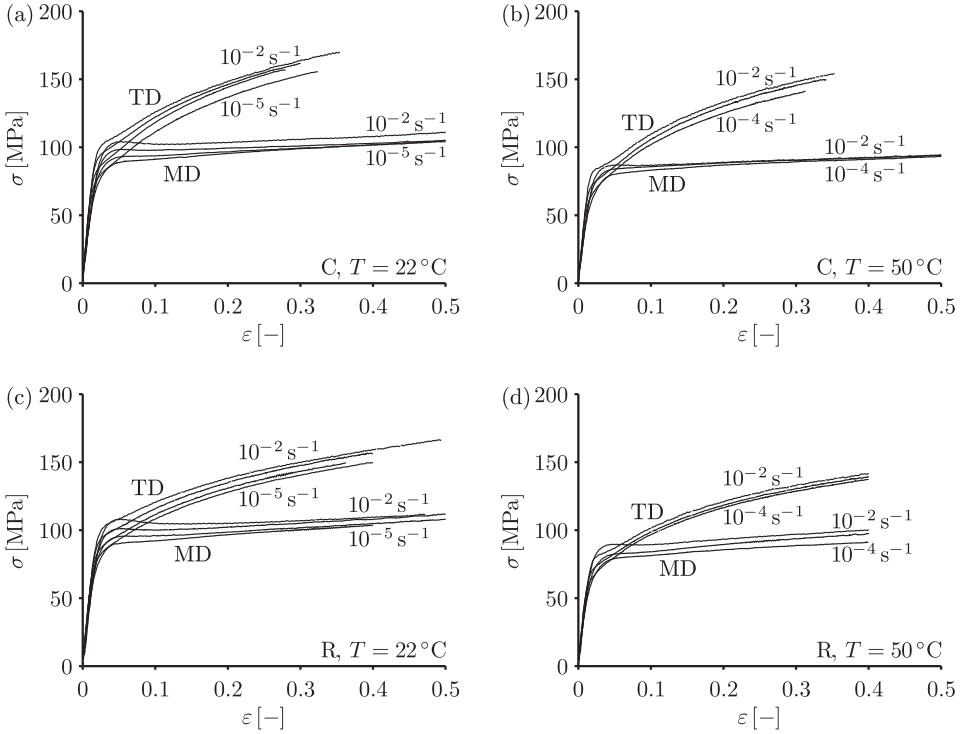
Figure 4.7: Engineering stress-strain response of oriented PET film under uniaxial tension at different strain rates, at $22\,°C$ (a,c) and at $50\,°C$ (b,d); comparison of centre of the film (a,b) and right side of the film (c,d).

in $+75°$ and $-15°$, respectively (results not shown here). At $+75°$ and $-15°$, the elastic moduli are the lowest and highest at the right side, comparable to MD and TD in the centre. Again, only minor differences, comparable to experimental accuracy, were observed.

The creep behaviour at various temperatures and an imposed stress of $\sigma_c = 5\,MPa$ of the samples cut in MD and TD is shown in figure 4.9. From the measured results a master curve was obtained (creep compliance of a non-ageing sample loaded with 5 MPa and at $50\,°C$) using time-temperature superposition, see figure 4.10. At temperatures above T_g, shift factors can be fitted by the Arrhenius equation, i.e. a linear dependence between the shift factor $\log(a_T)$ and $1/T$, for which the activation energy is $\Delta U = 138\,kJ/mol$ for both MD and TD. The Arrhenius fit was obtained only for points above $T_g \approx 70\,°C$, i.e. for temperatures above $80\,°C$, see figure 4.10b, since the creep compliance below T_g also depends on the thermomechanical history, i.e. on the material age [115, 116]. Below the glass transition temperature and in the region of T_g, the shift factor $\log(a_T)$ is non-linear and is lower than the calculated linear fit using data above T_g.

For semicrystalline polymers the glass transition of the constrained non-crystalline region is not as fast as for polymers in the amorphous state, leading to a different T_g. Therefore, different temperature regimes should be considered [116]. Since for amorphous PET, the glass transition is around $70\,°C$, the considered regime in figure 4.9, with the exception of the lowest creep compliance curve
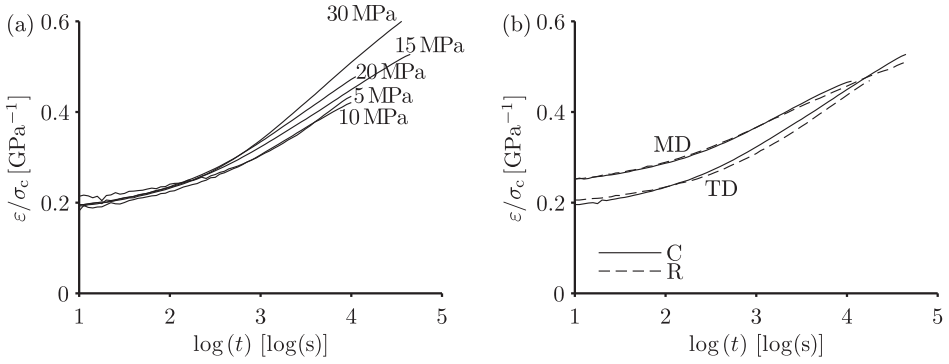
Figure 4.8: Creep compliance at $70\,^\circ\mathrm{C}$ in TD of the film at different applied stresses, position C, (a); at applied stresses $\sigma_\mathrm{c} = 15\,\mathrm{MPa}$, comparison of positions C and R (b).
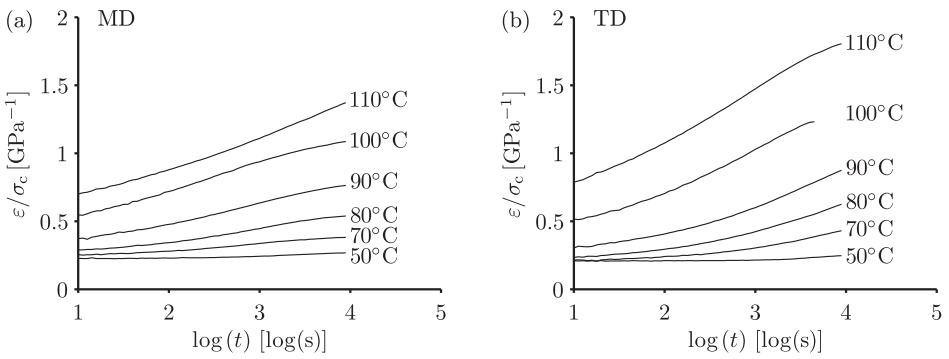

Figure 4.9: Creep compliance at different temperatures for an applied stress $\sigma_\mathrm{c} = 5\,\mathrm{MPa}$, comparison of MD (a) and TD (b) for the central part of the film.

(completely glassy state), is the regime where the non-crystalline material is partially in the glassy state, which leads to ageing effects causing a decrease in the rate of change of creep compliance at relatively large test times. This effect is observed in figure 4.10 as deviations of the compliance curves from the master curve. This effect was verified experimentally by measuring the creep compliance of samples annealed for a certain amount of time at the test temperature before the measurement (results not shown here). After manufacturing, a certain thermomechanical history is already present in the material (the material is "aged" with effective age t_e), and therefore the effect of progressive ageing, i.e. the evolution of properties during the test, can be observed only in cases where the test time exceeds the order of magnitude of t_e [116], which depends on the test temperature. Therefore, a master curve (representative for age t_e) is constructed using only parts of the compliance curves where no progressive ageing is observed, $t < t_\mathrm{e}$. The obtained creep curves are used for the model comparison for a sample with a constant age.
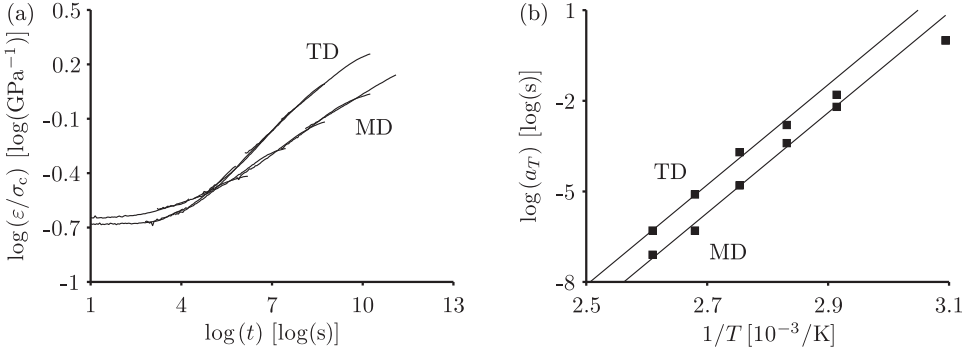
Figure 4.10: Creep compliance master curve for the centre of the film at $50\,^{\circ}\mathrm{C}$ at an applied stress $\sigma_{\mathrm{c}} = 5\,\mathrm{MPa}$ (a) and shift factors (b).

4.6 Modelling short-term behaviour

As outlined above, oriented PET is a semicrystalline material with a crystallinity depending on processing conditions. For the material studied here, the crystallinity was measured (by X-ray diffraction) to be $f_{\mathrm{c}} = 0.5$. PET has a triclinic crystal structure and its unit cell dimensions and elastic parameters were taken from [25]. More details can be found in chapter 3 where the micromechanical model was applied to isotropic PET. From the same source, the parameters for the non-crystalline phase were taken, although with some modifications. In section 4.7, the relaxation spectrum of the material is extended to model the tensile creep behaviour. A full list of the model parameters can be found in 4.A.

Plastic deformation in a polymer crystal is assumed to occur due to crystallographic slip. There are 3 possible slip systems in the PET crystal: $(100)[001]$ and $(010)[001]$ chain slip and $(100)[010]$ transverse slip [34]. To characterise the material behaviour, the parameters of these slip systems should be identified. The initial values for these parameters are those from the isotropic material. Physically, the slip system behaviour in the isotropic or oriented case is the same, however from the isotropic response, the parameters of the slip systems cannot be uniquely identified. For oriented material, the activity of the slip systems can be separated, as is shown later. It was observed that by varying only the slip system parameters, the macroscopic behaviour of the oriented film observed in the experiment cannot be described by the model. This indicates that due to the presence of the constraining neighbouring lamellae, the mechanical response of the non-crystalline phase most likely differs from that of purely amorphous PET. For the isotropic semicrystalline material this was not taken into account and the non-crystalline phase was modelled with a viscosity of purely amorphous PET. However, for the oriented material behaviour, it was not possible to obtain a fit with this viscosity value, and therefore a parameter variation study was performed which established a significantly higher viscosity of the non-crystalline phase than of the amorphous material, i.e. the relaxation spectrum shifts towards higher relaxation times. Additionally, the anisotropy of the non-crystalline phase was incorporated using an anisotropic internal stress, due to pre-orientation, which affects the yield and post-yield response. The parameter that controls the anisotropy of the non-crystalline phase within the film plane $(\vec{e}_1, \vec{e}_2)$, $\lambda_{\mathrm{d}} = 1.25$ (pre-deformation), was fitted based on the long-term response, since it was much more sensitive to the incorporated internal stresses. In

the simulation of the long-term response, the creep compliance in TD is proportional to the value of λ_d and the creep compliance in MD is reversely proportional to λ_d. The same parameter value was used for the simulations of the short-term behaviour.

The effect of the variation of different parameters is demonstrated in figure 4.11. For the simulations, an engineering strain rate of $10^{-3}\,\text{s}^{-1}$ was prescribed. The following effects are observed:

- The variation of crystallinity, $f_c = 0.4, 0.5, 0.6$, influences the hardening modulus in both directions simultaneously, and also increases material stiffness, see figure 4.11a. Based on X-ray measurements conducted for oriented PET material, a value $f_c = 0.5$ was chosen.

- By increasing the parameter $\lambda_d = 1, 1.25, 1.5$, the yield stress in the case of MD loading becomes higher, which is a consequence of the stretched state of the hardening spring (in the EGP model used for the non-crystalline phase). In the case of TD loading, it is the opposite due to the compressed state of the hardening spring.

- The ageing parameter $S_a = 0, 4, 8$ controls the yield stress and subsequent softening phase, see figure 4.11c. Although different parts of the non-crystalline phase age differently due to constraints from the crystalline phase, here only a homogeneous average age of the non-crystalline phase is taken into account. Therefore, this parameter was determined to be $S_a = 0$.

- The orientation distribution parameter $\kappa = 0.5, 2, 10$ determines to which degree the crystalline phase is oriented in one direction, see figure 4.11d. The value $\kappa = 0$ corresponds to the case where the chain direction [001] has a uniform distribution within the plane spanned by $\vec{e}_1$ and $\vec{e}_2$, i.e. there is no difference between MD and TD. The highest value will correspond to the largest difference between both directions. For details about the orientation distribution of the crystalline phase, see section 4.4. The value $\kappa = 2$ was determined by comparing simulations with the conducted mechanical tests, as well as from the orientation distribution in similar films [107, 108, 111] obtained by WAXD experiments.

In figure 4.12a, the constitutive behaviour of the crystalline slip systems is demonstrated for different parameter variations. The following observations can be made (for an engineering strain rate of $10^{-3}\,\text{s}^{-1}$):

- The viscosity of the non-crystalline phase influences the stress level in the yield and the post-yield regime, see figure 4.13a (values of $2.5\cdot10^{11}$, $2.5\cdot10^{16}$ and $2.5\cdot10^{21}\,\text{MPa}\cdot\text{s}$ used). The shape of the curves is almost unaffected, and therefore only a shift of the post-yield regime is observed. Here, based on this variation, a value of $2.5\cdot10^{16}\,\text{MPa}\cdot\text{s}$ results.

- In oriented PET, due to anisotropy of the crystal, the transverse slip system $(100)[010]$ is activated only at large deformations. This is even the case when the slip resistance on this slip system is relatively low. The variation of the behaviour of this slip system is shown in figure 4.13d (more precisely, parameter ξ^3 is varied: $\xi^3 = 10^{-25}, 10^{-30}, 10^{-35}\,\text{s}^{-1}$, for details about constitutive behaviour see 3.3.2).

- The slip resistance of the $(010)[001]$ chain slip system should be relatively high. Otherwise, the hardening modulus in the case of TD loading differs significantly from the experimental one. In figure 4.13c, the behaviour of this slip system is varied. The parameter $\xi^2 = 10^{-40}, 10^{-80}\,\text{s}^{-1}$ is used, where the first value was found by simulating isotropic material behaviour. The second value is selected such that this slip system remains inactive.
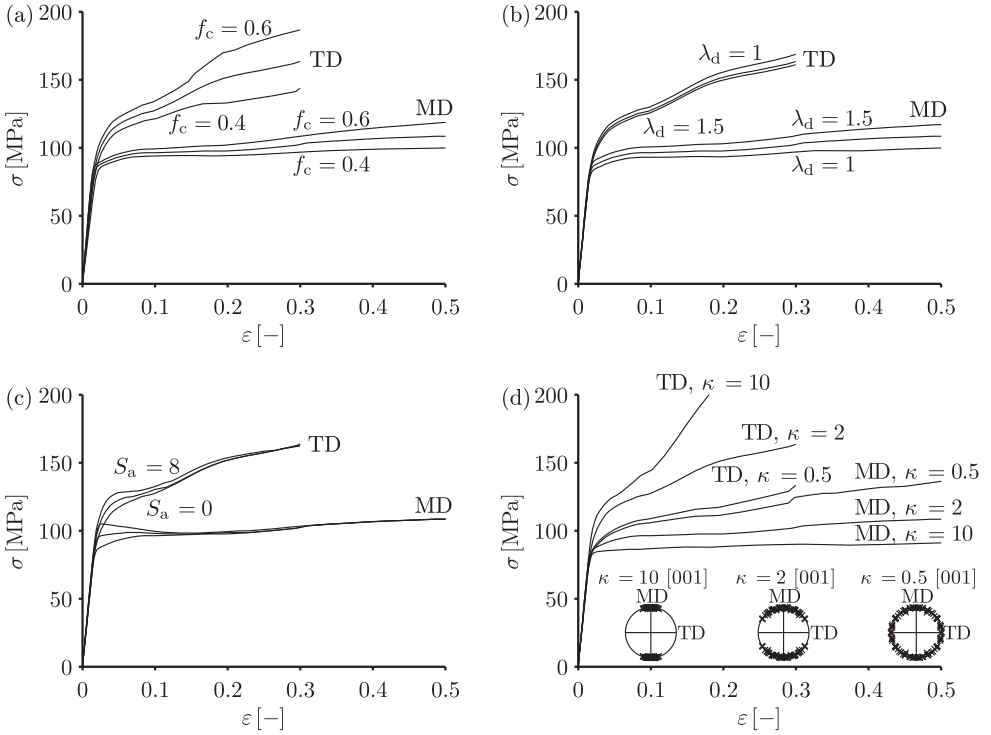
Figure 4.11: Simulated engineering stress-strain response of oriented PET film under uniaxial tension at $22\,^\circ$C, centre of the film. Multiple lines are results obtained with different values of varied parameters, for details see text.

- The slip resistance of the $(100)[001]$ chain slip system influences the hardening modulus and the shape of the stress-strain curve in the case of MD and TD loading. The parameter ξ^1 was varied, such that $\xi^1 = 10^{-11}, 10^{-16}, 10^{-21}\,\mathrm{s}^{-1}$. The results are shown in figure 4.13b.

So far, only one strain rate and one temperature were considered. Although the rate dependence of the non-crystalline phase can be taken to be the same as the rate dependence of amorphous PET, which can be characterised separately (see chapter 3), the rate dependence of the slip systems can be determined only by either comparing the effective behaviour of semicrystalline material or by molecular modelling. When considering the experimental stress-strain response in figure 4.7, it is noticed that the rate dependence changes at large strains. By only varying of the shear resistance of the slip systems τ_0^α only, this effect could not be captured quantitatively, although qualitatively this effect was definitely observed yet very small. In the model with the selected parameter set, the rate dependence effect is dominated by the non-crystalline phase. For the simulations, a value $\tau_0^\alpha = 1.1\,\mathrm{MPa}$ was used, which is a value representative of isotropic PET*.

---

*The parameter τ_0^α is proportional to the τ_0 of the non-crystalline phase, such that $\tau_0^\alpha = \chi\tau_0$ with the coefficient $\chi = 0.866$ because of the different definitions of shear stress on the slip plane in the crystalline phase and the equivalent stress in the amorphous phase [83].
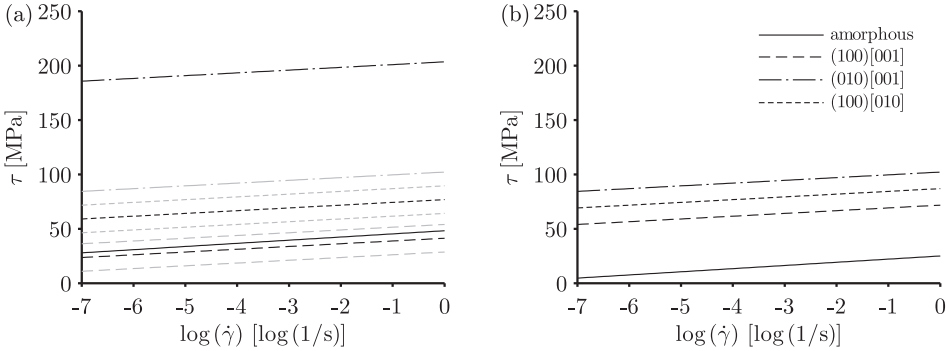
Figure 4.12: Constitutive behaviour of the slip systems of the crystalline phase in comparison to the yield kinetics of the amorphous phase: behaviour with parameters used for simulations (black lines) compared to variations of ξ^α (grey lines) (a) and behaviour with parameters used for simulations in chapter 3 with legend indicating processes (b).

Finally, a comparison of experimental data and simulations is shown in figure 4.14. Although the macroscopic hardening modulus is close to the experimentally measured one, there are some differences in the yield stress and shape of the stress-strain curve in the post-yield regime. The latter may be due to inaccuracies in the orientation distribution or limitations in the model imposed by the interaction law between the domains. Also, the deformation rate dependence appears to be different in the simulated behaviour at $50\,^\circ$C due to imprecise mechanical measurements, most probably due to small strain localisations taking place for the set of samples corresponding to the centre. As observed in figure 4.7, for the set of samples cut from the right part of the film, the rate dependence was the same at high temperature. Temperature dependence was taken into account only in the non-crystalline phase. A temperature dependence of the slip systems, i.e. an increase of shear rate of slip systems with temperature, does not further improve the model predictions.

Based on the mechanical behaviour of the isotropic semicrystalline material, which can be obtained by annealing amorphous PET, the deformation kinetics of the various slip systems cannot be determined uniquely, since the effect of various crystallographic slip systems cannot be isolated. For oriented material, obtained by substantial uniaxial or sequential biaxial drawing at high temperatures, due to the presence of a preferential orientation of the crystalline phase, the influence of individual slip systems can be separated to some extent by applying deformation in different directions. Thus, the parameters of the constitutive laws describing the behaviour of individual slip systems can be identified more precisely. In figure 4.12, the resulting constitutive behaviour is compared to the behaviour with parameters identified for isotropic PET in chapter 3. Although the set of parameters provided here differs from the set obtained in chapter 3, it is possible to describe the macroscopic behaviour of the isotropic material with the current parameter set.

Another structural effect that can be predicted by the model is the influence of the microstructure at different positions of the film on the macroscopic behaviour, although, as discussed in section 4.5, the difference between the centre and right positions is relatively small. In section 4.5, it was shown that based on the macroscopic behaviour, the microstructure at the side of the film is rotated by 15° compared to the centre. Therefore, to investigate the full anisotropy of the microstructure,
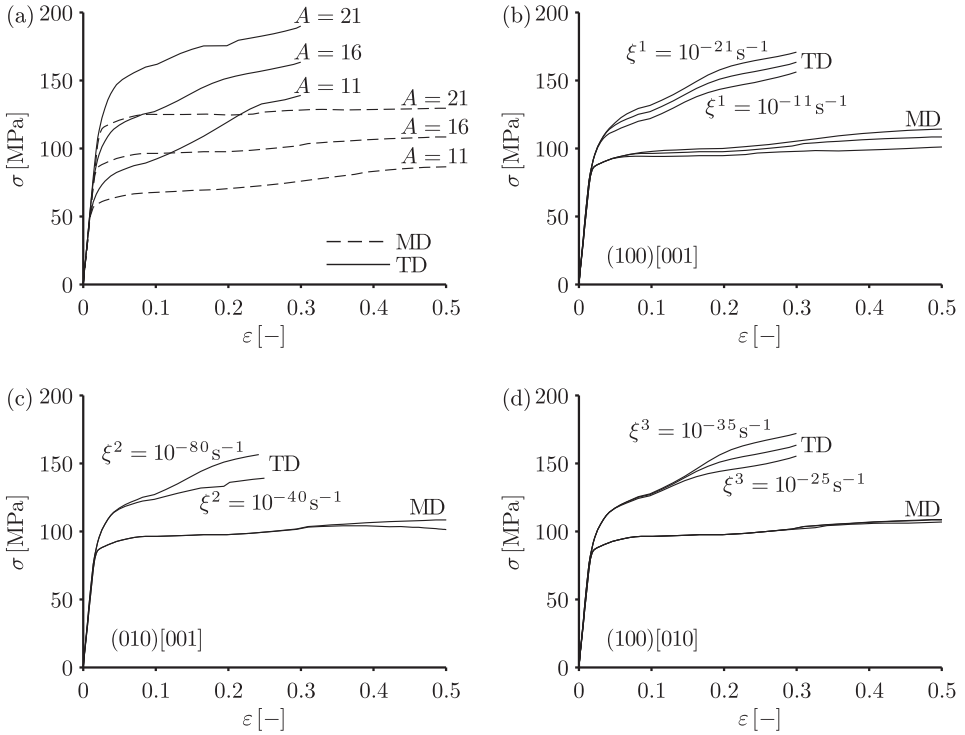
Figure 4.13: Simulated engineering stress-strain response of oriented PET film under uniaxial tension at $22\,°C$, centre of the film. Multiple lines are results obtained with different value of viscosity of the non-crystalline phase ($\eta_{0ir} = 2.5 \cdot 10^A\,\mathrm{MPa}\cdot\mathrm{s}$) (a) and values of parameters of the slip systems (b-d), for details see text.

the hardening moduli at different loading angles of simulated and measured stress-strain response are compared, see figure 4.15. In the model, the hardening modulus clearly has a minimum in the MD region ($\alpha = 90°$), as in the experiment. In the region close to TD, the model results deviate from the experimental data, and therefore the effect of a small variation in the rotation of the microstructure cannot be simulated precisely. However overall, the load angle dependence is adequately predicted, which allows to simulate anisotropic behaviour of different parts of oriented film.

At the microscopic level, deformation can be characterised by the average absolute plastic shear rates for the different slip systems of the crystalline phase of all inclusions and the average equivalent plastic strain rate of the amorphous phase. In figure 4.16, these quantities normalised by the applied strain rate $\dot{\varepsilon} = 10^{-3}\,\mathrm{s}^{-1}$ are demonstrated. No significant differences in normalised slip system activity are observed for different strain rates. In both the MD and TD loading cases, the (010)[001] chain slip is not active due to the parameter obtained for this slip system, as has already been shown. It can clearly be seen that the major plastic deformation happens in the non-crystalline phase. Moreover, the observed influence of the slip system parameters on the macroscopic behaviour are also
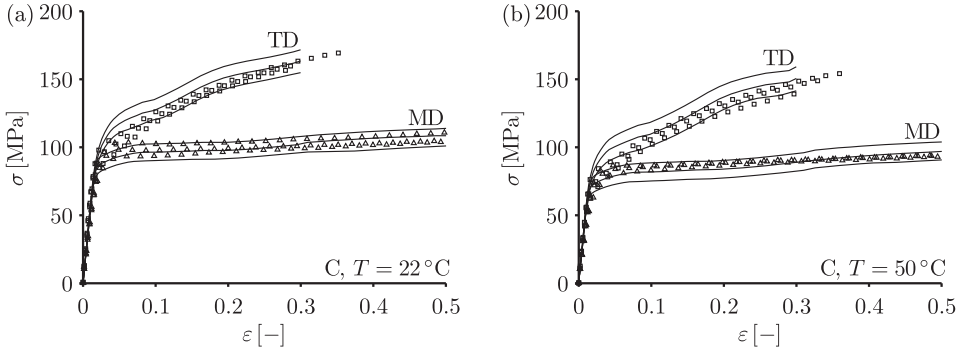
Figure 4.14: Simulated engineering stress-strain response (lines) of oriented PET film under uniaxial tension at $22\,^{\circ}\mathrm{C}$ (a) and $50\,^{\circ}\mathrm{C}$ (b) compared to experimental data (symbols). Multiple lines are results obtained at different applied strain rates: $10^{-2}, 10^{-3}, 10^{-4}\,\mathrm{s}^{-1}$.
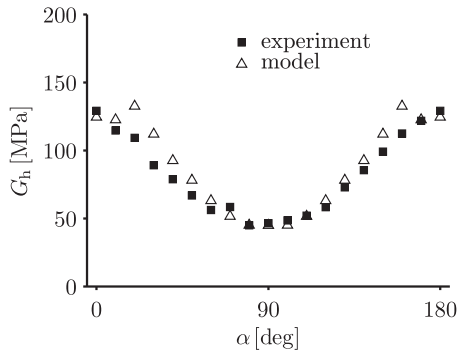

Figure 4.15: Hardening modulus depending on loading angle at the centre of the film, comparison of the simulated and experimental data.

confirmed at the microscopic scale. In case of MD loading, the average plastic deformation rate of the $(100)[010]$ transverse slip system is relatively small, which confirms the negligible influence of the ξ^3 parameter on the macroscopic behaviour. Only the $(100)[001]$ slip system is significantly active. Another useful observation is that the average plastic deformation rate of the amorphous phase decreases with time. In the case of TD loading, the plastic deformation rate of the amorphous phase is highest. There is a region where only the $(100)[001]$ slip system is active, however, in contrast to MD loading, there is a maximum followed by a decrease of the activity of this slip system. At a certain deformation, the $(100)[010]$ transverse slip is activated with a higher deformation rate compared to the other slip system.

Previously, it was shown that in the case of compression of isotropic PET, such a model demonstrated a good match of the texture evolution with experiments (see chapter 3). Here, the texture evolution of the oriented material is analysed. It is shown in figure 4.17 and is found to depend
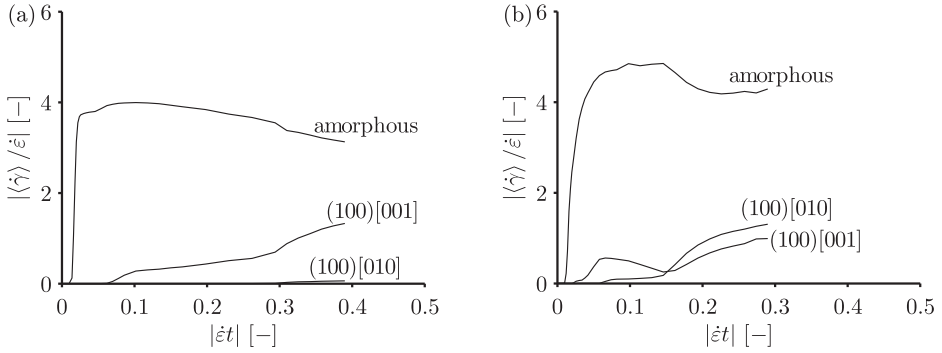
Figure 4.16: Evolution of the average plastic deformation with time predicted by the model for the amorphous phase and 2 slip systems (the deformation rate of the third slip system is significantly smaller and is not shown) for loading in MD (a) and TD (b).

strongly on loading conditions. In both loading cases, the inclusion interface normal $\vec{n}^{\mathrm{I}}$ is moving away from the loading direction. Thus, inclusions tend to be aligned such that the crystalline and non-crystalline phase are connected in a parallel way with respect to the loading direction. The chain directions are also moving away from the loading direction, which in the case of TD loading means that the relatively wide spots in the [001] pole figure become narrow and the chains become mostly oriented in $\vec{e}_2$ direction. In the case of MD loading, this implies that spots in the [001] pole figure only become wider and are moving towards the centre of the pole figure. This is the opposite of what is usually observed in polymer drawing, where chains are aligning with the stretching direction. This can be explained by considering an inclusion with its (100) plane parallel to the film surface (spanned by $\vec{e}_1$, $\vec{e}_2$) and with its [001] direction parallel to $\vec{e}_2$, which is loaded in MD. Depending on the constitutive behaviour of the separate phases, the chain direction either stays aligned with MD or deviates from it. The anisotropy of the crystalline phase may limit its shear mobility, resulting in a higher shear rate in the non-crystalline phase, which leads to the rotation of the crystalline phase, i.e. movement of the chain direction away from the loading direction. Similar conclusions are valid for the evolution of normals to the (001) plane with time. A more thorough investigation of the stability of the alignment of [001] with the loading direction requires the incorporation of the elastic anisotropy of the non-crystalline phase and its inhomogeneity in the region close to the crystal.

4.7   Modelling long-term behaviour

To describe the long-term macroscopic behaviour of the semicrystalline material, an appropriate number of viscoelastic Maxwell elements with timescales representing the experimental timescale should be used, i.e. a single mode model used for the simulation of the short-term behaviour is insufficient to describe creep up to $t = 10^{11}$ s. To fit the relaxation spectrum, the master curves constructed at $T = 50\,°C$ were taken. Ageing kinetics was not taken into account and a simulation of the tensile creep of an unageing sample was performed. As discussed in section 4.5 the
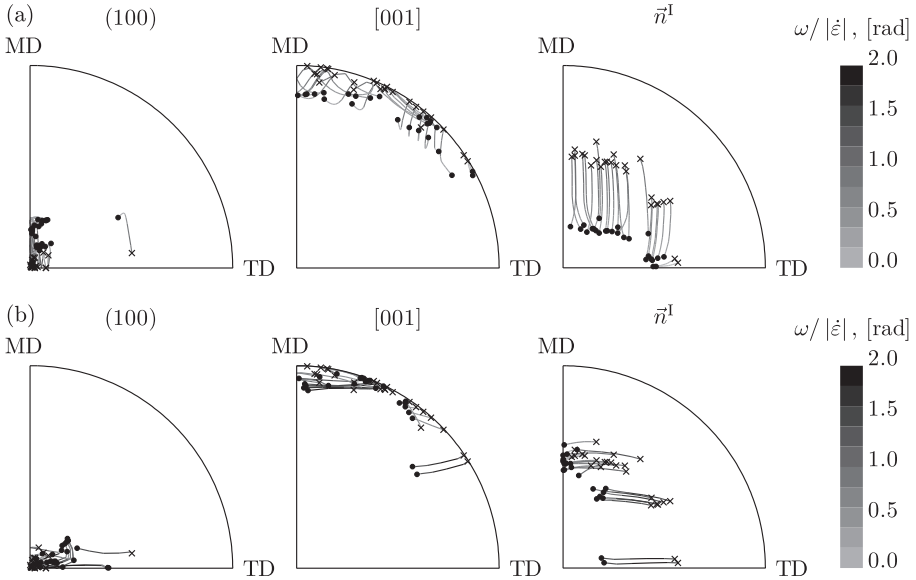
Figure 4.17: Equal area projection pole figures showing various crystallographic orientations (normal to the (100) plane and the $[001]$ direction) and the normal to the inclusion interface ($\vec{n}^{\mathrm{I}}$) with their trajectories during loading. Initial positions are shown with symbols $\times$, final positions with symbols $\bullet$. Colours indicate the angular velocity normalised by $|\dot{\varepsilon}|$. The material is loaded in MD (a) and TD (b). Due to symmetry of the set of inclusions with respect to MD and TD, and thereby symmetry of the pole figures, only quarters of the pole figures are shown.

master curves correspond to the response of the samples in a particular thermomechanical state. For samples with a different physical age, the compliance curves are shifted horizontally. This effect of transition in the thermomechanical state is accounted for in the model by a shift of the relaxation spectrum, i.e. by changing the parameter S_{a}. Since here only one set of master curves is used (samples were cut at different directions but from the same film) S_{a} was taken to be 0.

Ideally, the relaxation spectrum of the non-crystalline phase should be fitted separately, excluding the effect of the crystalline phase. However, as has already been discussed, the properties of the non-crystalline phase of semicrystalline PET and fully amorphous PET may be different, and the behaviour of semicrystalline material is determined directly. Using a gradient descent method, the pre-deformed state of the non-crystalline phase and the relaxation spectrum were determined. Relaxation times were fixed and both master curves (corresponding to creep in TD and MD) were used to identify shear moduli G_i^{a}, i.e. one relaxation spectrum of the non-crystalline phase was used to simulate both the MD and TD behaviour. The results are shown in figure 4.18a, where an adequate match of the experimentally measured creep compliance and the simulated one can be observed.

Without incorporating the anisotropy of the non-crystalline phase (by pre-deforming the hardening element), a completely different behaviour was observed. In figure 4.18a, the results with an isotropic non-crystalline phase (pre-deformation stretch ratio $\lambda_{\mathrm{d}} = 1$) are shown in grey. Qualitatively different behaviour was observed, with a higher compliance for MD than for TD loading, that
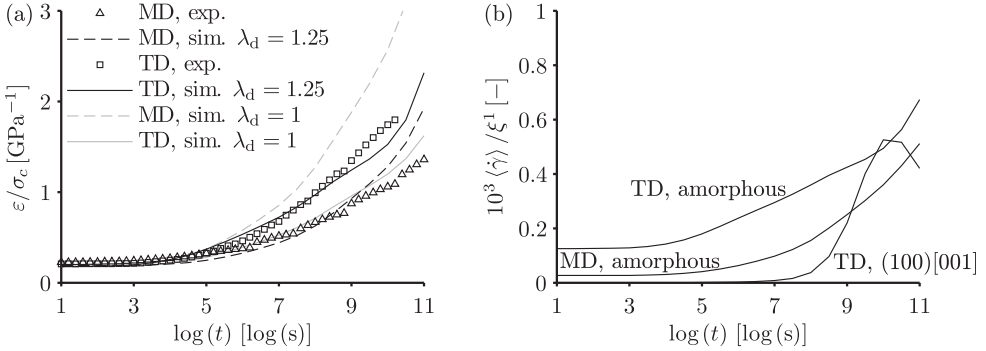
Figure 4.18: Dependence of the creep compliance of oriented PET on time for different loading directions (a), comparison of the simulations (line) with the measurements (symbols); model prediction of the evolution of the average plastic deformation rate of the amorphous phase and the $(100)[001]$ slip system (only the case of TD loading is shown; in the case of MD loading, the plastic deformation rate of the $(100)[001]$ slip system is significantly lower) with time for different loading conditions (b).

is, the opposite of what was observed experimentally. In the case of isotropic non-crystalline phase it was not possible to obtain a reliable creep compliance matching by fitting parameters G_i^a. Therefore, it was concluded that the incorporation of the effect of the anisotropy of the non-crystalline phase is essential to obtain a realistic macroscopic response.

Almost no texture evolution was observed during the creep simulation since the deformation stayed below 1.5%. As seen in figure 4.18b, the contribution to plastic deformation comes mostly from the non-crystalline phase in contrast to the case when isotropic material (with crystallinity of 0.25) was subjected to creep (see chapter 3). In the latter case, the average plastic shear rate on the $(100)[001]$ chain slip system was higher than the average shear rate of the amorphous phase. Apparently, in the case of oriented material loaded either in TD or MD, due to the orientations of slip planes and slip directions, slip systems are less active, which leaves almost only the contribution of the non-crystalline phase.

4.8   Conclusions

In this work, experimental characterisation and numerical modelling of biaxially oriented PET film using a multiscale approach was performed. Macroscopic characterisation of the PET film revealed the anisotropy as well as inhomogeneities in the film. Across the length (MD), the measured variation of the macroscopic properties was insignificant. From macroscopic results, the conclusion can be made that the underlying orientation of the crystalline phase is symmetric with respect to the centre and that the MD and TD directions in the centre demonstrated two extreme behaviours. Therefore, simulations were focused on these loading cases, whereby the influence of the underlying structure is investigated with the help of multiscale modelling. Parameter identification was performed and it was shown that the macroscopic behaviour qualitatively matched the experimen-

tally measured response, meanwhile in the case of isotropic PET, such a model demonstrated some mismatch at high crystallinity. Even though in the case of anisotropic material the influence of slip systems is separated in MD and TD, the parameter values might still be non-unique.

It was shown that properties of the non-crystalline phase in oriented material differ significantly from the properties of the purely amorphous material due to the constraints of the neighbouring crystalline phase and the presence of tie molecules. It was possible to simulate the macroscopic behaviour of the oriented material with an increased viscosity of the non-crystalline phase compared to the viscosity of the amorphous material obtained in a previous chapter, i.e. by a shift of the relaxation spectrum to longer relaxation times. Therefore, the relaxation spectrum obtained here represents the behaviour of the constrained non-crystalline phase and cannot be directly used for the simulation of purely amorphous material.

It was observed that in the case of tensile strain controlled simulations, texture evolution is somewhat different than what is commonly observed during film stretching. The influence of the anisotropy of the non-crystalline phase and the simulation of the macroscopic behaviour taking this effect into account were discussed. In the case of tensile creep simulations, it was observed that with the same relaxation spectrum for the non-crystalline phase, simulations of the behaviour in both the MD and TD directions can be performed and are highly sensitive to the pre-deformed state of the non-crystalline phase. Therefore, especially for creep applications, the non-crystalline anisotropy is significant, although there are other important effects, such as ageing during the test. The simulation of the latter effect is a possible future extension of the model by incorporation of the evolution of the parameter S_a during long-term testing, which would capture the effect of decreasing creep rate as the material thermodynamic state changes.

In semicrystalline material, an intermediate phase exists close to the crystalline layers. The anisotropy of this intermediate phase is the result of molecular orientation close to the crystalline phase and is physically different from the anisotropy of the non-crystalline phase, which was modelled here and is a result of the film drawing process. Such inhomogeneity can be simulated using three-phase layered domains as structural units of the microstructure. This approach was applied to HDPE [77] using the composite inclusion model and to PET [53] using other micromechanical models, such as a self-consistent model, for the domain interaction. In both cases, the elastic behaviour was considered.

Even though there are some limitations, by using the composite inclusion model, the influence of the material structure on the macroscopic properties can be adequately investigated. Additional numerical investigations of inclusion stability during loading and phase interaction are required for precise characterisation of texture evolution.

4.A   Appendix: model parameters

The stiffness matrix of the PET crystal is temperature dependent. In the model, the values interpolated at a particular temperature are used [25]. Here only the values at an ambient temperature (300 K) are listed in table 4.1, where the Voigt notation (11, 22, 33, 23, 31, 12) is used (the coordinate system $\vec{i}_1 \vec{i}_2 \vec{i}_3$ coupled to the crystal is explained in section 4.4). For the crystalline phase, there are two parameters determining viscoplastic deformation on a separate slip system. For all slip systems the reference shear stress is $\tau_0^\alpha = 1.1\,\mathrm{MPa}$ and the reference shear rates are $\xi^1 = 10^{-16}\,\mathrm{s}^{-1}$, $\xi^2 = 10^{-80}\,\mathrm{s}^{-1}$ and $\xi^3 = 10^{-30}\,\mathrm{s}^{-1}$ for the $(100)[001]$, $(010)[001]$ and $(100)[010]$ slip systems, respectively.

Table 4.1: Components of the stiffness matrix of the PET crystal at 300 K.

parameter	C_{11}^{c}	C_{22}^{c}	C_{33}^{c}	C_{44}^{c}	C_{55}^{c}	C_{66}^{c}	C_{12}^{c}	C_{13}^{c}	C_{23}^{c}
value [GPa]	14.4	17.3	178.0	6.6	1.4	1.2	6.4	3.4	9.5

parameter	C_{14}^{c}	C_{24}^{c}	C_{34}^{c}	C_{15}^{c}	C_{25}^{c}	C_{35}^{c}	C_{45}^{c}
value [GPa]	-2.2	3.3	3.8	-0.3	-0.5	-0.7	0.2

parameter	C_{16}^{c}	C_{26}^{c}	C_{36}^{c}	C_{46}^{c}	C_{56}^{c}
value [GPa]	-1.8	0.5	-1.8	-0.4	0.0

Table 4.2: Model parameters for PET, non-crystalline phase, short-term behaviour.

parameter	ΔU [kJ/mol]	V^{*} [nm^{3}]	G_{r} [MPa]	T_{r} [K]	K^{a} [MPa]	μ [$-$]
value	230	3.24	4.7	296	1800	0.048

parameter	G_{1}^{a} [MPa]	τ_{01r} [s]	r_{0} [$-$]	r_{1} [$-$]	r_{2} [$-$]	S_{a} [$-$]
value	813	$3.1 \cdot 10^{13}$	0.95	5	-9	0

Table 4.3: Model parameters for PET, non-crystalline phase, long-term behaviour, relaxation spectrum.

parameter	ΔU [kJ/mol]	V^{*} [nm^{3}]	G_{r} [MPa]	T_{r} [K]	K^{a} [MPa]	μ [$-$]			
value	230	3.24	4.7	323	1800	0.048			
parameter	τ_{01r}	τ_{02r}	τ_{03r}	τ_{04r}	τ_{05r}	τ_{06r}	τ_{07r}	τ_{08r}	τ_{09r}	τ_{010r}
value [s]	10^{12}	10^{11}	10^{10}	10^{9}	10^{8}	10^{7}	10^{6}	10^{5}	10^{4}	10^{3}
parameter	G_{1}^{a}	G_{2}^{a}	G_{3}^{a}	G_{4}^{a}	G_{5}^{a}	G_{6}^{a}	G_{7}^{a}	G_{8}^{a}	G_{9}^{a}	G_{10}^{a}
value [MPa]	8	13	12	16	50	53	102	257	274	28

For the amorphous phase, a different number of modes is used for the short-term behaviour than for the long-term behaviour, since for creep simulations across the large timescale a small amount of modes is insufficient. For the short-term strain controlled tests, a large number of modes is not necessary and is computationally inefficient; details are provided in the main text. Values of the parameters can be found in table 4.2 and table 4.3. Relaxation times for the rejuvenated state are listed instead of the viscosities:

$$\tau_{0ir} = \frac{\eta_{0ir}}{G_{i}^{a}}, \tag{A1}$$

where symbol τ is used for the relaxation time of the mode and not for the equivalent stress as in the model description.
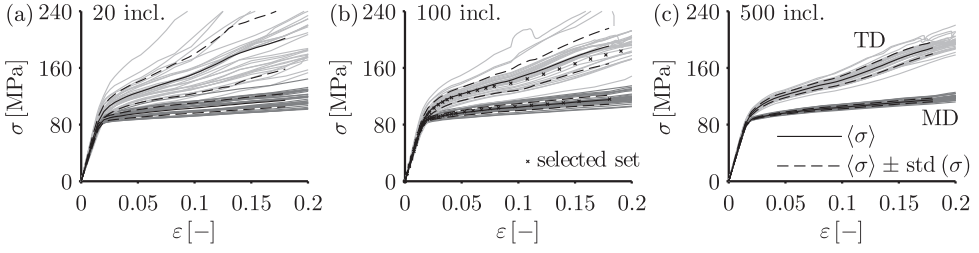
Figure 4.19: True stress-true strain response in MD and TD for each of 30 aggregates, average true stress-true strain response and standard deviation bandwidth for different aggregate sizes. The response of the aggregate used in the current work is shown in figure (b).
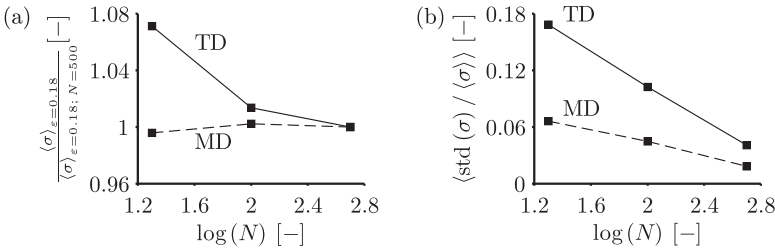

Figure 4.20: Dependence of average stress at strain $\varepsilon = 0.18$ on aggregate size, normalised by value for $N = 500$ (a); dependence of strain-average normalised standard deviation on aggregate size (b).

4.B   Appendix: influence of aggregate size

To study the influence of aggregate size on the mechanical behaviour, the response was calculated for aggregates with $N = 20$, 100 and 500 inclusions. To preserve TD, MD and ND ($\vec{e}_1, \vec{e}_2, \vec{e}_3$) as the principal directions even for small set sizes (as observed for real material) each set is generated by first generating a subset of $N/4$ inclusions. Subsequently, three copies of this subset are created and each is rotated by $180°$ around $\vec{e}_1, \vec{e}_2$ and $\vec{e}_3$, respectively. These subsets are then combined in a set of size N with the desired symmetry, thus enforcing TD, MD and ND to be the principal directions. For each selected aggregate size, 30 aggregates were generated and their strain-rate-controlled mechanical behaviour in TD and MD was simulated with an imposed strain rate of $\dot{\varepsilon} = 10^{-3}\,\mathrm{s}^{-1}$, see figure 4.19. For each strain value the standard deviation of the stress, $\mathrm{std}\,(\sigma)$, was found to decrease with aggregate size.

The dependence of the average stress at strain $\varepsilon = 0.18$ on the aggregate size is shown in figure 4.20a. The average over all of the strain values of the normalised standard deviation was found to be linearly dependent on the logarithm of the aggregate size, figure 4.20b. Based on the demonstrated convergence, the aggregate size of $N = 100$ was selected. The mechanical behaviour of the generated set of inclusions, which was used for the simulations in the current work, is compared to the average response in figure 4.19b (note that here the true stress-strain response is shown, in contrast

to section 4.6, where the engineering stress-strain response was considered).

5 Reversible and irreversible thermo-mechanical deformation of oriented PET film*

Abstract: In this chapter, the reversible and irreversible thermo-mechanical time-dependent deformation of oriented polyethylene terephthalate film is studied. A mean-field model is used to simulate these effects along with the long-term creep behaviour, taking into account the underlying material microstructure and differences in constitutive behaviour of the phases. The material is modelled as an aggregate of layered two-phase domains. Irreversible deformation, or partial shape recovery, results from the presence of an internal stress, which is characterised and incorporated into the constitutive behaviour of the non-crystalline phase. Using the micromechanical approach, the deformation mechanisms at the local scale are analysed.

5.1 Introduction

Predictable mechanical response and high dimensional stability are major requirements for polymer substrates used in the production of flexible electronics [2, 5]. There are a number of candidates for the substrate material with the most common materials being semicrystalline, oriented and thermally stabilised polyethylene terephthalate (PET) and polyethylene naphthalate (PEN) films. The goal of this work is to predict the dimensional stability of the polymer film at temperatures above the glass transition temperature, i.e. to simulate reversible and irreversible deformation of the film under these industrially relevant conditions based on the underlying microstructural information.

The polymer films studied here are produced by sequential biaxial stretching at temperatures above the glass transition (T_g) and subsequent cooling down to room temperature [108]. Upon heating above T_g these films demonstrate irreversible deformation under stress-free conditions, referred to as thermal shrinkage, or an emergence of shrinkage stress if the dimensions are fixed [118–120]. This process is significantly influenced by the manufacturing conditions [121]. Such behaviour can be classified as a shape-memory effect, where the partial recovery of the original shape is a result of increased molecular mobility above T_g and the driving force is due to the tendency of the structure to increase its entropy by relaxing the oriented conformation [122]. In oriented amor-

---

*This chapter is partly reproduced from [117].

phous PET there is evidence that the molecular origin of this process lies in a redistribution of the rotational isomers along the polymer chains, leading to their coiling [123].

The modelling approaches of shape-memory polymers can roughly be divided into macroscopic and micromechanical [122, 124]. In macroscopic models, the material behaviour is simulated as the behaviour of a system constructed of elastic, viscous and purely plastic elements. In this case, a non-linear temperature-dependent viscosity captures the shape memory effect. In contrast, micromechanical approaches take into account aspects of the material microstructure, while often lacking some reliable experimental data at that fine scale. In [125], the material was considered to consist of active and frozen phases with the phase transition being described by a temperature dependent volume fraction. A similar approach was used in [126] to construct a large deformation model based on the rules of mixtures. In [127], a model for semicrystalline shape-memory polymers was presented, where the shape-memory effect occurred due to a tendency of each phase to return to its initial configuration.

In this chapter, the effect of shape recovery of a PET film is modelled using a micromechanical model referred to as the composite inclusion model [73, 74, 81, 83]. In this model, the material is considered to consist of two phases: the crystalline and the amorphous phases, out of which layered domains are constructed. Here, the amorphous phase is referred to as non-crystalline since it significantly differs from purely amorphous material due to the constraints induced by crystalline lamellae and the presence of tie molecules. The material behaviour is modelled as the behaviour of an aggregate of such layered domains. Crystal plasticity [98] is used as a constitutive model for the crystalline phase, with viscous slip on the (limited number of) slip systems. The non-crystalline phase can be modelled with one of the material models suitable for glassy polymers, such as the model by Buckley et al. [37, 38], by Boyce et al. [39, 40] and by Govaert et al. [41, 42]. Here the model by Govaert et al., referred to as the EGP model, is used.

In [128], the composite inclusion model was used to describe the deformation kinetics of oriented HDPE. However, the model was found to lack the contribution of the pre-stretched amorphous phase. In chapter 4, this model was used to simulate short-term and long-term behaviour of the oriented PET film taking into account this pre-orientation. In the present chapter, the constitutive models of the phases are further extended, i.e. thermal expansion is added to the model and a relaxation of the internal pre-stress state of the PET film is incorporated to simulate the behaviour of the film at high temperatures and to model reversible and irreversible thermal deformation. The aim of this work is to simulate these effects based on the underlying microstructure, and therefore to obtain a reliable structure-property relationship and to analyse microstructural deformation processes.

5.2   Experimental methods

Thermally stabilised oriented PET film, manufactured by DuPont Teijin Films, was provided for the experimental analysis. The film is produced by sequential biaxial stretching with draw ratios $\lambda = 3.0$–3.5 in machine direction (MD) and transverse direction (TD), an average thickness of $125\,\mu\text{m}$, a width of $90\,\text{cm}$ and an approximate crystallinity of 50%.

To measure irreversible deformation of the film resulting from different heating conditions, the behaviour of oriented PET film was measured using two different techniques. In-situ strain measurements at varying temperatures were performed under uniaxial tensile stress-controlled conditions using a Zwick Z010 universal tensile tester equipped with a video extensometer, a temperature

controlled chamber and a 1 kN force cell. Samples, with a shape according to ISO 527-2, type 1BA, cut in different directions were heated from 60 °C to 190 °C with subsequent annealing at 190 °C. Three heating rates were imposed: constant rates of 1 °C/min, 5 °C/min and $\sim$ 10 °C/min, which is the maximum heating rate of the temperature controlled chamber. Measurements were performed under imposed stress of 0.16 MPa, which is sufficient to keep the sample straight while not leading to noticeable creep effects at high temperatures. Prior to testing, the samples were dried in the temperature controlled chamber at 60 °C for 60 min to prevent interference of hygroscopic expansion with the measurements. For the samples heated at 10 °C/min and 5 °C/min, multiple measurements were performed to ensure reproducibility.

The residual (i.e. irreversible) deformation after cooling down was measured using digital image correlation (DIC). Dried samples with dimensions of 15 cm by 10 cm (in TD and MD, respectively) with a grid of 16×11 dots were placed in a pre-heated oven and annealed for a certain time. Images of samples were taken before the heat treatment and after removing the sample from the oven and cooling it down to room temperature, thus eliminating reversible thermal deformation (thermal expansion). The two-dimensional strain was extracted from the images by correlating the displacement of the dots across the series of images. A uniform strain field in each sample was assumed, since the strain inhomogeneity within one sample was of the same order of magnitude as the deviation of the average strain within multiple samples tested at identical conditions. The actual calculated strain in each sample tested at certain conditions was averaged from three subsequently taken images. Since heating and annealing of the samples was performed at stress-free conditions, film wrinkling, resulting from inhomogeneity of the sample and of the temperature field, was observed. Therefore, when images of the samples were recorded, the samples were straightened by putting a glass plate on top.

The anisotropy and inhomogeneity of the film was studied in previous chapter. It was found that for the centre of the film (i.e. the middle position across the width) the principal strain directions correspond to MD and TD and for the sides the principal directions are rotated by 15°. Therefore the effective MD and TD, which are rotated by a small angle, are introduced here for the right part of the film. In chapter 4, the mechanical behaviour along the effective directions was found to be similar across the width of the film. Therefore, here samples from the sides of the film were also used for the experimental programme with strain measurements performed along the effective machine and transverse directions.

To measure the coefficient of thermal expansion (CTE) of isotropic PET, semicrystalline PET samples were prepared from amorphous PET, which was also supplied by DuPont Teijin Films, by annealing in an oven for 1, 4, 10 and 13 hours at 100 °C. Crystallinity of the samples was measured by X-ray diffraction and DSC. To determine the CTE, PET samples were heated from 30 °C to 70 °C and then cooled down to 30 °C at a rate of 5 °C/min. The cycle was repeated 2 times, and the obtained measurements of the CTE during heating and cooling were averaged. The deformation field was obtained by DIC. The observed deformation of the samples was homogeneous and linearly dependent on temperature within the imposed temperature region.

The CTE of the oriented PET film was measured using the same technique as used to measure the CTE of isotropic PET, however during the heating stage of the first cycle, strain was not recorded, and thus only 3 measurements (2 during cooling and 1 during heating) were taken. Measurements on 3 samples from the centre of the film were performed and the results were averaged.
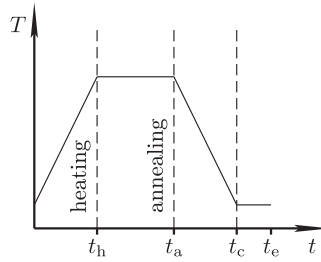
Figure 5.1: Schematic representation of the imposed temperature profile.

5.3　Measurements, oriented material

The thermomechanical behaviour of PET film under different conditions was studied. The imposed temperature profile is illustrated in figure 5.1. In the first case, the strain evolution during only the "heating" and "annealing" stages is considered with an imposed heating rate of 1–$10\,^{\circ}\mathrm{C/min}$. In the second case, only irreversible deformation due to the imposed temperature history is considered, i.e. only the strain value at $t = t_{\mathrm{e}}$ and its dependence on parameters of the temperature profile (the annealing temperature and the annealing time). As described in section 5.2, for the second case, samples were placed in a preheated oven, which resulted in almost instantaneous heating of the samples to the annealing temperature (in section 5.5.2, to model this case a heating rate of $17\,^{\circ}\mathrm{C/s}$ was used).

The heating stage and the annealing stage of the in-situ strain measurements are analysed separately. Measurements corresponding to a particular heating rate were reproducible with the absolute strain deviation between several samples not exceeding $2.5 \cdot 10^{-3}$. In figure 5.2, the effect of heating rate on the measured strain is demonstrated. It is obvious that the deformation due to heating is anisotropic with TD expanding and MD shrinking at lower temperatures. At higher temperatures, TD also shows shrinkage with a faster deformation rate than for MD. Although for TD samples, the influence of the heating rate on strain is comparable to experimental scatter, for MD it is noticeably larger. Using this measuring method, only combined reversible and irreversible deformations are obtained.

To analyse only irreversible deformations, the permanent strain resulting from fast heating of the sample in the oven was obtained with digital image correlation after cooling the sample. The influence of annealing temperature and annealing time was investigated. In figure 5.3, the measured strain and its dependence on annealing time (the time-dependent nature of the thermal irreversible deformation) and annealing temperature for the samples in effective MD and TD is shown. Comparing figures 5.2 and 5.3, it can again be seen that the heating rate influences the residual shrinkage strain with approximately doubled strain values for the case when samples are placed in a preheated oven. The reason for this is internal relaxation taking place in the material during slow heating, which does not lead to a macroscopic deformation, as well as the absence of reversible thermal deformation (thermal expansion) in the results shown in figure 5.3.

The maximum absolute value of the deviation of the shear strain from zero is $3 \cdot 10^{-3}$, i.e. the principal directions of the strain tensor deviate only slightly from the previously measured 15° at the sides of the film. This small deviation changes with annealing temperature: the shear strain is
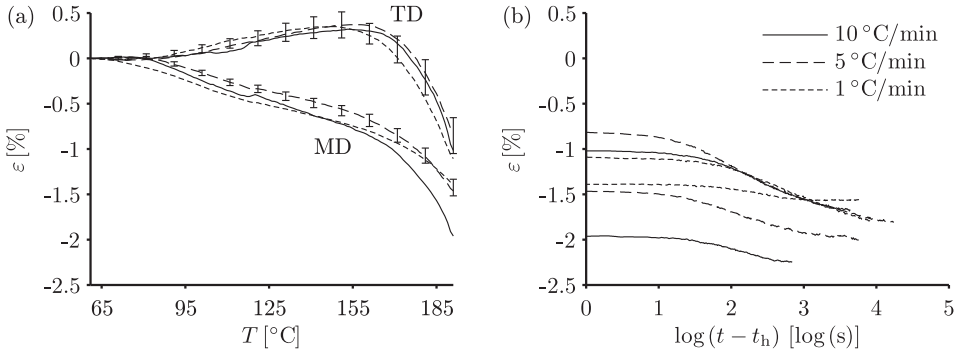
Figure 5.2: Dependence of strain on temperature for MD and TD samples during heating at heating rates of 1–$10\,°\text{C/min}$ (a) and evolution of strain with time during annealing at $190\,°\text{C}$ starting from the point of reaching the annealing temperature (b). For the heating rate of $5\,°\text{C/min}$, error bars indicating a 95% confidence interval are shown, where experimental scatter results from 9 measurements per direction (MD and TD).
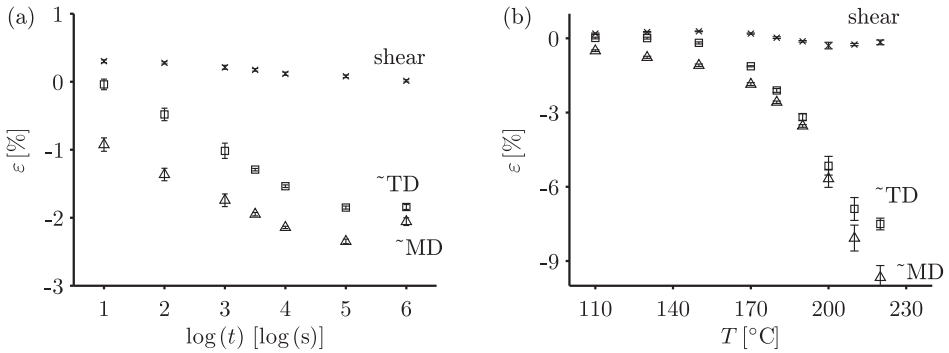

Figure 5.3: Dependence of the residual strain in effective directions on the annealing time at $170\,°\text{C}$ (a), dependence on annealing temperature, measured after annealing for $10^3\,\text{s}$ (b). The right part of the film was used. Error bars indicate a 95% confidence interval, where experimental scatter results from measurements performed on 3 different samples and 3 images taken per sample per measurement.

positive for temperatures below $180\,°\text{C}$ and negative above this value.

5.4 Micromechanical modelling

The material behaviour is modelled at multiple scales using the composite inclusion model [83]. A detailed model description can be found in section 3.A. The macroscopic scale corresponds to a material point, where the Cauchy stress tensor $\boldsymbol{\sigma}^\text{M}$ and the deformation gradient tensor $\boldsymbol{F}^\text{M}$ are
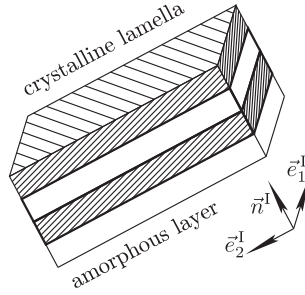
Figure 5.4: The two-layer composite inclusion after [74, 83]. The structural unit of the model is highlighted in a stack of crystalline lamellae.

volume averaged quantities of the two-phase layered microstructure, which consists of multiple differently oriented layered domains, each consisting of different phases, see figure 5.4. The two-phase domains are referred to as composite inclusions [74]. Each phase in a domain is described with its representative constitutive law and has homogeneous stress and deformation fields. Compatibility and equilibrium conditions are enforced at the interface between the phases:

$$\sigma_{n3}^{ck} = \sigma_{n3}^{ak}; \quad F_{ns}^{ck} = F_{ns}^{ak}; \quad k = \overline{1, N}; \quad n = \{1, 2, 3\}; \quad s = \{1, 2\}, \tag{5.1}$$

where components are taken with respect to the inclusion coordinate system shown in figure 5.4 (with unit vectors $\vec{e}_1^{\,\mathrm{I}}, \vec{e}_2^{\,\mathrm{I}}, \vec{e}_3^{\,\mathrm{I}} = \vec{n}^{\,\mathrm{I}}$). Superscripts "c", "a" indicate quantities belonging to crystalline and non-crystalline phases and N is the number of layered domains. The average stress tensor $\boldsymbol{\sigma}^{\mathrm{I}}$ and deformation gradient tensor $\boldsymbol{F}^{\mathrm{I}}$ of each layered domain are obtained by volume averaging. The domains are coupled using a mean-field interaction law [74, 83]: the components of the inclusion-averaged stress and deformation gradient tensors that are not constrained by intra-inclusion equilibrium and compatibility conditions, are equal to their corresponding macroscopic quantities. Macroscopic quantities $\boldsymbol{F}^{\mathrm{M}}$ and $\boldsymbol{\sigma}^{\mathrm{M}}$ are obtained by volume averaging the inclusion-averaged quantities $\boldsymbol{\sigma}^{\mathrm{I}}$ and $\boldsymbol{F}^{\mathrm{I}}$. The semicrystalline morphology is then characterised by the orientation distribution of the crystalline phases and interfaces between the crystalline and the non-crystalline phase.

Here, simulations of isotropic and oriented material are performed. The difference in model behaviour results from the orientation differences of the layered domains, which is illustrated in the equal area projection pole figures in figure 5.5, where the crystal orientations as well as the orientations of interface normals are shown. For the isotropic material, a set of uniform random orientations is adopted. For the oriented material, the orientation distribution in the PET film was characterised in previous chapter. For the isotropic case 125 inclusions were used, and for the oriented case 100 inclusions were used. Another difference is the incorporation of anisotropic internal stresses in the non-crystalline phase for the oriented material, whereas a stress-free non-crystalline phase is used for the isotropic material, as further elaborated in the following section. This addition was required to accurately model the differences between the long-term creep responses in MD and TD directions (see previous chapter).
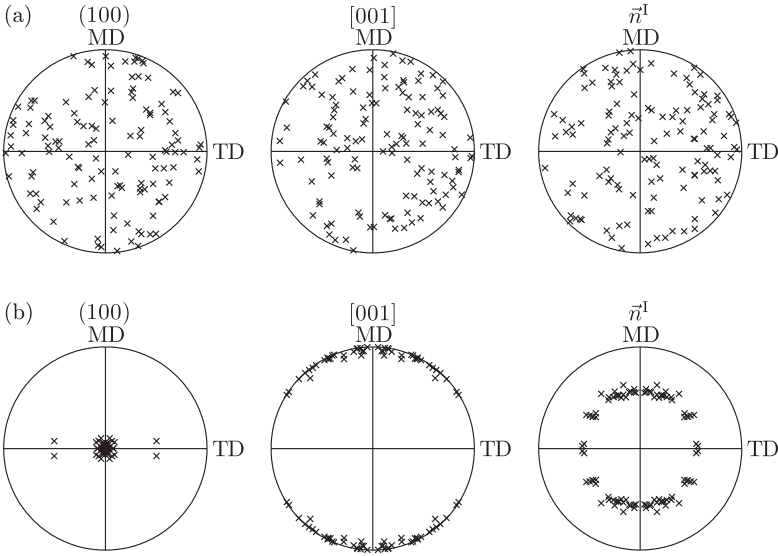
Figure 5.5: Equal area projection pole figures showing the initial crystallographic orientations (normal to the (100) plane and the [001] direction) and the normal to the interface between phases ($\vec{n}^{\mathrm{I}}$) for isotropic material (a) and oriented material (b). The orientation set in (b) is taken from chapter 4.

5.4.1 Constitutive behaviour of the phases

A multiplicative decomposition of the deformation gradient tensor into an elastic (e), thermal (t) and plastic (p) part is used for both phases: $\boldsymbol{F} = \boldsymbol{F}_{\mathrm{e}} \cdot \boldsymbol{F}_{\mathrm{t}} \cdot \boldsymbol{F}_{\mathrm{p}}$ [129]. Thermal expansion was introduced for each phase, with anisotropic expansion for the crystalline phase and isotropic expansion for the non-crystalline phase. The thermal velocity gradient* is linearly dependent on the time derivative of the temperature through a tensor $\boldsymbol{\alpha}^{\nu}$ containing thermal expansion coefficients [130]:

$$\boldsymbol{L}_{\mathrm{t}}^{\nu} = \dot{\boldsymbol{F}}_{\mathrm{t}}^{\nu} \cdot \boldsymbol{F}_{\mathrm{t}}^{\nu-1} = \boldsymbol{\alpha}^{\nu} \dot{T}; \quad \nu = \mathrm{a,c}. \tag{5.2}$$

The non-crystalline phase is modelled with the Eindhoven Glassy Polymer (EGP) model [42, 46, 109], which consists of a combination of viscoelastic Maxwell elements with neo-Hookean-like elasticity and non-linear viscosity, which is temperature and stress dependent. This constitutive model is schematically illustrated in figure 5.6a, where for simplicity only two viscoelastic modes are illustrated. The stress dependency is described using the Eyring flow model and temperature dependency using the Arrhenius law. The viscosity depends on the equivalent stress τ, the pressure

---

*Equation (5.2) is numerically integrated in the following way:

$$\boldsymbol{F}_{\mathrm{t}}^{\mathrm{c}}\left(t_{n+1}\right) = \exp\left(\Delta t \boldsymbol{\alpha}^{\mathrm{c}}\left(t_{n+1}\right) \dot{T}\left(t_{n+1}\right)\right) \cdot \boldsymbol{F}_{\mathrm{t}}^{\mathrm{c}}\left(t_{n}\right).$$
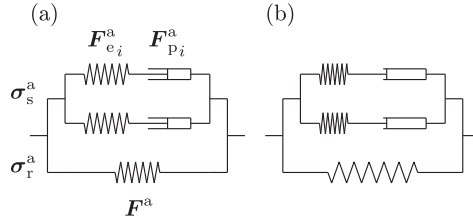
Figure 5.6: Schematic representation of the constitutive models used for the non-crystalline phase. Original EGP model formulation (a) and model with a pre-deformed initial state used in chapter 4 (b).

p^{a}, the temperature T and the thermomechanical history S:

$$\eta_i = \eta_{0ir} \exp\left(\frac{\Delta U}{R}\left(\frac{1}{T} - \frac{1}{T_{\mathrm{r}}}\right)\right) \frac{\tau/\tau_0}{\sinh\left(\tau/\tau_0\right)} \exp\left(\frac{\mu p^{\mathrm{a}}}{\tau_0}\right) \exp\left(S\right); \tag{5.3}$$

$$\tau_0 = \frac{kT}{V^*}, \tag{5.4}$$

where R is the universal gas constant, ΔU the activation energy, T_{r} a reference temperature, k is the Boltzmann constant and V^* the activation volume. Multiple molecular relaxation processes can be taken into account in this constitutive model by using different stress and temperature dependency parameters for viscoelastic modes. This model in combination with the composite inclusion model described above was used to simulate the large-strain mechanical behaviour of isotropic semicrystalline PET (chapter 3). To simulate the long-term and short-term behaviour of an oriented PET film (chapter 4), an internal pre-stress in the elastic elements describing the molecular network was included. These elastic elements are initially in a pre-deformed state (tension in MD and compression in TD), see figure 5.6b, thus introducing anisotropic yielding of the viscoplastic elements with isotropic behaviour in the elastic regime. The deformation gradient tensor $\boldsymbol{F}_{\mathrm{r}}^{\mathrm{a}}$ corresponding to the molecular network is calculated from the total deformation gradient tensor $\boldsymbol{F}^{\mathrm{a}}$ of the non-crystalline phase:

$$\boldsymbol{F}_{\mathrm{r}}^{\mathrm{a}} = \boldsymbol{F}^{\mathrm{a}} \cdot \boldsymbol{F}_{\mathrm{d}}^{\mathrm{a}}, \tag{5.5}$$

where $\boldsymbol{F}_{\mathrm{d}}^{\mathrm{a}}$ is a deformation gradient tensor determining the initial pre-deformation of the network. Initial elastic and plastic deformation gradients are calculated such that stress equilibrium of the non-crystalline phase is maintained initially, $\boldsymbol{\sigma}^{\mathrm{a}}\left(t = 0\right) = \boldsymbol{0}$, whereby the deformation gradient tensor equals the identity tensor, i.e. $\boldsymbol{F}^{\mathrm{a}}\left(t = 0\right) = \boldsymbol{I}$. The original formulation of the EGP model is recovered if $\boldsymbol{F}_{\mathrm{d}}^{\mathrm{a}} = \boldsymbol{I}$. The following form of the pre-deformation state of the molecular network was used:

$$\boldsymbol{F}_{\mathrm{d}}^{\mathrm{a}} = \left(1/\lambda_{\mathrm{d}}\right)\vec{e}_1\vec{e}_1 + \lambda_{\mathrm{d}}\vec{e}_2\vec{e}_2 + \vec{e}_3\vec{e}_3, \tag{5.6}$$

with $\vec{e}_1$ corresponding to TD and $\vec{e}_2$ corresponding to MD. This internal stress state, which was included in chapter 4 to describe the anisotropic creep behaviour of oriented film, is the basic mechanism which causes irreversible thermal deformations. However, to describe dimensional stability at temperatures above T_{g}, as required here, several additional modifications are made.
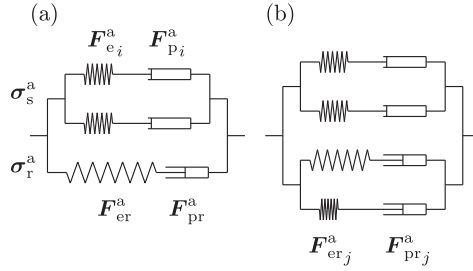
Figure 5.7: Schematic representation of the constitutive models used for the non-crystalline phase. Model extended with internal relaxation of the hardening stress (a) and model further extended with anisotropic pre-deformation (b).

In section 5.3, experimental results indicated that the heating rate influences residual irreversible deformation. This is included in the model by replacing the elastic hardening element in the EGP model by a viscoelastic element, see figure 5.7a, with a temperature dependent viscosity:

$$\eta_{\mathrm{r}} = \eta_{0\mathrm{r}} \exp\left(\frac{\Delta U_{\mathrm{r}}}{R}\left(\frac{1}{T} - \frac{1}{T_{\mathrm{r}}}\right)\right). \tag{5.7}$$

As such, a mechanism of stress relaxation during slow heating is incorporated, which leads to a lower irreversible shrinkage strain. A large relaxation time for the hardening elements is required such that these modes deform only elastically below T_{g}.

The crystalline phase is modelled with crystal viscoplasticity [98], where the deformation is decomposed into elastic and viscoplastic parts in addition to the thermal expansion. The elastic behaviour of the crystalline phase is anisotropic. The viscoplastic deformation is a superposition of shear deformations on a limited number of crystallographic slip systems with an Eyring flow equation relating shear rate and resolved shear stress [81].

Since the mechanism of irreversible thermal deformation (deformation driven by the presence of internal stresses due to the pre-stretched non-crystalline phase) is incorporated in the non-crystalline phase only, it elastically loads the crystalline phase during and after thermal deformation. If the crystalline phase deforms only elastically, it can subsequently deform the non-crystalline phase over longer time scales, such that the absolute value of the residual shrinkage strain is decreasing, i.e. the material is returning to its initial configuration, which is not experimentally observed. Therefore, a thermal dependence of the plastic slip has to be incorporated to increase the mobility of slip systems (decrease the time scale of plastic deformation), enabling plastic deformations in the crystalline phase at high temperatures. The following relation between shear stress τ^{α} and shear rate $\dot{\gamma}^{\alpha}$ on slip system α is used:

$$\dot{\gamma}^{\alpha} = \xi^{\alpha} \exp\left(\frac{\Delta U^{\alpha}}{R}\left(\frac{1}{T_{\mathrm{r}}} - \frac{1}{T}\right)\right) \sinh\frac{\tau^{\alpha}}{\tau_0^{\alpha}}, \tag{5.8}$$

where ΔU^{α} is the activation energy of the slip system, T the current temperature and T_{r} a reference temperature. A similar dependence of crystallographic slip on temperature was also included in a micromechanical model of HDPE in [81].
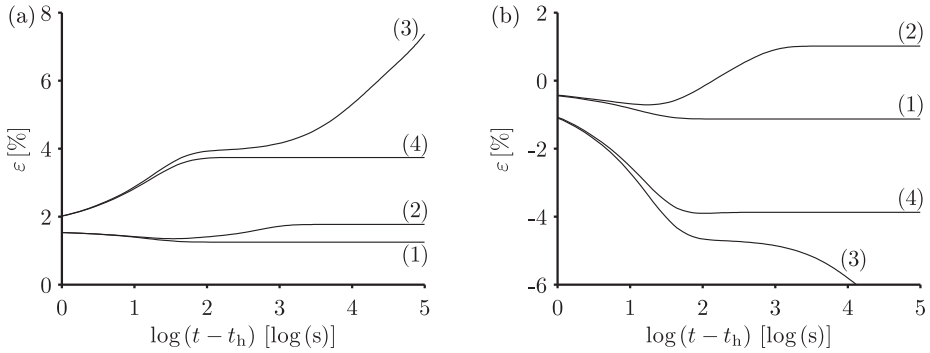
Figure 5.8: Composite inclusion model prediction of the evolution of strain with time during annealing at $T = 190\,°C$ after heating from $T_0 = 20\,°C$ with a heating rate of 17 $°C/s$ for TD (a) and MD (b). The model with a pre-deformed initial state of the non-crystalline phase (1), model extended with internal relaxation of the hardening stress in the non-crystalline phase (2), extended with temperature dependent slip systems in the crystalline phase (3) and extended with both modifications (4).

The influence of viscoelastic hardening of the non-crystalline phase and thermal dependence of the slip kinetics on the macroscopic behaviour obtained with the composite inclusion model is shown in figure 5.8, where the evolution of strain with time after reaching $T = 190\,°C$ is simulated. The heating stage ($t < t_h$) is not shown here. A uniaxial state of pre-deformation of the non-crystalline phase (as in chapter 4) is imposed, with $\lambda_d = 1.25$. Other model parameters are summarised in appendix 5.B. The following cases are compared:

(1) non-crystalline phase with elastic hardening;

(2) non-crystalline phase with internal relaxation of the hardening stress (with activation energy $\Delta U = 225\,kJ/mol$);

(3) crystalline phase with temperature dependent slip systems (parameters as in appendix 5.B);

(4) viscoelastic hardening and temperature dependent slip systems as in case (2) and (3), respectively.

The introduction of a temperature dependence of the slip systems significantly influences the deformation during annealing. Without allowing for relaxation of the internal hardening stresses of the non-crystalline phase, they drive the material to a state where the non-crystalline phase is stress-free, i.e. to a large strain determined by the pre-deformation. From a comparison of figures 5.2, 5.3 and 5.8 it can be seen that the simulated material behaviour is still not qualitatively matching the measurements. These observations indicate an anisotropic internal stress state, which constitutes the basis for further modifications.

Previously, it was shown that the non-crystalline phase of these films has a uniaxial internal stress state (see chapter 4). This was based on modelling the long-term behaviour of the film, in

Table 5.1: Pre-deformation parameters of the non-crystalline phase for oriented PET film.

parameter	$\lambda_{\mathrm{TD}1}\,[-]$	$\lambda_{\mathrm{MD}1}\,[-]$	$\lambda_{\mathrm{TD}2}\,[-]$	$\lambda_{\mathrm{MD}2}\,[-]$
value	1.37	0.93	0.39	1.74
parameter	$\Delta U_{\mathrm{r}1}\,[\mathrm{kJ/mol}]$	$\Delta U_{\mathrm{r}2}\,[\mathrm{kJ/mol}]$		
value	225	245		

correspondence with the experimentally observed behaviour. In section 5.3 it was shown that during heating to high temperatures, irreversible shrinkage deformation is observed in both directions, which indicates that at high temperatures the non-crystalline phase of the film demonstrates a biaxial internal stress state. At low temperatures, irreversible expansion in TD and irreversible shrinkage in MD were observed, indicating a uniaxial internal stress state at low temperatures. Therefore, to describe both effects, the viscoelastic hardening in the non-crystalline constitutive model was split into two modes with different activation energies and different pre-deformations:

$$\boldsymbol{F}_{\mathrm{d}j}^{\mathrm{a}} = \lambda_{\mathrm{TD}j}\vec{e}_1\vec{e}_1 + \lambda_{\mathrm{MD}j}\vec{e}_2\vec{e}_2 + \frac{1}{\lambda_{\mathrm{TD}j}\lambda_{\mathrm{MD}j}}\vec{e}_3\vec{e}_3, \quad j = \overline{1, N^{\mathrm{r}}}, \tag{5.9}$$

where $N^{\mathrm{r}} = 2$ is number of hardening modes. Pre-deformation ratios and activation energies for the hardening modes are summarised in table 5.1. Hardening moduli for these modes are equal (the full set of model parameters is given in appendix 5.B). For the adopted parameter set, both modes deform elastically at low temperatures and jointly reveal a uniaxial stress state as in chapter 4 (described by equation (5.6) with $\lambda_{\mathrm{d}} = 1.25$), allowing the simulation of anisotropic creep of the film. With increasing temperature, one of the modes undergoes relaxation while the other mode still contributes to the internal stress, thus describing a biaxial stress state leading to irreversible thermal shrinkage in both directions. This split is schematically illustrated in figure 5.7b. Note that the figure represents only one-dimensional analogues of the model, whereas in the full 3D model, the hardening stress $\boldsymbol{\sigma}_{\mathrm{r}}^{\mathrm{a}}$ is anisotropic. Values of the activation energies were identified from the experimental data (figures 5.2 and 5.3). A detailed model description can be found in section 5.A. Results of simulations using this constitutive model for the non-crystalline phase are compared in section 5.5.2.

5.5   Results

5.5.1   Characterisation of thermal expansion

The thermal expansion of the crystalline phase of PET is anisotropic due to the triclinic lattice structure of the PET unit cell, [25]. Thermal expansion coefficients of the crystalline phase, obtained by molecular modelling, were taken from [25] (parameters are listed in appendix 5.B). Thermal expansion of the non-crystalline phase was assumed to be isotropic, i.e. characterised by only one parameter $\alpha^{\mathrm{a}} = 7 \cdot 10^{-5}\,\mathrm{K}^{-1}$. A comparison of the CTE at various crystallinities obtained using the composite inclusion model (with an isotropic distribution of the layered domains) and measured CTEs is shown in figure 5.9. The micromechanical model qualitatively predicts the evolution
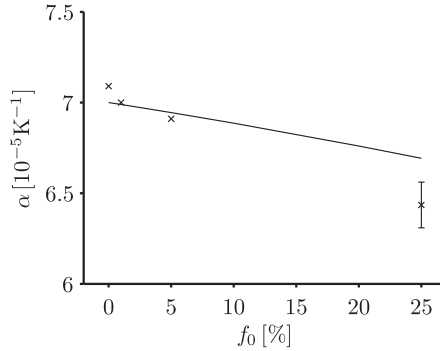
Figure 5.9: Dependence of macroscopic CTE of isotropic PET on crystallinity. Both experimental data (symbols) and model prediction (line) are shown. The error bar indicates a 95% confidence interval, where experimental scatter results from 4 measurements.

of the effective CTE of the isotropic material, although there is some quantitative deviation. For the isotropic material, the dependence of CTE on crystallinity is influenced by both the elastic and thermal properties of the phases. Elastic and thermal properties of the crystalline phase are obtained from molecular modelling and for the non-crystalline phase they are assumed to be isotropic and based on measurements on amorphous PET. Hence, the simulation is performed without any fitting parameters. In chapter 4, it was already shown that parameters of unconstrained and constrained amorphous material differ, with the latter being anisotropic. In the model, anisotropic yielding was included by including the internal stresses. However, the elastic and thermal expansion properties are still isotropic. Deviations of the model from experimental data is therefore attributed to the anisotropy of the elastic and thermal properties of the non-crystalline phase, for which no experimental data is available.

A comparison of the model prediction of the CTE and the measurements for oriented film is shown in table 5.2. The PET crystal has a negative CTE in the chain direction, i.e. the crystalline phase is contracting with increasing temperature in chain direction. Previous measurements show that MD is the dominant direction of the molecular chains in the crystalline domains of this PET film (see previous chapter). Therefore, for a high crystallinity of 50%, it is expected that the CTE in TD is higher than in MD, which is also predicted by the model but not observed experimentally. Furthermore, in [131], the mechanical behaviour as well as thermal behaviour of biaxially oriented PET film were measured and it was found that the direction corresponding to the largest hardening modulus demonstrated the lowest linear thermal expansion. For the PET film studied here, TD corresponds to the largest hardening modulus and the CTE in TD has the lowest value. For uniaxially oriented films, modelling concepts based on a combination of crystalline and amorphous phases and tie molecules give a reasonable prediction of linear expansion [132], whereby the CTE in drawing direction decreases with draw ratio and the CTE normal to the drawing direction increases with draw ratio. This result also corresponds to the behaviour of the composite inclusion model studied here, where the lower CTE in MD is a result of the dominant chain orientation in MD. The deviation observed here is most likely due to anisotropy of the non-crystalline phase, in particular, an anisotropic CTE and elastic properties, resulting from the biaxial drawing process.

Table 5.2: Macroscopic CTE below T_g of oriented PET film in different directions.

direction	TD	MD
measurement $\left[10^{-5}\mathrm{K}\right]$	2.2	4.3
model $\left[10^{-5}\mathrm{K}\right]$	5.4	3.0
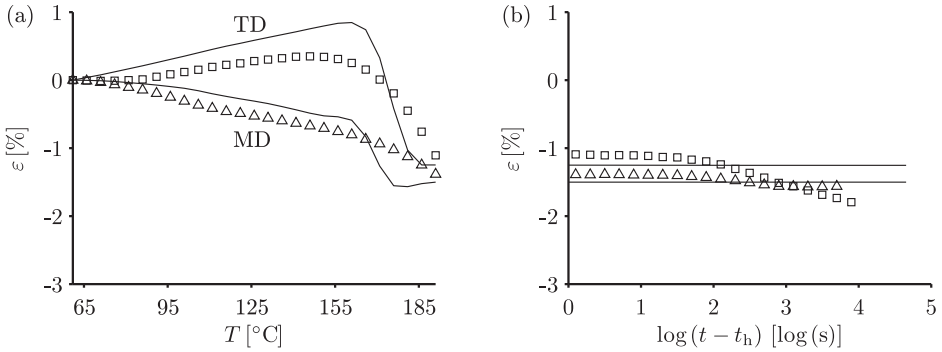
Figure 5.10: Dependence of strain on temperature during heating with a heating rate of $1\,^\circ\mathrm{C}/\mathrm{min}$ (a) and evolution of strain with time during annealing (b). Comparison of model results (solid lines) and measurements (symbols) for MD and TD.

5.5.2 Simulation of dimensional stability of oriented film

A comparison of simulation results and measurements for the case when both reversible and irreversible processes contribute to strain during thermal loading is shown in figure 5.10, which is split into two parts: "heating" and "annealing". The model qualitatively predicts the experimentally observed behaviour in the entire temperature range, whereby the deformation rates are even quantitatively captured in the region up to $160\,^\circ\mathrm{C}$. The fast change in deformation rate after $\sim 160\,^\circ\mathrm{C}$ in the simulated results is due to stress relaxation in the first viscoelastic hardening mode, whereby only the second mode remains active. A more smooth transition, as observed in the experiment, can be achieved with a larger number of viscoelastic hardening modes with different pre-deformation ratios and different relaxation times. Both viscoelastic hardening modes are active at low temperatures. Therefore the film demonstrates shrinkage in MD and expansion in TD, i.e. corresponding to a uniaxial internal stress state. After relaxation of the first mode, the remaining biaxial internal stress state leads to shrinkage deformation in both directions, resulting in both MD and TD deformations below -1%. The exact mechanism of transformation of the internal stress state is discussed in section 5.5.4. Due to a limited amount of viscoelastic modes (relaxation times), no subsequent deformation is observed during annealing at high temperatures. All modes already passed the relaxation process, which is not the case at lower temperatures, see figure 5.11.

The second case is fast heating with subsequent cooling. A comparison of simulation results and experimental data is shown in figure 5.12. As in the experiments, the line corresponding to the modelling results is based on strain values taken at $t = t_e$ from simulations with an imposed temperature profile as in figure 5.1, with varying holding time (figure 5.12a) and varying temperature
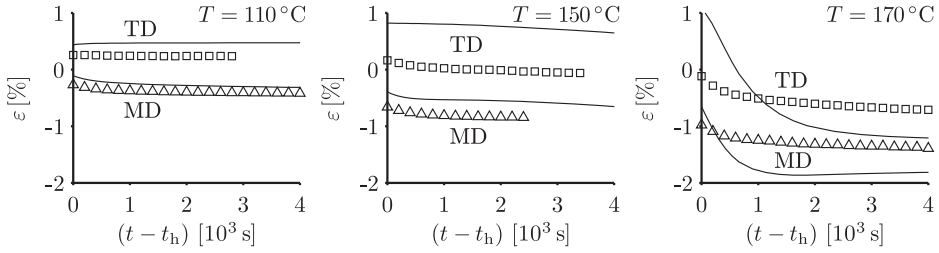
Figure 5.11: Dependence of strain on time during annealing in case of heating from $60\,°C$ to $110\,°C$, $150\,°C$ and $170\,°C$ with a heating rate of $5\,°C/min$. Comparison of model results (solid lines) and measurements (symbols) for MD and TD.
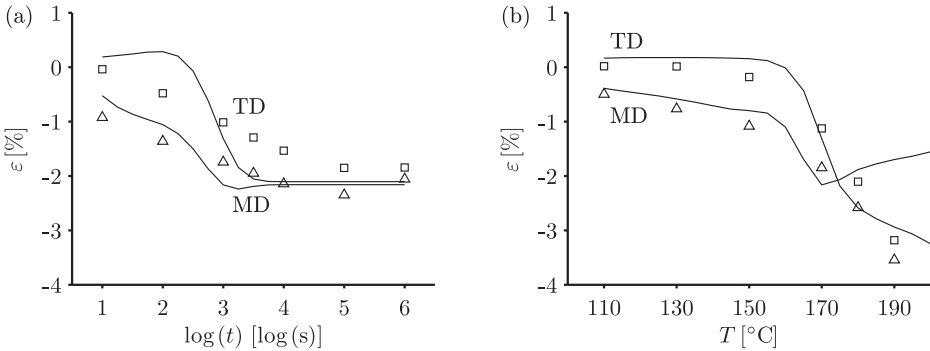

Figure 5.12: Dependence of residual strain on annealing time at $170\,°C$ (a) and on annealing temperature for an annealing time of $10^3\,s$ (b) for the fast heating rate. Comparison of the model results (solid lines) and the measurements (symbols) for MD and TD.

(figure 5.12b) and heating and cooling rates of $\dot{T} = 17\,°C/s$. The model qualitatively predicts the behaviour of the PET film. For an annealing temperature of $170\,°C$, the model demonstrates fast deformation, reaching equilibrium faster than $10^4\,s$. In figure 5.12b, qualitative deviations are observed at temperatures above $T = 170\,°C$, where in the model, the internal biaxial stress state changes rapidly to a uniaxial stress state and the material starts to expand in MD. This can be remedied by using more relaxation modes. In the temperature regime corresponding to the application conditions (for flexible electronics manufacturing), up to $170\,°C$, the absolute deviation between the predicted and experimentally determined strain does not exceed $3.5 \cdot 10^{-3}$.

5.5.3 Simulation of the long-term response

As indicated in the introduction, the long-term behaviour of the material considered here was already predicted with the composite inclusion model in previous chapter. In the present chapter, an extension is made to the model, such that the pre-deformation (internal stress) of the non-crystalline phase in now modelled with two separate modes, describing the behaviour of the PET
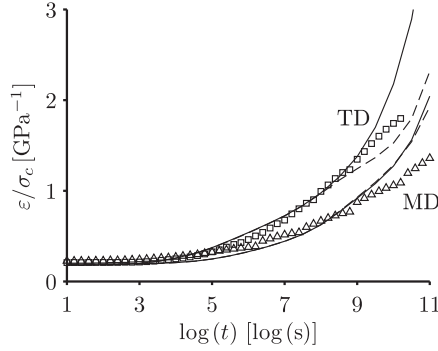
Figure 5.13: Dependence of the creep compliance of oriented PET on time for different loading directions. Comparison of simulations (lines) with measurements (symbols). Measurements are master curves constructed for $50\,^{\circ}\text{C}$, taken from chapter 4. The case when two pre-deformation modes are used (solid lines) is compared to the case when one pre-deformation mode is used (dashed lines), results corresponding to the latter case taken from chapter 4.

film at high temperatures. A simulation of the same creep conditions as in previous chapter with the extended model is shown in figure 5.13. As observed in the figure, the creep prediction of the model at $50\,^{\circ}\text{C}$ and a stress of $5\,\text{MPa}$ is not affected by the model extension, i.e. at lower temperatures the non-crystalline phase of the film demonstrates a uniaxial pre-deformation state (tensile state of the molecular network in MD). The deviation above 10^9 s is a result of the asynchronous relaxation in the hardening viscoplastic elements due to a difference in the magnitude of the stress to which these elements are subjected. This deviation does not influence the applicability of the model.

5.5.4 Local deformations

Deformation processes in separate phases of the material are characterised with inclusion-averaged equivalent plastic shear rates of individual slip systems and of the non-crystalline phase:

$$\langle\dot{\gamma}^{\alpha}\rangle = \frac{1}{N^{\text{I}}}\sum_{k=1}^{N^{\text{I}}}\left|\dot{\gamma}^{\alpha k}\right|; \quad \langle\dot{\gamma}^{\text{a}}\rangle = \frac{1}{N^{\text{I}}}\sum_{k=1}^{N^{\text{I}}}\dot{\gamma}_{\text{p}}^{\text{a}k}, \quad \dot{\gamma}_{\text{p}}^{\text{a}k} = \sqrt{2\boldsymbol{D}_{\text{P}1}^{\text{a}} : \boldsymbol{D}_{\text{P}1}^{\text{a}}}, \tag{5.10}$$

which are shown in figure 5.14 for the case of slow heating (corresponding to the model results shown in figure 5.10). In contrast to the behaviour at low temperatures, at high temperatures, the $(100)[010]$ transverse slip system is the most active slip system with a higher plastic deformation rate than in the non-crystalline phase. The simulations show that the slip activity of this particular system mainly determines the residual macroscopic strain.

As discussed in section 5.4.1, the stress of the non-crystalline phase is split into two contributions: the intermolecular interactions and the molecular network. The latter is modelled with two viscoplastic hardening modes with different pre-deformation, representing two different deformation modes. Mode 1 is pre-stretched in TD and mode 2 is pre-stretched in MD. To quantify plastic deformation in the modes, associated with relaxation of the molecular network $\boldsymbol{F}_{\text{pr}\,j}^{\text{a}}$
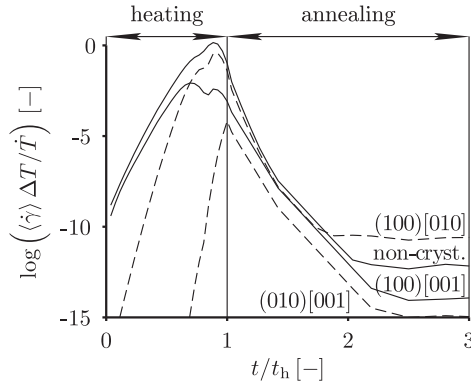
Figure 5.14: Evolution of inclusion-averaged plastic deformation rates on crystalline slip systems and the equivalent plastic deformation rate of the non-crystalline phase. Note that the maximum temperature is reached at $t = t_h$, i.e. the conditions (heating rate and annealing temperature) are the same as for results shown in figure 5.10.

(see figure 5.6d), the components of the inclusion-averaged plastic deformation gradient tensors are compared in figure 5.15a. It can be observed that one of the processes is slower and has lower accumulated plastic deformation. The amount of plastic deformation is influenced by the amount of pre-deformation.

The internal stress state of the molecular network of the non-crystalline phase is shown in figure 5.15b. The difference between MD and TD components of the volume-averaged tensor $\boldsymbol{\sigma}_r^a$, split into the contributions of two modes, is shown. Mode 1 is initially in a tensile state in TD and in a compressive state in MD, i.e. the in-plane stress state is close to uniaxial. Mode 2 provides an opposite initial stress state with a higher magnitude of stress. As observed in figure 5.15b, the speed of stress relaxation of these modes is different. Therefore the total internal stress is transformed during relaxation from a state which is close to uniaxial (a positive MD stress component and a negative TD component) to a state which is close to biaxial (both MD and TD components are positive and approximately equal).

The deformation of the non-crystalline phase within the layered domain is strongly dependent on the orientation of the interface. The components of the deformation gradient tensor of the non-crystalline phase $\boldsymbol{F}^a$ corresponding to the principal directions of the film depending on the orientation of the layered domains are shown in figure 5.16 (the corresponding macroscopic response is shown in figure 5.10). The selected temperatures correspond to moments when constant-rate thermal deformation is observed ($T = 90\,^{\circ}\mathrm{C}$), a change from expansion to shrinkage for TD ($T = 160\,^{\circ}\mathrm{C}$) and the end of the heating stage ($T = 190\,^{\circ}\mathrm{C}$). Upon heating, the non-crystalline phase is contracting in MD and expanding in TD for domains with an interface normal oriented towards MD. The opposite effect is observed for domains, for which the interface normal is oriented towards TD. It was found that the molecular network stress hardly depends on the orientation of the layered domain. The maximum value of the variation in stress tensor components was found to be $0.35\,\mathrm{MPa}$; for a comparison see figure 5.15b.

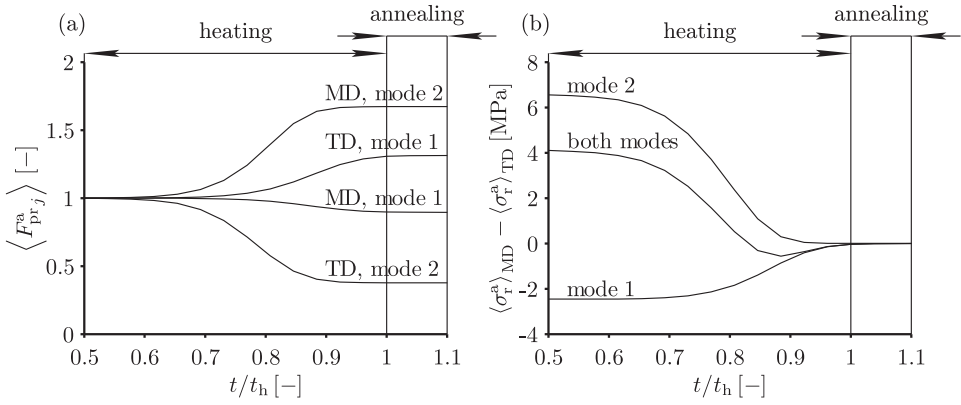The effect of the heating rate on the equivalent plastic deformation of the non-crystalline phase

Figure 5.15: Evolution of TD and MD components of the inclusion-averaged plastic deformation gradient tensors in viscoelastic elements associated with the molecular network of the non-crystalline phase, showing internal relaxation (a). Evolution of the difference between MD and TD components of the stress tensor associated with the molecular network of the non-crystalline phase (b). Note that the maximum temperature is reached at $t = t_\mathrm{h}$, i.e. the conditions (heating rate and annealing temperature) are the same as for the the results shown in figure 5.10.
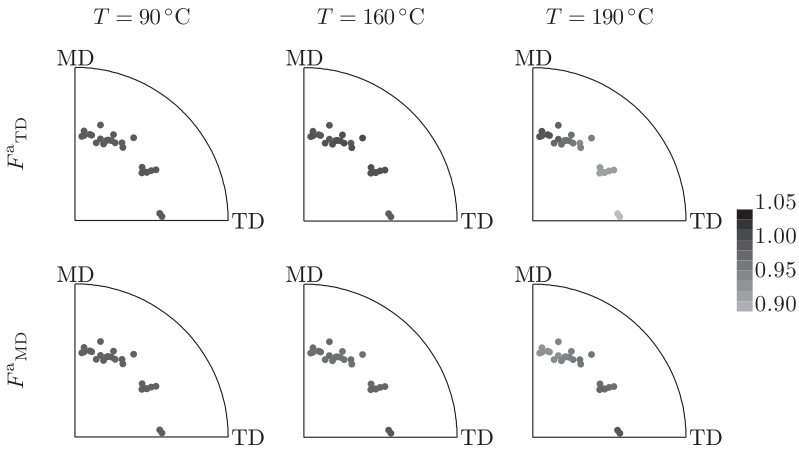

Figure 5.16: Equal area projection pole figures showing the initial normals to the interface between phases $(\vec{n}^\mathrm{I})$ for oriented material. The magnitude of TD and MD components of the deformation gradient tensors of the non-crystalline phase of layered domains is shown in colour. Heating up to $190\,^\circ\mathrm{C}$ is simulated with a heating rate of $1\,^\circ\mathrm{C}/\mathrm{min}$, results corresponding to two intermediate and final temperatures are shown.
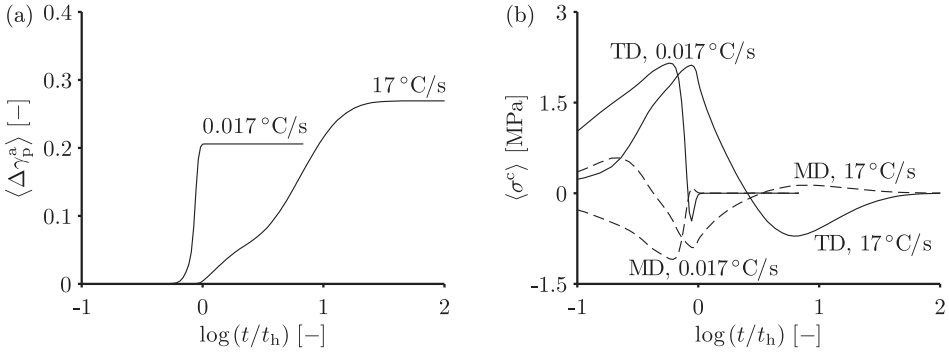
Figure 5.17: Influence of heating rate on the inclusion-averaged equivalent plastic deformations in elasto-viscoplastic elements associated with the molecular network of the non-crystalline phase (a) and on the volume-averaged stress in the crystalline phase (b). In (b) the evolution of TD and MD tensor components is shown.

as defined in equation (5.10) is shown in figure 5.17a. The relative change in plastic deformation $\Delta\gamma_p^a(t) = \gamma_p^a(t) - \gamma_p^a(0)$ is shown. Note that in case of slow heating, the magnitude of plastic deformation is lower, i.e. the amount of stress relaxation increases with decreasing heating rate. It was found that components of the volume-averaged stress tensor of the crystalline phase corresponding to TD and MD in the case of slow heating are qualitatively different than those for fast heating, see figure 5.17b. The absolute value of the stress is slightly higher for the slow heating and is qualitatively different for MD, where it is compressive during fast heating and tensile during slow heating. When thermal expansion for both phases is disabled in the model (results not shown here), the stress in the crystalline phase is similar for both heating rates, i.e. the TD component increases and the MD component decreases during the initial part of the heating. The initial qualitative difference for MD is due to the hydrostatic pressure resulting from a different thermal expansion of the phases. The compressive stresses in TD and tensile stresses in MD in the crystalline phase originate from the relaxation of the stress associated with the molecular network, see figure 5.15b.

5.6   Conclusions

In this chapter, mechanisms of reversible and irreversible thermal deformation of a polymer film produced by biaxial stretching, have been investigated both experimentally and numerically using a micromechanical modelling approach taking into account the microstructure and different phases of the material. The investigated thermo-mechanical effects can be classified as shape memory effects, since the material is partially returning to its initial state prior to biaxial drawing. The measured thermo-mechanical film behaviour during heating was anisotropic with a qualitative change in thermal deformation around 160 °C, after which significant thermal shrinkage is observed for both directions, while at lower temperatures thermal shrinkage is observed only for one of the principal directions of the film. Previous modelling work indicated the necessity of taking into account the internal stress state of the non-crystalline phase for micromechanical modelling of the long-term response. In this chapter, the internal stress state is described by two deformation processes, each

with its own internal stress state and thermal activation energy. At low temperatures, both processes act as one process as modelled in chapter 4, such that the molecular network is in a tensile state in MD and in a compressive state in TD. With such an internal stress state of the material, the model quantitatively predicts the measured creep behaviour. At higher temperatures, due to a difference of activation energies, the influence of the processes is disparate.

The two separate modes have pre-stretches in MD and TD and are activated at different temperatures. During biaxial drawing of PET film, molecules acquire mainly two types of orientations, in MD and in TD [107, 108, 111]. Thus pre-stretches of the viscoelastic hardening modes can be linked to deformations of the film, which occur in MD and TD drawing steps. Shrinkage in MD is observed at lower temperatures, which indicates that molecules that are oriented in MD are mechanically less constrained than ones oriented in TD. The difference of these sets of orientations was also confirmed by WAXD (see chapter 4), where mostly crystals with MD chain orientations were detected, which suggests that molecules with TD orientation do not have perfect crystalline symmetry and thus can be classified as oriented non-crystalline phase.

A qualitative mismatch between the experimentally and numerically obtained coefficient of linear thermal expansion was observed for oriented material. Due to the dominant chain orientation in MD, the CTE value in MD is expected to be lower than in TD, which was not experimentally observed for this material. An explanation for the mismatch may be the anisotropy of the non-crystalline phase, which influences the macroscopic behaviour. This means that a negative thermal expansion in TD of the non-crystalline phase (as for the chain direction of crystalline phase) should be taken into account to explain macroscopic thermal expansion of the film. For an isotropic material, the measured decrease of CTE with increasing crystallinity was adequately predicted by the micromechanical model. There is a small influence of the mismatch of the CTE prediction of the oriented film on the simulation of thermal deformation during heating, i.e. figures 5.10 and 5.11, where simultaneously reversible and irreversible effects are observed. For example at $150\,^\circ\text{C}$, with an accurate prediction of the CTE, the difference between model and experiment would have been larger in MD by an absolute value of strain of $1.2 \cdot 10^{-3}$ and smaller in TD by an absolute value of strain of $2.9 \cdot 10^{-3}$, whereas the experimental scatter of the absolute value of strain is up to $2.5 \cdot 10^{-3}$. Therefore, it can be concluded that simulation of the combined effect of reversible and irreversible thermal deformation is not qualitatively affected by the mismatch in CTE prediction, since the contribution of the irreversible deformation to the total strain is higher.

It was found that at the microscopic scale, the deformation mechanisms do not significantly depend on the orientation of the interface during heating up to $160\,^\circ\text{C}$. The heating rate significantly influences not only the macroscopic behaviour but also the stress distribution at the local scale. During slow heating, the crystalline phase is subjected to a slightly higher equivalent stress than during fast heating, with a qualitative change in the MD component of the average crystalline stress tensor from compressive to tensile.

5.A   Appendix: constitutive behaviour of non-crystalline phase

In this section, the equations representing the constitutive behaviour of the non-crystalline phase are summarised. For each mode $i = \overline{1, N^{\mathrm{a}}}$, a multiplicative decomposition of the deformation gradient tensor is used (the plastic deformation is taken spin-free): $\boldsymbol{F}^{\mathrm{a}} = \boldsymbol{F}^{\mathrm{a}}_{\mathrm{e}_i} \cdot \boldsymbol{F}^{\mathrm{a}}_{\mathrm{t}} \cdot \boldsymbol{F}^{\mathrm{a}}_{\mathrm{p}_i}$. The Cauchy stress tensor is split into a driving stress, which, in turn, is split into a hydrostatic part and

a deviatoric part and a hardening stress:

$$\boldsymbol{\sigma}^{\mathrm{a}} = \boldsymbol{\sigma}_{\mathrm{s}}^{\mathrm{ah}} + \boldsymbol{\sigma}_{\mathrm{s}}^{\mathrm{ad}} + \boldsymbol{\sigma}_{\mathrm{r}}^{\mathrm{a}}. \tag{A1}$$

The driving stress represents the contribution of the intermolecular interactions and is modelled with N^{a} viscoplastic modes, whereas the hardening stress represents the molecular network modelled with N^{r} viscoplastic modes:

$$\boldsymbol{\sigma}_{\mathrm{s}}^{\mathrm{ah}} = K^{\mathrm{a}}\left(J_{\mathrm{e}}^{\mathrm{a}} - 1\right)\boldsymbol{I}; \quad \boldsymbol{\sigma}_{\mathrm{s}}^{\mathrm{ad}} = \sum_{i=1}^{N^{\mathrm{a}}} \boldsymbol{\sigma}_{\mathrm{s}\,i}^{\mathrm{a}\,\mathrm{d}} = \sum_{i=1}^{N^{\mathrm{a}}} G_{i}^{\mathrm{a}} \tilde{\boldsymbol{B}}_{\mathrm{e}\,i}^{\mathrm{a}\,\mathrm{d}}; \quad \boldsymbol{\sigma}_{\mathrm{r}}^{\mathrm{a}} = \sum_{j=1}^{N^{\mathrm{r}}} G_{\mathrm{r}\,j} \tilde{\boldsymbol{B}}_{\mathrm{er}\,j}^{\mathrm{a}\,\mathrm{d}}, \tag{A2}$$

with K^{a} being the bulk modulus, G_{i}^{a} the shear moduli, $G_{\mathrm{r}\,j}$ the hardening moduli and N^{r} the number of viscoelastic hardening modes. The isochoric elastic Finger tensor of mode i is calculated as:

$$\tilde{\boldsymbol{B}}_{\mathrm{e}\,i}^{\mathrm{a}} = J_{\mathrm{e}\,i}^{\mathrm{a}\,-\frac{2}{3}} \boldsymbol{F}_{\mathrm{e}\,i}^{\mathrm{a}} \cdot \boldsymbol{F}_{\mathrm{e}\,i}^{\mathrm{a}\,\mathrm{T}}. \tag{A3}$$

The elastic deformation gradient tensors of the modes corresponding to the molecular network, are determined from the following multiplicative decomposition:

$$\boldsymbol{F}^{\mathrm{a}} = \boldsymbol{F}_{\mathrm{er}\,j}^{\mathrm{a}} \cdot \boldsymbol{F}_{\mathrm{t}}^{\mathrm{a}} \cdot \boldsymbol{F}_{\mathrm{pr}\,j}^{\mathrm{a}} \cdot \boldsymbol{F}_{\mathrm{d}\,j}^{\mathrm{a}\,-1}, \quad j = \overline{1, N^{\mathrm{r}}}, \tag{A4}$$

where $\boldsymbol{F}_{\mathrm{d}\,j}^{\mathrm{a}}$ is a deformation gradient tensor determining the initial pre-deformation of the network, such that $\det\left(\boldsymbol{F}_{\mathrm{d}\,j}^{\mathrm{a}}\right) = 1$. In this work the following form is adopted:

$$\boldsymbol{F}_{\mathrm{d}\,j}^{\mathrm{a}} = \lambda_{\mathrm{TD}\,j}\vec{e}_{1}\vec{e}_{1} + \lambda_{\mathrm{MD}\,j}\vec{e}_{2}\vec{e}_{2} + \frac{1}{\lambda_{\mathrm{TD}\,j}\lambda_{\mathrm{MD}\,j}}\vec{e}_{3}\vec{e}_{3}, \tag{A5}$$

where $\vec{e}_{2}$ corresponds to MD. The isochoric elastic Finger tensor of mode j, $\tilde{\boldsymbol{B}}_{\mathrm{er}\,j}^{\mathrm{a}}$, is calculated in a similar way as in equation (A3). The evolution of thermal expansion is according to:

$$\boldsymbol{L}_{\mathrm{t}}^{\mathrm{c}} = \dot{\boldsymbol{F}}_{\mathrm{t}}^{\mathrm{c}} \cdot \boldsymbol{F}_{\mathrm{t}}^{\mathrm{c}-1} = \alpha^{\mathrm{a}}\dot{T}\boldsymbol{I}, \tag{A6}$$

where α^{a} is the scalar isotropic thermal expansion coefficient.

The viscoplastic behaviour is defined by the plastic part of the deformation rate:

$$\boldsymbol{D}_{\mathrm{p}\,i}^{\mathrm{a}} = \frac{1}{2}\left(\boldsymbol{L}_{\mathrm{p}\,i}^{\mathrm{a}} + \boldsymbol{L}_{\mathrm{p}\,i}^{\mathrm{a}\,\mathrm{T}}\right) = \frac{\boldsymbol{\sigma}_{\mathrm{s}\,i}^{\mathrm{a}\,\mathrm{d}}}{2\eta_{i}}. \tag{A7}$$

The viscosities η_{i} for $i = \overline{1, N^{\mathrm{a}}}$ in equation (A7) depend on the equivalent deviatoric driving stress τ, temperature T, pressure p^{a}, and thermodynamic state S, which here is taken to be 0:

$$\eta_{i} = \eta_{0\,i}\exp\left(\frac{\Delta U}{R}\left(\frac{1}{T} - \frac{1}{T_{\mathrm{r}}}\right)\right)\frac{\tau/\tau_{0}}{\sinh\left(\tau/\tau_{0}\right)}\exp\left(\frac{\mu p^{\mathrm{a}}}{\tau_{0}}\right)\exp\left(S\right), \quad i = \overline{1, N^{\mathrm{a}}}; \tag{A8}$$

$$\tau = \sqrt{\frac{1}{2}\boldsymbol{\sigma}_{\mathrm{s}}^{\mathrm{ad}} : \boldsymbol{\sigma}_{\mathrm{s}}^{\mathrm{ad}}}; \quad \tau_{0} = \frac{kT}{V^{*}}, \tag{A9}$$

Table 5.3: Components of the stiffness matrix and thermal expansion tensor of the PET crystal at 300 K, from [25].

parameter	C_{11}^{c}	C_{22}^{c}	C_{33}^{c}	C_{44}^{c}	C_{55}^{c}	C_{66}^{c}	C_{12}^{c}	C_{13}^{c}	C_{23}^{c}
value [GPa]	14.4	17.3	178.0	6.6	1.4	1.2	6.4	3.4	9.5

parameter	C_{14}^{c}	C_{24}^{c}	C_{34}^{c}	C_{15}^{c}	C_{25}^{c}	C_{35}^{c}	C_{45}^{c}
value [GPa]	−2.2	3.3	3.8	−0.3	−0.5	−0.7	0.2

parameter	C_{16}^{c}	C_{26}^{c}	C_{36}^{c}	C_{46}^{c}	C_{56}^{c}
value [GPa]	−1.8	0.5	−1.8	−0.4	0.0

parameter	α_{11}^{c}	α_{22}^{c}	α_{33}^{c}	$2\alpha_{23}^{c}$	$2\alpha_{13}^{c}$	$2\alpha_{12}^{c}$
value [$10^{-5}\mathrm{K}^{-1}$]	11.4	4.12	−1.07	4.5	−1.38	5.05

Table 5.4: Reference shear rates at different temperatures for the PET crystal.

slip system	(100)[001]	(010)[001]	(100)[010]
ξ^{α} at 295 K [s^{-1}]	10^{-16}	10^{-80}	10^{-30}
ξ^{α} at 463 K [s^{-1}]	$8 \cdot 10^{-6}$	$7 \cdot 10^{-7}$	$2 \cdot 10^{-2}$

where R is the universal gas constant, ΔU the activation energy, T_r a reference temperature, $\boldsymbol{\sigma}_\mathrm{s}^\mathrm{ad}$ is the overall deviatoric driving stress, k is the Boltzmann constant and V^* the activation volume. The plastic part of the deformation rate corresponding to the molecular network, $\boldsymbol{D}_{\mathrm{pr}\,j}^\mathrm{a}$, is calculated in a similar way as in equation (A7). The viscosities $\eta_{\mathrm{r}\,j}$ for hardening modes are only temperature dependent:

$$\eta_{\mathrm{r}\,j} = \eta_{0\mathrm{r}\,j} \exp\left(\frac{\Delta U_{\mathrm{r}\,j}}{R} \left(\frac{1}{T} - \frac{1}{T_\mathrm{r}} \right) \right), \quad j = \overline{1, N^\mathrm{r}}. \tag{A10}$$

5.B Appendix: model parameters

The stiffness matrix of the PET crystal is temperature dependent. In the model, values interpolated at a particular temperature are used [25]. Here only values at ambient temperature (300 K) are listed in table 5.3, where the Voigt notation (11, 22, 33, 23, 31, 12) is used (the coordinate system $\vec{i}_1\vec{i}_2\vec{i}_3$ is coupled to the crystal, see [25]). Parameters for the viscoplastic deformation for the crystalline phase are listed in table 5.4. For all slip systems, the reference shear stress is $\tau_0^\alpha = 1.1$ MPa.

For the non-crystalline phase, values of the parameters can be found in table 5.5. Relaxation times for the rejuvenated state are listed instead of viscosities $\tau = \eta/G^\mathrm{a}$, where the symbol τ is used for the relaxation time of the mode and not for the equivalent stress as in the model description.

Table 5.5: Model parameters for PET, non-crystalline phase.

parameter	ΔU [kJ/mol]		V^* [nm^3]		α^{a} [K^{-1}]		T_{r} [K]		K^{a} [MPa]	μ [$-$]
value	230		3.24		$7 \cdot 10^{-5}$		323		1800	0.048

parameter	τ_1	τ_2	τ_3	τ_4	τ_5	τ_6	τ_7	τ_8	τ_9	τ_{10}
value [s]	10^{12}	10^{11}	10^{10}	10^9	10^8	10^7	10^6	10^5	10^4	10^3

parameter	G_1^{a}	G_2^{a}	G_3^{a}	G_4^{a}	G_5^{a}	G_6^{a}	G_7^{a}	G_8^{a}	G_9^{a}	G_{10}^{a}
value [MPa]	8	13	12	16	50	53	102	257	274	28

parameter	λ_{TD1} [$-$]		λ_{MD1} [$-$]		λ_{TD2} [$-$]		λ_{MD2} [$-$]		τ_{r_1} [s]	G_{r_1} [MPa]
value	1.37		0.93		0.39		1.74		10^{13}	2.35

parameter	ΔU_{r_1} [kJ/mol]		ΔU_{r_2} [kJ/mol]		τ_{r_2} [s]	G_{r_2} [MPa]
value	225		245		10^{13}	2.35

6 Oriented PET film under complex loading conditions

Abstract: In this chapter, the ability of the composite inclusion model [73,74,81,83] to predict the thermo-mechanical behaviour of oriented polyethylene terephthalate film subjected to complex loading conditions is investigated. The studied cases represent industrially-relevant lithographic processing conditions (for polymer films that are used as substrates for flexible electronics). Anisotropic viscoplastic deformation of the film resulting from both creep loading (with varying imposed levels of stress) and heating is measured and simulated. Previously, the micromechanical model successfully predicted anisotropic creep at constant temperature (chapter 4) and reversible and irreversible thermal deformations at stress-free conditions (chapter 5). Here, the combination of these effects is studied. The influence of heating from below to above the glass transition temperature during mechanical loading and prior to loading, as well as the film behaviour during cyclic loading are investigated.

6.1 Introduction

The production of flexible electronics requires dimensionally highly stable polymer substrates with a predictable mechanical response. The most commonly used materials are semicrystalline, oriented and thermally stabilised polyethylene terephthalate (PET) and polyethylene naphthalate (PEN) films [2, 5]. The goal of this work is to analyse the response of such a substrate material when subjected to industrially-relevant conditions, including heating from below to above the glass transition temperature and step-like loading and unloading.

In chapter 4, the anisotropic creep behaviour of an oriented PET film was modelled using a micromechanical model referred to as the composite inclusion model [73, 74, 83]. In chapter 5, reversible and irreversible thermal deformations at stress-free conditions resulting from heating of an oriented PET film to above the glass transition temperature were predicted using this micromechanical model. In this chapter, a combination of these effects is investigated, i.e. creep and unloading above glass transition during and after heating of the polymer.

First, the influence of the variation of the creep stress on the material behaviour above T_g is studied. In the second case, a variation in temperature (heating from below T_g to above) is added. Additionally, the effect of creep during heating is studied separately. Finally, the behaviour of the material under cyclic loading is analysed.

6.2   Methods

6.2.1   Experimental

Thermally stabilised oriented PET film, manufactured by DuPont Teijin Films, was provided for the experimental analysis. The film was produced by sequential biaxial stretching with draw ratios $\lambda = 3.0\text{–}3.5$ in machine direction (MD) and transverse direction (TD), an average thickness of $125 \, \mu\text{m}$, a width of $90 \, \text{cm}$ and an approximate crystallinity of 50%. The glass transition temperature of this material is $T_\text{g} \approx 70 \,^{\circ}\text{C}$.

Strain measurements at varying temperatures were performed under uniaxial tensile stress-controlled conditions using a Zwick Z010 universal tensile tester equipped with a video extensometer, a temperature controlled chamber and a 1 kN force cell. Samples were shaped according to ISO 527-2, type 1BA. Specific stress and temperature profiles were imposed. The heating was performed with a constant heating rate of $5 \,^{\circ}\text{C}/\text{min}$. The highest imposed stress was 5 MPa. In the case of cyclic loading, the lowest imposed stress was 0.16 MPa, which is necessary to keep the sample straight while not leading to any noticeable creep effects at high temperatures. Prior to testing, the samples were dried in a temperature controlled chamber at $50 \,^{\circ}\text{C}$ for 60 min to prevent interference of hygroscopic expansion with the measurements. The experimentally obtained engineering strain was converted to true strain.

6.2.2   Modelling

The material behaviour is modelled as the behaviour of an aggregate of layered domains, consisting of two phases: crystalline and amorphous. A detailed model description can be found in chapter 3, section 3.A. The macroscopic scale corresponds to a material point, where the Cauchy stress tensor $\boldsymbol{\sigma}^{\text{M}}$ and the deformation gradient tensor $\boldsymbol{F}^{\text{M}}$ are volume averaged quantities of the aggregate. Each phase in a domain is described with its own constitutive law and has homogeneous stress and deformation fields. Compatibility and equilibrium conditions are enforced at the interface between the phases. The average stress tensor $\boldsymbol{\sigma}^{\text{I}}$ and deformation gradient tensor $\boldsymbol{F}^{\text{I}}$ of each layered domain are obtained by volume averaging. The domains are coupled using a mean-field interaction law [74, 83]: the components of the inclusion-averaged stress and deformation gradient tensors that are not constrained by intra-inclusion equilibrium and compatibility conditions, are equal to their corresponding macroscopic quantities. Macroscopic quantities $\boldsymbol{F}^{\text{M}}$ and $\boldsymbol{\sigma}^{\text{M}}$ are obtained by volume averaging the inclusion-averaged quantities $\boldsymbol{\sigma}^{\text{I}}$ and $\boldsymbol{F}^{\text{I}}$.

The glassy polymer model by Govaert et al. [41, 42] is used for the non-crystalline phase (for details see chapter 3, sections 3.3, 3.A and chapter 5, section 5.A). It consists of a combination of viscoelastic Maxwell elements with neo-Hookean-like elasticity and non-linear viscosity, which is temperature and stress dependent. The stress dependency of the viscosity is described using an Eyring flow model and the temperature dependency is captured using an Arrhenius law. Thermal expansion is taken into account in the model. An internal pre-stress in the elastic elements describing the molecular network was included, thus introducing anisotropic yielding of the viscoplastic elements with isotropic behaviour in the elastic regime. The hardening modes also contain viscous elements, for which two modes with different activation energies and different pre-deformations are used.

The crystalline phase is modelled with crystal viscoplasticity [98], where the deformation is decomposed into elastic and viscoplastic parts in addition to the thermal expansion. The elastic
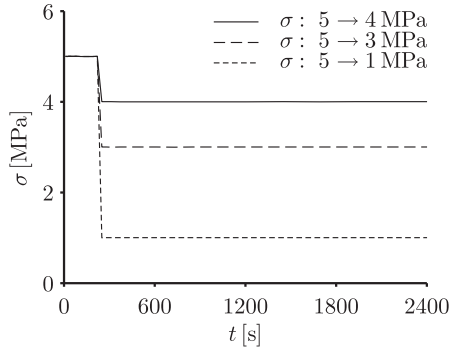
Figure 6.1: Dependence of the applied creep stress on time imposed in simulations and experiments.

behaviour of the crystalline phase is anisotropic. The viscoplastic deformation is a superposition of shear deformations on a limited number of crystallographic slip systems with an Eyring flow equation relating shear rate and resolved shear stress and an Arrhenius law relating shear rate and temperature [81]. The model parameters, used here are taken from chapter 5.

6.3 Results

6.3.1 Creep and unloading at constant temperature

The first case considered is uniaxial creep under stress with a step-like drop. The dependence of the applied creep stress on time is shown in figure 6.1. The creep stress of $5 \, \mathrm{MPa}$ is maintained for $220 \, \mathrm{s}$ and is reduced afterwards to $4, 3$ or $1 \, \mathrm{MPa}$. A constant temperature of $90 \, °\mathrm{C}$, which is above T_g, is maintained. Each sample is held at the test temperature for approximately 3 minutes before loading.

The simulated film behaviour qualitatively matches the measured behaviour, as shown in figure 6.2. In the case of MD loading, the strain increases further when the stress is reduced to $4 \, \mathrm{MPa}$, whereas it stays relatively constant when the stress is changed to $3 \, \mathrm{MPa}$ or decreases when the stress is lowered to $1 \, \mathrm{MPa}$. The constant strain in the case of a reduction to $3 \, \mathrm{MPa}$, is a result of a balance between the applied creep stress and the internal stress, which originates from the biaxial drawing of the film and which contributes to the deformation of the film above the glass transition temperature. After the instantaneous drop due to the stress reduction, the strain becomes negative because of this shrinkage stress. For MD, also large shrinkage was observed under stress-free conditions, see chapter 4. In the case of TD loading, irreversible deformation above T_g is positive for this film (see chapter 5). Therefore, for the creep conditions imposed here, in the case of TD loading, only increasing or constant strain is observed, even for a stress reduction to $1 \, \mathrm{MPa}$.

6.3.2 Creep and unloading with heating above glass transition

In the second case considered, the creep stress of $5 \, \mathrm{MPa}$ is maintained for $1220 \, \mathrm{s}$ and subsequently reduced to $4, 3$ or $1 \, \mathrm{MPa}$. During the first stage of creep, after $240 \, \mathrm{s}$, the temperature is changed
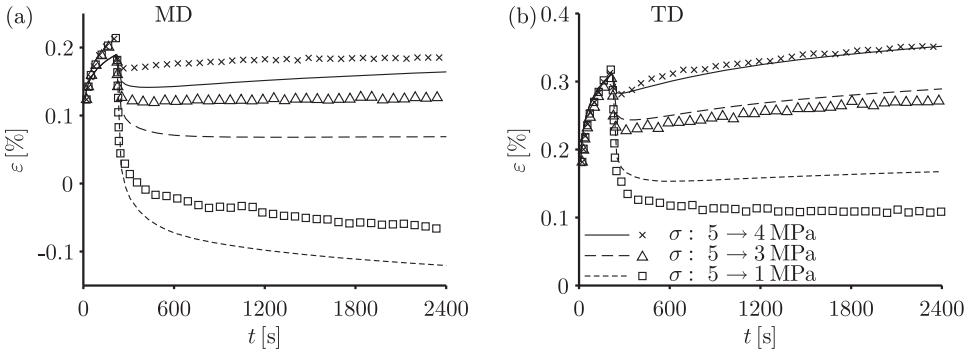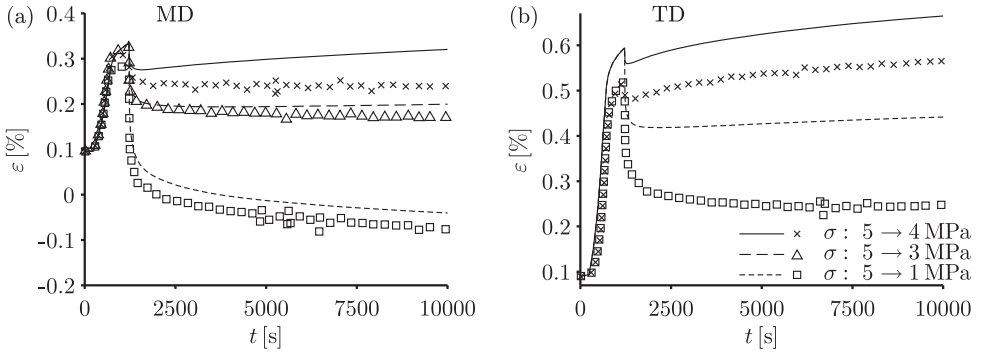
Figure 6.2: Dependence of strain on time in MD (a) and TD (b) under a creep stress of 5 MPa and subsequent unloading to 4 MPa, 3 MPa and 1 MPa at 90 °C; comparison of simulations (lines) and experiments (symbols). Each experimental curve corresponds to a single experiment.
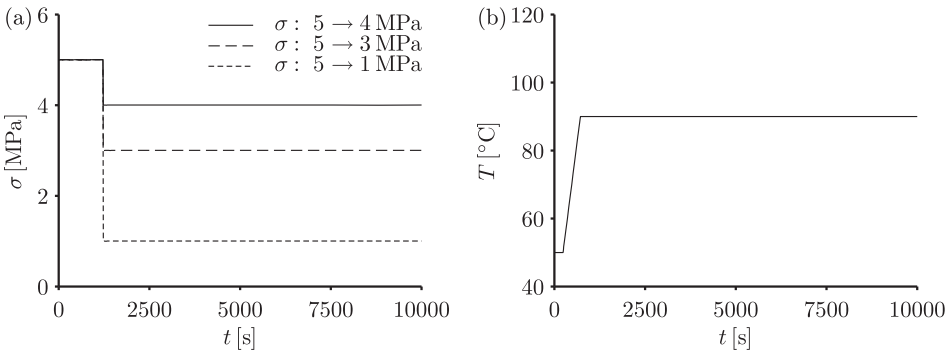
Figure 6.3: Dependence of the applied creep stress on time (a) and dependence of temperature on time (b) as imposed in the simulations and experiments.

from 50 °C to 90 °C with a rate of 5 °C/min, see figure 6.3.

In this case, the simulated behaviour also qualitatively matches the experimentally measured behaviour, as shown in figure 6.4. The model significantly overestimates the strain after unloading in TD to 1 MPa. In chapter 5, it was observed that the proposed model overestimates the coefficient of thermal expansion (CTE) in TD for this film, which here leads to an overestimation of the strain in the case of TD loading after heating. The deviation due to the thermal expansion appears during the first creep stage (creep stress of 5 MPa). The strain drop and subsequent deformation are predicted more accurately if this deviation in the thermal expansion is reduced, for example, by introducing anisotropic thermal expansion of the non-crystalline phase in the model.

Figure 6.4: Dependence of strain on time in MD (a) and TD (b) under a creep stress of 5 MPa and subsequent unloading to 4 MPa, 3 MPa and 1 MPa; comparison of simulations (lines) and experiments (symbols). Each experimental curve corresponds to a single experiment. During the first stage (creep stress of 5 MPa), the material is heated from 50 °C to 90 °C with a rate of 5 °C/min.
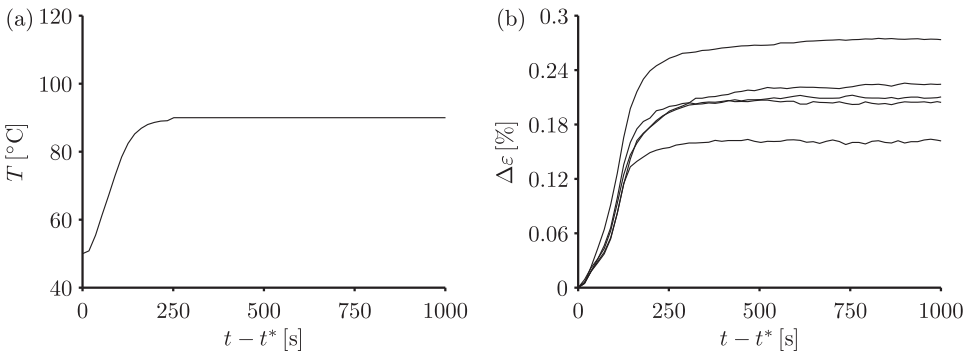
Figure 6.5: Dependence of the imposed temperature on time (a) and dependence of the strain on time in MD (b), five measurements are shown. A constant stress of 5 MPa is maintained. The change in strain, $\Delta\varepsilon$, with respect to the onset of heating ($t^* = 3600$ s) is shown.

6.3.3   Creep and unloading, longer creep stage

In the third case, the creep stress of 5 MPa is maintained for 7200 s and subsequently reduced to 4, 3 or 1 MPa. During the first stage of creep, after 3600 s, the temperature is changed from 50 °C to 90 °C with an approximate rate of 14 °C/min (the temperature profile is shown in figure 6.5a). Here, a relatively large variation of thermal expansion was observed between measurements performed at identical conditions, as shown in figure 6.5. This is attributed to the intrinsic inhomogeneity of orientation of the amorphous phase. Since the experimental spread mostly results from heating of the film, only the region after heating is considered for comparison with the simulations.

The quantitative prediction of the strain drop and subsequent deformation is similar to the case
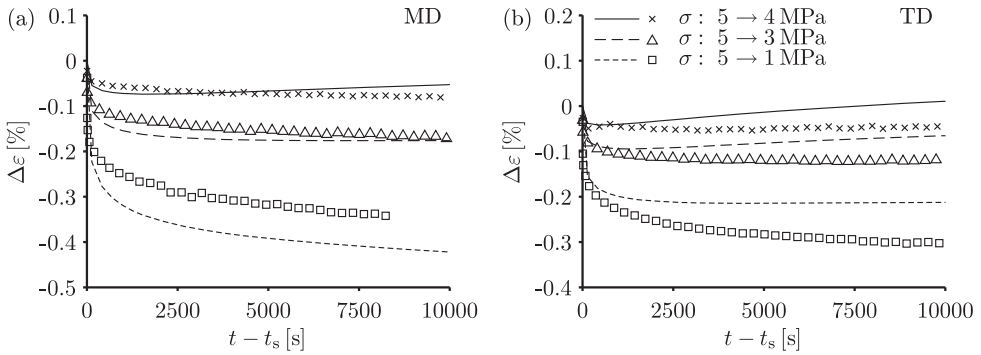
Figure 6.6: Dependence of the strain on time in MD (a) and TD (b) after unloading from 5 MPa to 4 MPa, 3 MPa and 1 MPa at 90 °C; comparison of simulations (lines) and experiments (symbols). Each experimental curve corresponds to a single experiment. The change in strain, $\Delta\varepsilon$, with respect to the point when stress is changed ($t_{\mathrm{s}} = 7200\,\mathrm{s}$) is shown.

of short loading, see figure 6.6. In the case of MD loading, after unloading, the creep rate prediction adequately matches the measurements. However, in the case of TD loading, an overestimation of the creep rate is observed.

6.3.4   Creep during heating

In addition to the previous case, the material behaviour during heating in a larger temperature range is investigated. In chapter 5, the film behaviour during heating under stress-free conditions was analysed. Here, the material is heated from 35 °C to 155 °C with an applied stress of 1.5 MPa or 5 MPa.

As observed in figure 6.7, the rate of deformation (i.e. the slope on the figure) resulting from creep, and reversible and irreversible thermal deformations, is relatively well predicted by the model in the case of TD loading and somewhat overestimated in the case of MD loading. Overall, the results match qualitatively, although some quantitative mismatches persist. Similar to stress-free heating, the strain predicted by the model is higher than the measured strain. In the case of 5 MPa loading, above 110 °C, the strain exceeds 1%, which is relatively large for the industrial application of interest, since the material is not used under such conditions.

6.3.5   Cyclic loading after heating

In the case of cyclic loading, the material is heated from 50 °C to 110 °C under stress-free conditions and after 10 min of annealing, 5 cycles of 10 min loading at 5 MPa (with intermediate unloading) are imposed. The stress and temperature profiles are shown in figures 6.8ab.

As seen in figures 6.8cd, the micromechanical model overestimates the strain during heating. From the experimental and numerical results it can be seen that the strain profile during each of the loading cycles is approximately the same. In terms of model prediction, the creep rate is adequately
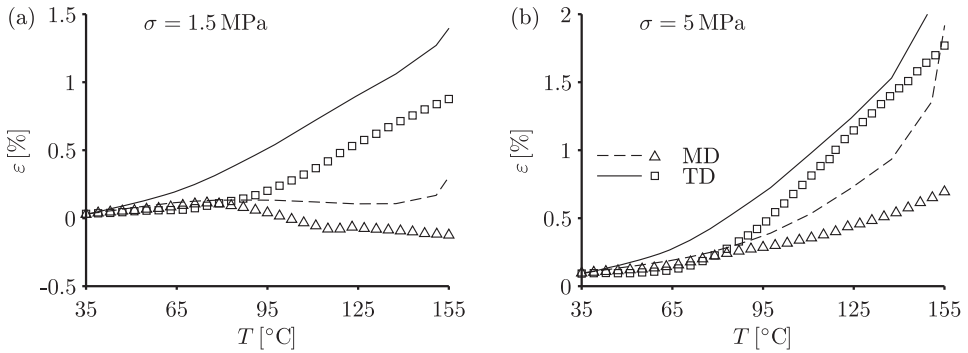
Figure 6.7: Dependence of strain on temperature in MD and TD during heating with an imposed heating rate of $5\,°\mathrm{C/min}$ in the case of an applied creep stress of $1.5\,\mathrm{MPa}$ or $5\,\mathrm{MPa}$; comparison of simulations (lines) and experiments (symbols). Each experimental curve corresponds to a single experiment.

simulated, however the elastic contribution of strain is only well predicted for MD with a systematic underestimation in TD.

6.4   Conclusions

In this chapter, a comparison of the thermomechanical behaviour of the oriented PET film under complex loading conditions obtained experimentally and computationally using the micromechanical composite inclusion model was performed. This comparison demonstrates that the two-phase micromechanical model gives a qualitative agreement with the experiment when the film is subjected to creep conditions, including step-like stress changes (film unloading), both below the glass transition temperature and above. The quantitative prediction of the anisotropic film behaviour was made possible through the incorporation of the internal stress state of the amorphous phase (see chapter 4).

The largest deviations of simulated and measured behaviour are observed during the heating stage, where in the case of MD loading the match between the experiments and the model is noticeably better than for TD loading. The main cause of this deviation is the difference between the measurements and predictions of the thermal expansion coefficients of the film (see chapter 5). The model prediction of the CTE in MD is lower than in TD, whereas the opposite is observed experimentally. This was attributed to the oriented non-crystalline phase, which was modelled as an isotropic material with isotropic thermal expansion, whereas the addition of an anisotropic pre-stress state did lead to an anisotropic yield response. Overall, the simulated thermo-mechanical behaviour at least qualitatively matches the measured behaviour.

An advantage of the discussed micromechanical model lies in its ability to predict the behaviour of polymer films with various internal molecular orientations, assuming these orientations are measured beforehand and the behaviour of the constituent phases is properly characterised. Although the model is micromechanically-based, there are still some empirical parameters, such as the pre-deformation ratios, which should be determined from experimental data. The number of these
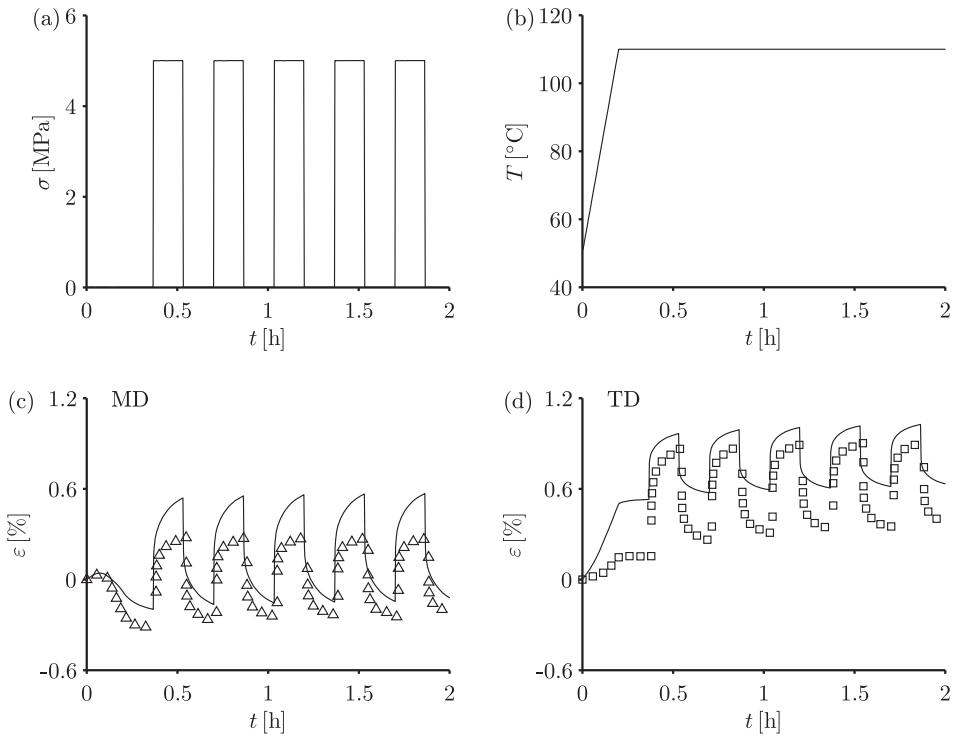
Figure 6.8: Dependence of the applied creep stress on time (a) and dependence of temperature on time (b) imposed in the simulations and experiments. Dependence of strain on time in MD (c) and TD (d); comparison of simulations (lines) and experiments (symbols). Each experimental curve corresponds to a single experiment.

parameters is relatively small, so the proposed approach can be used to efficiently predict the behaviour of films with various molecular orientations.

7 Conclusions and recommendations

7.1 Conclusions

In this thesis, a micromechanical model for the thermo-mechanical behaviour of oriented semicrystalline polyethylene terephthalate was developed. To establish a structure-property relationship and to investigate microstructural deformation mechanisms of the material, a multi-scale mean-field modelling approach was used.

A comparison of the selected micromechanical approach with multi-scale full-field simulations of a spherulitic (isotropic) material microstructure with elastic behavior revealed that the mean-field model is valid from a macroscopic point of view as well as from a micromechanical perspective. The predicted elastic material properties and microscopic deformation mechanisms obtained by both models qualitatively and quantitatively matched. It was demonstrated that the two-phase composite inclusion model is also able to adequately represent the behaviour of low crystalline (up to 25% of crystallinity) polymers. The performance of this model for cases of moderate and high crystallinity was investigated elsewhere (see [77, 83]).

In the full-field finite-element model, the geometrical properties of the crystalline phase of the spherulitic structure (aspect ratios of the crystalline lamella) do not significantly influence the prediction, and thus the applicability of the composite inclusion model for modelling isotropic structures. However it should be mentioned that this was verified for PET only, for which the difference in elastic properties of the phases is relatively small. This might not be the case, for example, for HDPE.

After having established the applicability of the mean-field model for isotropic PET, appropriate constitutive laws were used for the amorphous and crystalline phases to simulate the large-strain behaviour of PET under compression. The micromechanical model accurately predicted the increase of the yield stress with crystallinity, the dependence of the yield stress on strain rate and temperature, and the stress-strain behaviour up to 70% of strain for low crystallinity. For high crystallinity, a deviation of the model and experiment was observed above 25% of strain. The lower hardening stress that is observed experimentally, is a consequence of the break-up of the crystalline lamellae, an effect which is not included in the model. It was shown that the model is capable of capturing the decrease of the creep rate with an increase of the crystallinity. It was also demonstrated that texture evolution of isotropic PET under compression obtained with the model qualitatively corresponds with the experimentally observed texture evolution, despite the omitted effect of crystal break-up at high strains. No influence of material ageing on texture evolution was predicted by the model. To our knowledge this effect has not been investigated yet. At the microscopic scale,

various deformation measures were analysed and it was observed that in case of short-term large-strain deformation, the equivalent plastic deformation rate of the amorphous phase is higher than the slip rate on any of the slip systems of the crystalline phase. In contrast, for long-term small-strain deformation, the slip rate on the $(100)[001]$ slip system is significantly higher than the equivalent plastic deformation rate of the amorphous phase (see chapter 3).

Measurements on oriented film revealed a highly anisotropic nature of the material and significant spacial variations (along the width) in the film. Due to the drawing process, the film is homogeneous along the length direction. At the sides of the film (along the width) the principal directions (corresponding to the maximum and minimum values of the elastic and hardening moduli) are rotated by a certain angle. The mechanical behaviour in these principal directions at the side corresponded to the mechanical behaviour of the film in MD and TD in the centre.

After generating a set of inclusions with orientations matching the experimentally measured orientations of (100) and $(10\bar{5})$ planes by WAXD, the micromechanical model accurately predicted the large-strain anisotropic response of the film with a quantitative description of the dependence of the hardening modulus on the loading angle. A difference in activity of the slip systems for loading in MD and TD was observed. When the long-term mechanical behaviour was predicted by the model, a qualitative mismatch of simulations and measured behaviour appeared, which was attributed to the presence of internal stress in the amorphous phase, resulting from the manufacturing process, influencing the yield behaviour of the amorphous phase, rendering it anisotropic. After incorporation of a uniaxial pre-stress state of the amorphous phase, the model prediction quantitatively captures the experiments. Hence, it can be concluded that the presence of an internal stress state of the amorphous phase is essential to simulate the long-term behaviour of oriented polymers using a micromechanical model. The internal stress state depends on the drawing process during production of the film and should be identified from experimental data, since it cannot be measured directly.

Measurements of irreversible thermal deformation of the oriented PET film demonstrate a strong dependence of irreversible deformation on heating rate, with smaller deformations for low heating rates due to internal stress relaxation. At relatively low temperatures (slightly above T_g) the biaxially oriented film demonstrates positive irreversible deformation (expansion) in TD and negative (shrinkage) in MD. This effect is also time-dependent with most of the deformation taking place within 10^3–10^4 s. At high temperatures (above $160\,^\circ$C), irreversible shrinkage is also active in TD. A relatively large inhomogeneity (experimental spread) of the irreversible deformation was observed.

It was established that, to simulate the irreversible deformation using the micromechanical composite inclusion model, it is necessary to take into account internal stress relaxation of the molecular network in the non-crystalline phase and a temperature dependence of crystallographic slip. Furthermore, to simulate irreversible expansion and shrinkage in TD depending on temperature, it is also necessary to use multiple hardening viscoplastic modes (modes associated with the molecular network) with their own pre-deformations and activation energies. Micromechanical modelling incorporating these effects showed a change of the internal stress state from uniaxial to biaxial at high temperatures. Micromechanical modelling also confirmed a significant influence of the heating rate on the internal stress state.

7.2   Recommendations

Crystal break-up

As observed in chapter 3, the composite inclusion model highly overestimates the post-yield behaviour during compression of isotropic semicrystalline PET with a high crystallinity. Experimentally, the increase of total stress during plastic flow of isotropic samples was not observed. Additionally, there is experimental evidence of the break-up of the crystalline lamellae, which is not taken into account in the model. Therefore the reason for overestimation of the hardening stress by the composite inclusion model is the reinforcing effect of the crystalline phase. To remedy the mismatch between model prediction and experimental data, the effect of crystal break-up can be included in the composite inclusion model. Precise characterisation of this phenomenon requires WAXD and SAXS experimental data during polymer deformation. Even without including the effect of crystal break-up, the composite inclusion model qualitatively predicts texture evolution for HDPE [73, 83] and PET (see chapter 3) up to strains of 70%–100%, however after including this effect, the composite inclusion model can also be useful to predict texture evolution during drawing of oriented films and fibres up to large draw ratios. In this case, the phase transition effects, such as strain-induced crystallisation, should be taken into account and the constitutive behaviour of the non-crystalline phase should be further extended by including deformation resulting from the phase transition (for example, in the case of macroscopic modelling of biaxial hot drawing of PET, such effects were taken into account in [133]).

Stability of inclusions

In chapter 3, it was shown that in the case of large macroscopic deformations, some inclusions at certain moments of time undergo significant plastic deformations at a relatively short time scale. Such behaviour of the composite inclusion model was already observed previously [134]. This appears in figure 3.10 as large spikes in the dependence of plastic deformation rates on macroscopic strain. These spikes do not affect the overall behaviour due to the large size of the set of inclusions. During such deformation, the inclusion involved is significantly rotated, which is also noticeable in the pole figures. Inclusions that only have a specific orientation and specific stress state are affected. To further understand and remedy this phenomenon, the behaviour of a single inclusion subjected to varying macroscopic loads should be investigated numerically.

Property evolution during creep

As mentioned in chapter 4, there is significant change in polymer properties with annealing above T_{g}, which is revealed during creep loading of the film. In figure 7.1, it can be seen that with annealing prior to creep, the shape of the creep curves changes. For annealed samples, the creep rate increases with annealing time. A precise characterisation of the influence of thermal treatment of semicrystalline oriented PET on creep was out of the scope of this thesis. To simulate this effect, ageing kinetics (evolution of the parameter S_{a}) should be implemented.

Anisotropy of amorphous phase

As discussed in chapter 5, the state of the amorphous phase is anisotropic and somewhat complicated for the case of biaxially oriented films. To clearly understand anisotropy of the amor-
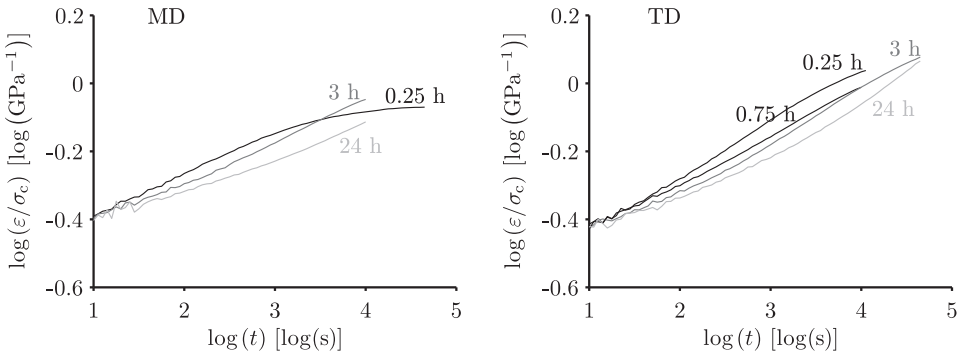
Figure 7.1: Influence of annealing time on the creep compliance for an applied stress of 5 MPa. Both annealing prior to testing and the creep loading were performed at 90 °C. Comparison of MD and TD for the central part of the film.

phous phase and its influence on the thermo-mechanical behaviour, films with a uniaxial orientation should be studied. For uniaxially drawn films with different draw ratios, the molecular chains in the amorphous phase should have only one preferential direction, and anisotropy of the phase depending on the draw ratio can be obtained by parameter identification. For biaxially drawn films, orientation of the amorphous phase can be characterised experimentally, for example, by using an infrared dichroism. This will contribute to further understanding of anisotropy and orientation of the amorphous phase.

Hygroscopic behaviour

In the case of PET, hygroscopic effects have only a minor contribution to macroscopic deformations with hygroscopic expansion coefficients being several times smaller than thermal expansion coefficients [135]. However for other semicrystalline polymers, such as Nylon, moisture significantly influences properties including the yield stress and the large-strain post-yield behaviour. For these types of polymers, the composite inclusion model might be useful in establishing a structure-property relationship at different humidity conditions. This requires an extension of the kinematics of the amorphous and crystalline phase in a way analogous to the incorporation of the thermal expansion.

Slip behaviour from molecular simulation

As shown in chapters 3 and 4 (and also in previous work for HDPE, [80, 81]), when the constitutive behaviour of the slip systems is obtained by parameter identification, non-uniqueness of the solution prevents the exact determination of the parameters. In the case of oriented material, groups of slip systems can be separated with different activity for different loading directions, which helps in identifying parameters, although still some non-uniqueness persists. As an alternative, the parameters of the slip systems may be obtained from molecular simulation of crystallographic slip in the crystalline phase. For example, in [136], plastic deformation of polyethylene was studied using atomistic Monte Carlo and molecular dynamics simulations. Slip kinetics obtained at molecular

level can later be used in the micromechanical continuum models.

Validating inclusion interaction law for large strains

In this thesis, in chapter 2, the composite inclusion interaction law was validated for the elastic isotropic material only. A similar validation using finite-element modelling can be performed for the large-strain regime and for the oriented material.

Incorporation of the intermediate phase for oriented material

In [77], an extended inclusion model was suggested introducing a third phase. It was demonstrated that incorporation of this phase is not necessary to simulate the behaviour of isotropic material. However, when behaviour of the oriented material is simulated, the presence of the intermediate phase might significantly influence the material behaviour. This could be investigated numerically.

Polymorphism

Some other semicrystalline polymers, such as PEN, which is also used as a substrate material for flexible electronics, demonstrate an existence of different crystal forms. Such crystal forms have different geometries, hence different elastic and thermal properties and more importantly different behaviours of the slip systems, which are of the same type. To simulate the behaviour of these materials, polymorphism should be taken into account.

Macroscopic modelling

As it was discussed in chapter 5, the precision of the description of the thermo-mechanical behaviour of the film at high temperatures can be improved by attributing individual pre-deformations to each viscoelastic mode. Using the micromechanical model, modified in such a way, a macroscopic constitutive thermo-elasto-viscoplastic model for oriented PET film can be developed. Such model could then be used in finite element software to simulate large areas of the film, which are inhomogeneous and are subjected to inhomogeneous conditions. These simulations may be used to optimise processing of the material and predict the film deformation with sufficient accuracy, as required by the application.

Bibliography

[1] D. Graham-Rowe. Electronic paper rewrites the rulebook for displays. *Nature Photonics*, 1(5):248–251, 2007.

[2] W. A. MacDonald, M. K. Looney, D. MacKerron, R. Eveson, R. Adam, K. Hashimoto, and K. Rakos. Latest advances in substrates for flexible electronics. *Journal of the Society for Information Display*, 15(12):1075–1083, 2007.

[3] S. Logothetidis. Flexible organic electronic devices: materials, process and applications. *Materials Science and Engineering: B*, 152(1-3):96–104, 2008.

[4] W. A. MacDonald. Engineered films for display technologies. *Journal of Materials Chemistry*, 14(1):4–10, 2004.

[5] W. A. MacDonald. Structural materials underpinning functional materials: teaching old dogs new tricks. *Polymer International*, 57(5):672–677, 2008.

[6] D. I. Bower. *An introduction to polymer physics*. Cambridge University Press, 2002.

[7] P. J. Flory. On morphology of crystalline state in polymers. *Journal of the American Chemical Society*, 84(15):2857–2867, 1962.

[8] C. J. Heffelfinger and P. G. Schmidt. Structure and properties of oriented poly(ethylene terephthalate) films. *Journal of Applied Polymer Science*, 9(8):2661–2680, 1965.

[9] A. Keller and S. Sawada. On the interior morphology of bulk polyethylene. *Makromolekulare Chemie*, 74:190–221, 1964.

[10] Y. Yamashita. Single crystals of poly(ethylene terephthalate). *Journal of Polymer Science Part A: General Papers*, 3(1PA):81–92, 1965.

[11] L. Lin and A. S. Argon. Structure and plastic deformation of polyethylene. *Journal of Materials Science*, 29(2):294–323, 1994.

[12] A. Keller. The spherulitic structure of crystalline polymers 1. Investigations with the polarizing microscope. *Journal of Polymer Science*, 17(84):291–308, 1955.

[13] A. Keller. The spherulitic structure of crystalline polymers 2. The problem of molecular orientation in polymer spherulites. *Journal of Polymer Science*, 17(85):351–364, 1955.

[14] A. Keller and J. R. S. Waring. The spherulitic structure of crystalline polymers 3. Geometrical factors in spherulitic growth and the fine-structure. *Journal of Polymer Science*, 17(86):447–472, 1955.

[15] P. Chandran and S. Jabarin. Biaxial orientation of poly(ethylene terephthalate) 1. Nature of the stress-strain curves. *Advances in Polymer Technology*, 12(2):119–132, 1993.

[16] V. B. Gupta, A. K. Jain, J. Radhakrishnan, and P. K. Chidambareswaran. Crystal perfection in axially oriented poly(ethylene terephthalate) fibers and films and its dependence on process variables. *Journal of Macromolecular Science, Part B: Physics*, B33(2):185–207, 1994.

[17] R. M. Gohil. Morphology-property relationship in oriented PET films: microstructural reorganization during heat treatment. *Journal of Applied Polymer Science*, 52(7):925–944, 1994.

[18] S. A. Jabarin. Orientation studies of poly(ethylene terephthalate). *Polymer Engineering and Science*, 24(5):376–384, 1984.

[19] J. D. Hoffman, G. T. Davis, and Jr. Lauritzen, J. I. *Treatise on solid state chemistry*, chapter The rate of crystallization of linear polymers with chain folding, pages 497–614. Springer US, 1976.

[20] Y. G. Fu, W. R. Busing, Y. M. Jin, K. A. Affholter, and B. Wunderlich. Structure analysis of the noncrystalline material in poly(ethylene terephthalate) fibers. *Macromolecular Chemistry and Physics*, 195(2):803–822, 1994.

[21] R. Androsch and B. Wunderlich. The link between rigid amorphous fraction and crystal perfection in cold-crystallized poly(ethylene terephthalate). *Polymer*, 46(26):12556–12566, 2005.

[22] P. G. Karagiannidis, A. C. Stergiou, and G. P. Karayannidis. Study of crystallinity and thermomechanical analysis of annealed poly(ethylene terephthalate) films. *European Polymer Journal*, 44(5):1475–1486, 2008.

[23] R. Rastogi, W. P. Vellinga, S. Rastogi, C. Schick, and H. E. H. Meijer. The three-phase structure and mechanical properties of poly(ethylene terephthalate). *Journal of Polymer Science Part B: Polymer Physics*, 42(11):2092–2106, 2004.

[24] R. D. Daubeny and C. W. Bunn. The crystal structure of polyethylene terephthalate. *Proceedings of the Royal Society of London. Series A, Mathematical and Physical Sciences*, 226(1167):531–542, 1954.

[25] G. C. Rutledge. Thermomechanical properties of the crystal phase of poly(ethylene terephthalate) by molecular modeling. *Macromolecules*, 30(9):2785–2791, 1997.

[26] J. Liu and P. H. Geil. Crystal structure and morphology of poly(ethylene terephthalate) single crystals prepared by melt polymerization. *Journal of Macromolecular Science, Part B: Physics*, 36(1):61–85, 1997.

[27] J. Liu, G. Sidoti, J. A. Hommema, P. H. Geil, J. C. Kim, and M. Cakmak. Crystal structures and morphology of thin-film, melt-crystallized, and polymerized poly(ethylene naphthalate). *Journal of Macromolecular Science, Part B: Physics*, B37(4):567–586, 1998.

[28] J. B. F. de Champchesnel, J. F. Tassin, L. Monnerie, P. Sergot, and G. Lorentz. Amorphous phase orientation in biaxially drawn poly(ethylene terephthalate) films. *Polymer*, 38(16):4165–4173, 1997.

[29] L. Sirelli, R. A. Pereira, C. A. Perez, and M. L. Dias. Thermal behavior of poly(ethylene terephthalate) crystalline and amorphous phases by wide angle X-ray scattering. *Journal of Macromolecular Science, Part B: Physics*, 45(2):343–359, 2006.

[30] A. Ajji, J. Guevremont, K. C. Cole, and M. M. Dumoulin. Orientation and structure of drawn poly(ethylene terephthalate). *Polymer*, 37(16):3707–3714, 1996.

[31] C. J. Heffelfinger and E. L. Lippert. X-ray low-angle scattering from oriented poly(ethylene terephthalate) films. *Journal of Applied Polymer Science*, 15(11):2699–2731, 1971.

[32] S. K. Sharma and A. Misra. The effect of stretching conditions on properties of amorphous polyethylene terephthalate film. *Journal of Applied Polymer Science*, 34(6):2231–2247, 1987.

[33] P. Chandran and S. Jabarin. Biaxial orientation of poly(ethylene terephthalate) 2. The strain-hardening parameter. *Advances in Polymer Technology*, 12(2):133–151, 1993.

[34] A. Bellare, R. E. Cohen, and A. S. Argon. Development of texture in poly(ethylene terephthalate) by plane-strain compression. *Polymer*, 34(7):1393–1403, 1993.

[35] C. Hakme, I. Stevenson, L. David, A. Voice, and G. Seytre. Thermo-mechanical behavior of uniaxially drawn and crystallized poly(ethylene naphthalene-2,6-dicarboxylate) (PEN) films. *Journal of Non-Crystalline Solids*, 353(47-51):4252–4261, 2007.

[36] R. M. Gohil. Morphology-property relationships in oriented PET films: a role of in-plane crystalline orientation distribution on the film properties. *Journal of Applied Polymer Science*, 48(9):1635–1648, 1993.

[37] C. P. Buckley and D. C. Jones. Glass-rubber constitutive model for amorphous polymers near the glass transition. *Polymer*, 36(17):3301–3312, 1995.

[38] C. P. Buckley, P. J. Dooling, J. Harding, and C. Ruiz. Deformation of thermosetting resins at impact rates of strain. Part 2: constitutive model with rejuvenation. *Journal of the Mechanics and Physics of Solids*, 52(10):2355–2377, 2004.

[39] M. C. Boyce, D. M. Parks, and A. S. Argon. Large inelastic deformation of glassy polymers. Part 1: rate dependent constitutive model. *Mechanics of Materials*, 7(1):15–33, 1988.

[40] E. M. Arruda and M. C. Boyce. Evolution of plastic anisotropy in amorphous polymers during finite straining. *International Journal of Plasticity*, 9(6):697–720, 1993.

[41] L. E. Govaert, P. H. M. Timmermans, and W. A. M. Brekelmans. The influence of intrinsic strain softening on strain localization in polycarbonate: modeling and experimental validation. *Journal of Engineering Materials and Technology*, 122(2):177–185, 2000.

[42] E. T. J. Klompen, T. A. P. Engels, L. E. Govaert, and H. E. H. Meijer. Modeling of the postyield response of glassy polymers: influence of thermomechanical history. *Macromolecules*, 38(16):6997–7008, 2005.

[43] L. C. A. van Breemen, E. T. J. Klompen, L. E. Govaert, and H. E. H. Meijer. Extending the EGP constitutive model for polymer glasses to multiple relaxation times. *Journal of the Mechanics and Physics of Solids*, 59(10):2191–2207, 2011.

[44] L. Figiel, F. P. E. Dunne, and C. P. Buckley. Computational modelling of large deformations in layered-silicate/PET nanocomposites near the glass transition. *Modelling and Simulation in Materials Science and Engineering*, 18(1):015001, 2010.

[45] H. X. Li and C. P. Buckley. Necking in glassy polymers: effects of intrinsic anisotropy and structural evolution kinetics in their viscoplastic flow. *International Journal of Plasticity*, 26(12):1726–1745, 2010.

[46] L. C. A. van Breemen, T. A. P. Engels, E. T. J. Klompen, D. J. A. Senden, and L. E. Govaert. Rate- and temperature-dependent strain softening in solid polymers. *Journal of Polymer Science Part B: Polymer Physics*, 50(24):1757–1771, 2012.

[47] J. E. Shepherd, D. L. McDowell, and K. I. Jacob. Modeling morphology evolution and mechanical behavior during thermo-mechanical processing of semi-crystalline polymers. *Journal of the Mechanics and Physics of Solids*, 54(3):467–489, 2006.

[48] M. J. Doyle. On the effect of crystallinity on the elastic properties of semicrystalline polyethylene. *Polymer Engineering and Science*, 40(2):330–335, 2000.

[49] K. J. Hsia, Y. B. Xin, and L. Lin. Numerical simulation of semi-crystalline nylon 6: elastic constants of crystalline and amorphous parts. *Journal of Materials Science*, 29(6):1601–1611, 1994.

[50] M. Uchida, T. Tokuda, and N. Tada. Finite element simulation of deformation behavior of semi-crystalline polymers with multi-spherulitic mesostructure. *International Journal of Mechanical Sciences*, 52(2):158–167, 2010.

[51] J. D. Eshelby. The determination of the elastic field of an ellipsoidal inclusion, and related problems. *Proceedings of the Royal Society of London. Series A, Mathematical and Physical Sciences*, 241(1226):376–396, 1957.

[52] S. Nikolov and I. Doghri. A micro/macro constitutive model for the small-deformation behavior of polyethylene. *Polymer*, 41(5):1883–1891, 2000.

[53] O. Gueguen, S. Ahzi, A. Makradi, and S. Belouettar. A new three-phase model to estimate the effective elastic properties of semi-crystalline polymers: application to PET. *Mechanics of Materials*, 42(1):1–10, 2010.

[54] R. Hill. A self-consistent mechanics of composite materials. *Journal of the Mechanics and Physics of Solids*, 13(4):213–222, 1965.

[55] A. Molinari, G. R. Canova, and S. Ahzi. A self-consistent approach of the large deformation polycrystal viscoplasticity. *Acta Metallurgica*, 35(12):2983–2994, 1987.

[56] S. Ahzi, N. Bahlouli, A. Makradi, and S. Belouettar. Composite modeling for the effective elastic properties of semicrystalline polymers. *Journal of Mechanics of Materials and Structures*, 2(1):1–21, 2007.

[57] O. Gueguen, S. Ahzi, S. Belouettar, and A. Makradi. Comparison of micromechanical models for the prediction of the effective elastic properties of semicrystalline polymers: application to polyethylene. *Polymer Science, Series A*, 50(5):523–532, 2008.

[58] T. Mori and K. Tanaka. Average stress in matrix and average elastic energy of materials with misfitting inclusions. *Acta Metallurgica*, 21(5):571–574, 1973.

[59] Y. Benveniste. A new approach to the application of Mori-Tanaka theory in composite materials. *Mechanics of Materials*, 6(2):147–157, 1987.

[60] X. Guan and R. Pitchumani. A micromechanical model for the elastic properties of semicrystalline thermoplastic polymers. *Polymer Engineering and Science*, 44(3):433–451, 2004.

[61] R. Hill. Continuum micro-mechanics of elastoplastic polycrystals. *Journal of the Mechanics and Physics of Solids*, 13(2):89–101, 1965.

[62] R. M. Christensen. Viscoelastic properties of heterogeneous media. *Journal of the Mechanics and Physics of Solids*, 17(1):23–41, 1969.

[63] A. Molinari, S. Ahzi, and R. Kouddane. On the self-consistent modeling of elastic-plastic behavior of polycrystals. *Mechanics of Materials*, 26(1):43–62, 1997.

[64] N. Lahellec and P. Suquet. Effective behavior of linear viscoelastic composites: a time-integration approach. *International Journal of Solids and Structures*, 44(2):507–529, 2007.

[65] S. Mercier and A. Molinari. Homogenization of elastic-viscoplastic heterogeneous materials: self-consistent and Mori-Tanaka schemes. *International Journal of Plasticity*, 25(6):1024–1048, 2009.

[66] S. Mercier, A. Molinari, S. Berbenni, and M. Berveiller. Comparison of different homogenization approaches for elastic-viscoplastic materials. *Modelling and Simulation in Materials Science and Engineering*, 20(2):024004, 2012.

[67] M. Hori and S. Nemat-Nasser. Double-inclusion model and overall moduli of multi-phase composites. *Mechanics of Materials*, 14(3):189–206, 1993.

[68] F. Bedoui, J. Diani, G. Regnier, and W. Seiler. Micromechanical modeling of isotropic elastic behavior of semicrystalline polymers. *Acta Materialia*, 54(6):1513–1523, 2006.

[69] J. C. Halpin and J. L. Kardos. The Halpin-Tsai equations: a review. *Polymer Engineering and Science*, 16(5):344–352, 1976.

[70] J. C. Halpin and J. L. Kardos. Moduli of crystalline polymers employing composite theory. *Journal of Applied Physics*, 43(5):2235–2241, 1972.

[71] J. L. Kardos and J. Raisoni. Potential mechanical response of macromolecular systems—a composite analogy. *Polymer Engineering and Science*, 15(3):183–190, 1975.

[72] R. L. McCullough, C. T. Wu, J. C. Seferis, and P. H. Lindenmeyer. Predictions of limiting mechanical performance for anisotropic crystalline polymers. *Polymer Engineering and Science*, 16(5):371–387, 1976.

[73] B. J. Lee, A. S. Argon, D. M. Parks, S. Ahzi, and Z. Bartczak. Simulation of large strain plastic deformation and texture evolution in high density polyethylene. *Polymer*, 34(17):3555–3575, 1993.

[74] B. J. Lee, D. M. Parks, and S. Ahzi. Micromechanical modeling of large plastic deformation and texture evolution in semicrystalline polymers. *Journal of the Mechanics and Physics of Solids*, 41(10):1651–1687, 1993.

[75] D. M. Parks and S. Ahzi. Polycrystalline plastic deformation and texture evolution for crystals lacking five independent slip systems. *Journal of the Mechanics and Physics of Solids*, 38(5):701–724, 1990.

[76] S. Ahzi, B. J. Lee, and R. J. Asaro. Plasticity and anisotropy evolution in crystalline polymers. *Materials Science and Engineering: A*, 189(1-2):35–44, 1994.

[77] A. Sedighiamiri, T. B. van Erp, G. W. M. Peters, L. E. Govaert, and J. A. W. van Dommelen. Micromechanical modeling of the elastic properties of semicrystalline polymers: a three-phase approach. *Journal of Polymer Science Part B: Polymer Physics*, 48(20):2173–2184, 2010.

[78] J. A. W. van Dommelen, D. M. Parks, M. C. Boyce, W. A. M. Brekelmans, and F. P. T. Baaijens. Micromechanical modeling of intraspherulitic deformation of semicrystalline polymers. *Polymer*, 44(19):6089–6101, 2003.

[79] J. A. W. van Dommelen, B. A. G. Schrauwen, L. C. A. van Breemen, and L. E. Govaert. Micromechanical modeling of the tensile behavior of oriented polyethylene. *Journal of Polymer Science Part B: Polymer Physics*, 42(16):2983–2994, 2004.

[80] A. Sedighiamiri, L. E. Govaert, and J. A. W. van Dommelen. Micromechanical modeling of the deformation kinetics of semicrystalline polymers. *Journal of Polymer Science Part B: Polymer Physics*, 49(18):1297–1310, 2011.

[81] A. Sedighiamiri, L. E. Govaert, M. J. W. Kanters, and J. A. W. van Dommelen. Micromechanics of semicrystalline polymers: yield kinetics and long-term failure. *Journal of Polymer Science Part B: Polymer Physics*, 50(24):1664–1679, 2012.

[82] M. Poluektov, J. A. W. van Dommelen, L. E. Govaert, I. Yakimets, and M. G. D. Geers. Micromechanical modelling of poly(ethylene terephthalate) using a layered two-phase approach. *Journal of Materials Science*, 48(10):3769–3781, 2013.

[83] J. A. W. van Dommelen, D. M. Parks, M. C. Boyce, W. A. M. Brekelmans, and F. P. T. Baaijens. Micromechanical modeling of the elasto-viscoplastic behavior of semi-crystalline polymers. *Journal of the Mechanics and Physics of Solids*, 51(3):519–541, 2003.

[84] L. H. Palys and P. J. Phillips. Microkinetics of crystallization in poly(ethylene terephthalate). *Journal of Polymer Science Part B: Polymer Physics*, 18(4):829–852, 1980.

[85] V. G. Kouznetsova, M. G. D. Geers, and W. A. M. Brekelmans. Multi-scale second-order computational homogenization of multi-phase materials: a nested finite element solution strategy. *Computer Methods in Applied Mechanics and Engineering*, 193(48-51):5525–5550, 2004.

[86] E. W. C. Coenen, V. G. Kouznetsova, and M. G. D. Geers. Computational homogenization for heterogeneous thin sheets. *International Journal for Numerical Methods in Engineering*, 83(8-9):1180–1205, 2010.

[87] P. J. Hine and I. M. Ward. Measuring the elastic properties of high-modulus fibres. *Journal of Materials Science*, 31(2):371–379, 1996.

[88] M. Matsuo and C. Sawatari. Morphological and mechanical properties of poly(ethylene terephthalate) gel and melt films in terms of the crystal lattice modulus, molecular orientation, and small angle X-ray scattering intensity distribution. *Polymer Journal*, 22(6):518–538, 1990.

[89] A. Miyagi and B. Wunderlich. Etching of crystalline poly(ethylene terephthalate) by hydrolysis. *Journal of Polymer Science: Polymer Physics Edition*, 10(10):2073–2083, 1972.

[90] B. J. Wang, C. Y. Li, J. Hanzlicek, S. Z. D. Cheng, P. H. Geil, J. Grebowicz, and R. M. Ho. Poly(trimethylene teraphthalate) crystal structure and morphology in different length scales. *Polymer*, 42(16):7171–7180, 2001.

[91] J. Petermann and U. Rieck. On the plastic deformation of fiber self-reinforced polymers. *Journal of Materials Science*, 22(3):1120–1126, 1987.

[92] C. L. Chang, W. Y. Chiu, K. H. Hsieh, and C. C. M. Ma. The molecular orientation and mechanical properties of poly(ethylene terephthalate) under uniaxial extension. *Journal of Applied Polymer Science*, 50(5):855–862, 1993.

[93] F. Bouquerel, P. Bourgin, and J. Perez. Viscoelastic behavior of thin bioriented poly(ethylene terephthalate) films under low and medium stresses. *Polymer*, 33(3):516–525, 1992.

[94] J. F. Graham, M. Kovar, P. R. Norton, P. Pappalardo, J. van Loon, and O. L. Warren. Quantitative nanoscale mechanical properties of a phase segregated homopolymer surface. *Journal of Materials Research*, 13(12):3565–3570, 1998.

[95] M. Poluektov, J. A. W. van Dommelen, L. E. Govaert, I. Yakimets, and M. G. D. Geers. Micromechanical modelling of short-term and long-term large-strain behaviour of polyethylene terephthalate. *Modelling and Simulation in Materials Science and Engineering*, 21:085015, 2013.

[96] C. P. Buckley and C. Y. Lew. Biaxial hot-drawing of poly(ethylene terephthalate): An experimental study spanning the processing range. *Polymer*, 52(8):1803–1810, 2011.

[97] M. C. Boyce, S. Socrate, and P. G. Llana. Constitutive model for the finite deformation stress-strain behavior of poly(ethylene terephthalate) above the glass transition. *Polymer*, 41(6):2183–2201, 2000.

[98] R. J. Asaro and A. Needleman. Texture development and strain hardening in rate dependent polycrystals. *Acta Metallurgica*, 33(6):923–953, 1985.

[99] L. C. A. van Breemen, T. A. P. Engels, C. G. N. Pelletier, L. E. Govaert, and J. M. J. den Toonder. Numerical simulation of flat-tip micro-indentation of glassy polymers: influence of loading speed and thermodynamic state. *Philosophical Magazine*, 89(8):677–696, 2009.

[100] O. A. Hasan, M. C. Boyce, X. S. Li, and S. Berko. An investigation of the yield and post-yield behavior and corresponding structure of poly(methyl methacrylate). *Journal of Polymer Science Part B: Polymer Physics*, 31(2):185–197, 1993.

[101] L. C. A. van Breemen. *Contact mechanics in glassy polymers*. PhD thesis, Eindhoven University of Technology, 2009.

[102] T. A. P. Engels, L. E. Govaert, G. W. M. Peters, and H. E. H. Meijer. Processing-induced properties in glassy polymers: application of structural relaxation to yield stress development. *Journal of Polymer Science Part B: Polymer Physics*, 44(8):1212–1225, 2006.

[103] H. C. E. van der Aa, M. A. H. van der Aa, P. J. G. Schreurs, F. P. T. Baaijens, and W. J. van Veenen. An experimental and numerical study of the wall ironing process of polymer coated sheet metal. *Mechanics of Materials*, 32(7):423–443, 2000.

[104] M. Poluektov, J. A. W. van Dommelen, L. E. Govaert, and M. G. D. Geers. Characterisation and modelling of anisotropic thermo-mechanical behaviour of oriented polyethylene terephthalate. *Modelling and Simulation in Materials Science and Engineering*, 22:055024, 2014.

[105] Y. Z. Bin, K. Oishi, K. Yoshida, T. Nakashima, and M. Matsuo. Orientation distribution functions of the three principal crystallographic axes as well as crystallites of poly(ethylene terephthalate) films under biaxially stretching. *Polymer Journal*, 36(5):394–402, 2004.

[106] U. Göschel. Two-dimensional small-angle X-ray scattering studies on oriented poly(ethylene terephthalate) films. *Polymer*, 36(6):1157–1165, 1995.

[107] C. J. Heffelfinger and R. L. Burton. X-ray determination of the crystallite orientation distributions of polyethylene terephthalate films. *Journal of Polymer Science*, 47(0149):289–306, 1960.

[108] D. P. Jones, D. H. MacKerron, and S. V. Norval. Effect of crystal texture on the anisotropy of thermal expansion in polyethylene naphthalate: measurements and modelling. *Plastics Rubber and Composites*, 42(2):66–74, 2013.

[109] T. A. Tervoort, R. J. M. Smit, W. A. M. Brekelmans, and L. E. Govaert. A constitutive equation for the elasto-viscoplastic deformation of glassy polymers. *Mechanics of Time-Dependent Materials*, 1:269–291, 1998.

[110] D. J. A. Senden, G. W. M. Peters, L. E. Govaert, and J. A. W. van Dommelen. Anisotropic yielding of injection molded polyethylene. *Polymer*, 54(21):5899–5909, 2013.

[111] J. Kuusipalo, A. M. Savijarvi, S. Norval, M. J. Adlen, and D. H. MacKerron. The dependence of tear behaviour on the microstructure of biaxially drawn polyester film. *Journal of Materials Science*, 39(23):6909–6919, 2004.

[112] C. Forbes, M. Evans, N. Hastings, and B. Peacock. *Statistical distributions*. John Wiley & Sons, Inc., 2011.

[113] Y. G. Fu, B. Annis, A. Boller, Y. M. Jin, and B. Wunderlich. Analysis of structure and properties of poly(ethylene terephthalate) fibers. *Journal of Polymer Science Part B: Polymer Physics*, 32(13):2289–2306, 1994.

[114] L. E. Govaert, C. W. M. Bastiaansen, and P. J. R. Leblans. Stress-strain analysis of oriented polyethylene. *Polymer*, 34(3):534–540, 1993.

[115] L. C. E. Struik. The mechanical and physical aging of semicrystalline polymers: 1. *Polymer*, 28(9):1521–1533, 1987.

[116] L. C. E. Struik. Mechanical behavior and physical aging of semicrystalline polymers: 3. Prediction of long-term creep from short-time tests. *Polymer*, 30(5):799–814, 1989.

[117] M. Poluektov, J. A. W. van Dommelen, L. E. Govaert, and M. G. D. Geers. Micromechanical modelling of reversible and irreversible thermo-mechanical deformation of oriented polyethylene terephthalate. 2014. Submitted.

[118] G. Schoukens, P. Samyn, S. Maddens, and T. van Audenaerde. Shrinkage behavior after the heat setting of biaxially stretched poly(ethylene 2,6-naphthalate) films and bottles. *Journal of Applied Polymer Science*, 87(9):1462–1473, 2003.

[119] U. Göschel. Thermally stimulated structural changes in highly oriented glassy poly(ethylene terephthalate). *Polymer*, 37(18):4049–4059, 1996.

[120] B. Haworth, Z. W. Dong, and P. Davidson. Characterization of shrinkage in oriented pet films and containers by thermomechanical analysis (TMA). *Polymer International*, 32(3):325–335, 1993.

[121] V. B. Gupta, J. Radhakrishnan, and S. K. Sett. Effect of processing history on shrinkage stress in axially oriented poly(ethylene terephthalate) fibers and films. *Polymer*, 35(12):2560–2567, 1994.

[122] M. Heuchel, T. Sauter, K. Kratz, and A. Lendlein. Thermally induced shape-memory effects in polymers: quantification and related modeling approaches. *Journal of Polymer Science Part B: Polymer Physics*, 51(8):621–637, 2013.

[123] P. M. Pakhomov, M. V. Shablygin, B. A. Tsaplin, S. A. Baranova, and Z. P. Vysotskaya. Molecular mechanism of shrinkage of polyethylene terephthalate. *Vysokomolekulyarnye Soedineniya: A*, 25(3):572–577, 1983.

[124] J. L. Hu, Y. Zhu, H. H. Huang, and J. Lu. Recent advances in shape-memory polymers: structure, mechanism, functionality, modeling and applications. *Progress in Polymer Science*, 37(12):1720–1763, 2012.

[125] Y. P. Liu, K. Gall, M. L. Dunn, A. R. Greenberg, and J. Diani. Thermomechanics of shape memory polymers: uniaxial experiments and constitutive modeling. *International Journal of Plasticity*, 22(2):279–313, 2006.

[126] H. J. Qi, T. D. Nguyen, F. Castroa, C. M. Yakacki, and R. Shandas. Finite deformation thermo-mechanical behavior of thermally induced shape memory polymers. *Journal of the Mechanics and Physics of Solids*, 56(5):1730–1751, 2008.

[127] G. Barot, I. J. Rao, and K. R. Rajagopal. A thermodynamic framework for the modeling of crystallizable shape memory polymers. *International Journal of Engineering Science*, 46(4):325–351, 2008.

[128] A. Sedighiamiri, D. J. A. Senden, D. Tranchida, L. E. Govaert, and J. A. W. van Dommelen. A micromechanical study on the deformation kinetics of oriented semicrystalline polymers. *Computational Materials Science*, 82:415–426, 2014.

[129] J. A. W. van Dommelen, D. M. Parks, M. C. Boyce, W. A. M. Brekelmans, and F. P. T. Baaijens. Micromechanical modeling of the thermo-elasto-viscoplastic behavior of semi-crystalline polymers. In *Proceedings of the European Congress on Computational Methods in Applied Sciences and Engineering, Barcelona*, 2000.

[130] F. T. Meissonnier, E. P. Busso, and N. P. O'Dowd. Finite element implementation of a generalised non-local rate-dependent crystallographic formulation for finite strains. *International Journal of Plasticity*, 17(4):601–640, 2001.

[131] B. F. Blumentritt. Anisotropy and dimensional stability of biaxially oriented poly(ethylene terephthalate) films. *Journal of Applied Polymer Science*, 23(11):3205–3217, 1979.

[132] C. L. Choy, M. Ito, and R. S. Porter. Thermal expansivity of oriented poly(ethylene terephthalate). *Journal of Polymer Science Part B: Polymer Physics*, 21(8):1427–1438, 1983.

[133] A. M. Adams, C. P. Buckley, and D. P. Jones. Biaxial hot drawing of poly(ethylene terephthalate): measurements and modelling of strain-stiffening. *Polymer*, 41(2):771–786, 2000.

[134] J. A. W. van Dommelen. *Micromechanics of particle-modified semicrystalline polymers*. PhD thesis, Eindhoven University of Technology, 2003.

[135] B. F. Blumentritt. Laminated films with isotropic in-plane properties. *IBM Journal of Research and Development*, 23(1):66–74, 1979.

[136] S. Lee and G. C. Rutledge. Plastic deformation of semicrystalline polyethylene by molecular simulation. *Macromolecules*, 44(8):3096–3108, 2011.

Samenvatting

In flexibele elektronica worden conventionele substraatmaterialen zoals silicium vervangen door polymere materialen, waardoor flexibiliteit geboden wordt en *roll-to-roll* productie mogelijk gemaakt wordt. Polymere films die gebruikt worden als substraat voor flexibele elektronica hebben gewoonlijk een sterk georiënteerde semikristallijne microstructuur en moeten voldoen aan een aantal voorwaarden, zoals goede dimensionele stabiliteit, ook bij verhoogde temperaturen. Deze dimensionele stabiliteit is sterk afhankelijk van de interne macromoleculaire oriëntatie.

Dit proefschrift is gericht op het begrijpen en voorspellen van de effecten van de microstructuur en van de belastingcondities (spanning, temperatuur en tijdsafhankelijkheid) op de mechanische respons van dunne semikristallijne polymere films. Hiertoe is een micromechanisch thermoelasto-viscoplastisch model ontwikkeld waarmee de dimensionele stabiliteit van films blootgesteld aan diverse belastingen voorspeld kan worden. Het beschouwde materiaal bestaat uit een aggregaat van verschillend georiënteerde gelaagde tweefasen domeinen, waarbij verschillende constitutieve relaties gebruikt worden voor ieder van de fasen. De kristallijne fase is gemodelleerd met kristal viscoplasticiteit en de amorfe fase is beschreven als een elasto-viscoplastisch glasachtig polymeer, waarbij materiaalveroudering in beschouwing is genomen.

In het tweede hoofdstuk worden de interacties tussen de verschillende fasen van isotroop semikristallijn polyethyleentereftalaat (PET) geanalyseerd. De validiteit van een hybride interactiewet in een *mean-field* micromechanisch model gebaseerd op het mechanische gedrag van gelaagde tweefasen domeinen wordt geëvalueerd. Hiertoe wordt een ander tweeschalig eindige elementenmodel van de sferulitische microstructuur van een semikristallijn polymeer geconstrueerd, waarbij verschillende kristalgeometrieën beschouwd worden, inclusief het geval waarin de kristallijne gebieden geen onderling verbonden netwerk vormen. Aangetoond wordt dat de voorspellingen van grootheden voor microscopische deformatie en macroscopische eigenschappen verkregen met beide modellen kwalitatief en kwantitatief overeenkomen.

In het derde hoofdstuk wordt het micromechanisch model gebruikt om het mechanische gedrag van isotroop semikristallijn PET te beschrijven onder uniaxiale compressie tot grote rekken bij verschillende temperaturen. Model parameters van de geselecteerde constitutieve relaties van de fasen worden bepaald aan de hand van experimentele data. Het kruipgedrag onder trekbelasting van isotroop PET wordt gesimuleerd en vergeleken met metingen om de toepasbaarheid van het model voor het beschrijven van het langeduur gedrag te demonstreren.

In het vierde hoofdstuk wordt het langeduur en korteduur anisotrope mechanische gedrag van een biaxiaal verstrekte PET film gemeten en gesimuleerd met het micromechanisch model. De representatieve microstructuur van de film is verkregen middels experimentele karakterisering van

de oriëntatie van de kristallijne domeinen. Het model wordt verder uitgebreid door het opnemen van voororiëntatie van de niet-kristallijne fase. Gebaseerd op resultaten van simulaties worden de deformatiemechanismen op microscopische schaal geanalyseerd. Het vermogen om het grote rek anisotrope gedrag van georiënteerde film te beschrijven in een reksnelheidsgestuurd regiem en het langeduur kruip regiem wordt gedemonstreerd.

In het vijfde hoofdstuk worden mechanismen van anisotrope reversibele en irreversibele thermische deformatie in een polymere film geproduceerd door biaxiaal verstrekken experimenteel bestudeerd en numeriek beschreven met het voorgestelde micromechanische model. De onderzochte thermo-mechanische effecten kunnen geclassificeerd worden als geheugeneffecten aangezien het materiaal gedeeltelijk terugkeert naar de initiële toestand voor biaxiaal verstrekken. De interne spanningstoestand wordt beschreven met twee deformatieprocessen met ieder een andere interne spanningstoestand en thermische activeringsenergie.

In hoofdstuk zes wordt het ontwikkelde micromechanisch model gebruikt om het gedrag van de film te voorspellen wanneer het onderworpen wordt aan condities die representatief zijn voor de productie van flexibele OLED's. Effecten van kruip en thermische krimp, die experimenteel tegelijk waargenomen worden, worden gemodelleerd.

Acknowledgements

Curriculum vitae

Mikhail Poluektov was born on 31 March 1987 in Leningrad, USSR (now Saint Petersburg, Russian Federation). In 2004, after finishing the secondary education, he started higher education in mechanical engineering at Saint Petersburg State Polytechnical University. In 2006, he won the first place in the Strength of Materials all–Saint Petersburg university student competition and the fifth place in the all–Russia competition. During his higher education, Mikhail was participating in research projects on dynamics of dipole systems and on numerical algorithms for elastoplasticity, part of which was conducted at the Dresden University of Technology. The topic of his graduation project was optimal control in physical chemistry. In 2010, he graduated with honours from the Mechanics and Control Processes Department of Saint Petersburg State Polytechnical University.

In 2010, Mikhail started a PhD project on thermo-mechanical behaviour of oriented semicrystalline polymers at the Eindhoven University of Technology. This project was supported by the Materials innovation institute (M2i) and carried out in the group of prof.dr.ir. M.G.D. Geers, supervised by dr.ir. J.A.W. van Dommelen and dr.ir. L.E. Govaert. Since 2014, Mikhail is employed by Uppsala University.